Institute of Thermoelectricity, Academy of Sciences and Ministry of Education and Science of Ukraine

Journal of THERMOELECTRICITY

International Research
Founded in December, 1993
published 6 times a year

No. 2 *2015*

Founders – National Academy of Sciences, Ukraine
Institute of Thermoelectricity of National Academy of Sciences and Ministry of Education and Science of Ukraine

Certificate of state registration № KB 15496-4068 ПР

Editorial office manager O. Pugantseva

Editors:

L. Vikhor, V. Kramar, V. Katerynchuk, O. Luste, A. Farion, O. Bodnaruk

Approved for printing by the Academic Council of Institute of Thermoelectricity
of the National Academy of Sciences and Ministry of Education and Science, Ukraine

Address of editorial office:
Ukraine, 58002, Chernivtsi, General Post Office, P.O. Box 86.
Phone: +(380-372) 90 31 65.
Fax: +(380-3722) 4 19 17.
E-mail: jt@inst.cv.ua
http://www.jt.inst.cv.ua

Signed for publication 25.05.15. Format 70×108/16. Offset paper №1. Offset printing.
Printer's sheet 11.5. Publisher's signature 9.2. Circulation 400 copies. Order 5.

Printed from the layout original made by “Journal of Thermoelectricity” editorial board
in the printing house of “Bukrek” publishers,
10, Radischev Str., Chernivtsi, 58000, Ukraine

CONTENTS

Material Research

Design

Metrology and standardization

Thermoelectric products

News

* – papers of XVI International Forum on thermoelectricity

E.I. Rogacheva[1], A.V. Budnik[1], A.G. Fedorov[2], A.S. Krivonogov[3], P.V. Mateychenko[3]

[1]National Technical University "Kharkiv Polytechnic Institute",
21 Frunze St., Kharkiv 61002, Ukraine
[2]Institute for Scintillation Materials NAS of Ukraine, 60 Lenin Ave., Kharkiv, 61001, Ukraine
[3]Institute for Single Crystals NAS of Ukraine, 60 Lenin Ave., Kharkiv, 61001, Ukraine

STRUCTURE OF p-Bi_2Te_3 THIN FILMS PREPARED BY SINGLE SOURCE THERMAL EVAPORATION IN VACUUM

The growth mechanism, microstructure, and crystal structure of thin Bi_2Te_3 films with thicknesses d = 28 – 620 nm prepared by thermal evaporation of stoichiometric Bi_2Te_3 crystals in vacuum onto glass substrates were studied using X-ray diffraction, scanning electron microscopy, energy dispersive spectroscopy, and atomic force microscopy. The obtained thin films were polycrystalline, exhibited p-type conductivity and did not contain any other phases except for Bi_2Te_3. It was shown that with increasing film thickness, the crystallite size increased up to ~ 700-800 nm. It was established that the preferential orientation of crystallite growth was [00*l*] *direction corresponding to a trigonal axis C_3 in hexagonal lattice. When the film thickness exceeded ~ 200-250 nm, along with reflections from (00l) planes, reflections from other planes appeared, which indicated a certain disorientation of crystallites. The results obtained show that using a simple and inexpensive method of thermal evaporation from a single source and choosing optimal technological parameters, one can grow thin p-Bi_2Te_3 films of sufficiently high quality.*

Key words: bismuth telluride, thermal evaporation, thin film, thickness, structure, growth orientation.

Introduction

Bi_2Te_3 semiconductor compound and Bi_2Te_3-based solid solutions belong to the best low-temperature thermoelectric (TE) materials, which are widely used in the manufacture of different types of refrigerating devices [1-4]. A growing interest in low-dimensional nanostructures based on bismuth telluride [5-7] stimulates conducting detailed studies of properties of the indicated materials in the thin film state and establishing correlations among technological parameters, structure, and TE characteristics. In recent years, the interest in studying bulk crystals and thin films of Bi_2Te_3 has grown even more after the discovery of new unique physical objects – topological insulators. It was established that Bi_2Te_3 possesses properties of a 3D topological insulator, which attracted attention to studies of thin Bi_2Te_3 films, in which the contribution of the surface layer to electrical conductivity increases in comparison with bulk crystals, thus making it possible to reveal the specificity of topological objects [8-10]. Works have appeared which showed a connection between topological and TE properties and pointed out the possibility to use this fact in searching for principally new ways of increasing TE efficiency [11-19].

Bi_2Te_3 crystallizes in a rhombohedral structure (space group $R3m$-D_{3d}^5) [2, 4]. Often for describing Bi_2Te_3 structure, instead of rhombohedral a hexagonal unit cell is used whose parameters correspond to a = 0.4386 nm and c = 3.0497 nm [2, 4]. The structure is composed of five-layer packets (quintets) − Te^1− Bi− Te^2− Bi− Te^1 (indices 1 and 2 denote different positions of Te atoms in the crystal lattice), perpendicular to a third-order symmetry axis (a trigonal axis C_3 in a hexagonal lattice). Within each layer, similar atoms constitute a hexagonal flat lattice forming a hexagonal close packing with atoms of lower layers. Chemical bonds within quintets are predominantly covalent-ionic, whereas between quintets there are weak van der Waals bonds. This determines a low mechanical strength, easy splitting of crystals along cleavage planes (perpendicular to a C_3 axis) and substantial anisotropy of all physical properties of Bi_2Te_3 single crystals.

Bi_2Te_3 has a narrow homogeneity region (59.75 – 60.2 at.% Te at 770 K [20]) in the Bi – Te system. The stoichiometric Bi_2Te_3 (60.0 at.% Te) exhibits p-type conductivity due to the presence of anti-site defects $BiTe$.

Bi_2Te_3 films can be grown by a variety of methods: thermal evaporation in vacuum from a single source [21-30], thermal co-evaporation from two sources [31-33], hot wall epitaxy [34-36], quasi-closed volume technique [37], ion-beam deposition [38], magnetron sputtering [26, 39], molecular-beam epitaxy [27-29, 40], liquid phase epitaxy [30], metal organic chemical vapor deposition [41], laser deposition [42-44], explosive evaporation [45] and so on. Both amorphous and crystalline materials can be used as substrates. It was established that on amorphous substrates (glass [21-26, 39], SiO_2 [34-36], kapton [35, 31]), films grow in an island-like fashion, while on crystalline substrates (BaF_2 [27], Si [34, 28, 36, 40], sapphire [29]) both island-like [27] and layer-by-layer [27-29] growth can be realized. The growth mechanism, film morphology, grain size, and grain crystallographic orientation depend on the film preparation technique and technological parameters.

For anisotropic materials like Bi_2Te_3, the transport properties depend significantly on the direction in the crystal. For example, it was reported in [39] that in Bi_2Te_3 films the preferential growth of (00*l*) planes leads to substantially higher values of electrical conductivity, charge carrier mobility and the Seebeck coefficient in comparison with the preferential growth of (015) planes. That is why, when growing films, it is important to know and to control the preferential growth direction.

The growth mechanism and structure of Bi_2Te_3 thin films prepared by thermal evaporation in vacuum from a single source onto glass substrates were investigated in few works [23-25]. In [23], where the authors did not indicate the substrate temperature, it was established using X-ray diffraction analysis that in films with thicknesses d = 36 – 330 nm deposited onto glass substrates the preferential orientation of crystallites corresponded to [015] direction, although under increasing film thickness additional peaks appeared in X-ray diffraction patterns, which indicated a partial grain disorientation. In [24], X-ray diffraction analysis was used to study the structure of Bi_2Te_3 films of the fixed thickness (d = 100 nm) but deposited onto glass substrates heated to different temperatures (T_S = 303 – 573 K). The authors found out that for all values of T_S the preferential growth takes place along the [015] direction, although there is some disorientation of grains relative to this direction. Note that in [23, 24] the films were not subjected to annealing which could improve the quality of their structure, and perhaps because of this the crystallite size D in the films was small (D = 15 – 45 nm). The authors of [25] investigated sufficiently thick Bi_2Te_3 films (d = 170 – 342 nm), which were annealed at T = 443 K for one hour. They reported that the film with thickness d = 342 nm had the preferential orientation of growth along the [015] direction, which manifests clearly only after annealing. With increasing film thickness from 170 nm to 342 nm, the grain size increased from 60 up to 160 nm. Thus, in the available works on Bi_2Te_3 films prepared by thermal evaporation of Bi_2Te_3 crystals in vacuum onto glass substrates and characterized by X-ray diffraction method, authors reported their observation of preferential orientation only along the [015] axis. There arises a question whether it is possible to obtain another preferential orientation, specifically [00*l*], which as was mentioned above is more desirable because of the possibility to obtain higher values of TE figure of merit.

The goal of the present work is to carry out a detailed comprehensive investigation of the microstructure and crystal structure of thin Bi_2Te_3 films grown by thermal evaporation of stoichiometric bismuth telluride crystals in vacuum and subsequent condensation onto glass substrates.

Experimental procedure

As a charge for thin films preparation, *p*-type Bi_2Te_3 polycrystal of stoichiometric composition was used. Crystal synthesis was made by direct alloying of *Bi* and *Te* of high purity (99.999 at. %) in evacuated quartz ampoules at a temperature of (1020 ± 10) K for 5 – 6 hours with subsequent annealing at 670 K for 300 hours.

Films of thickness d = 28– 620 nm were grown by method of thermal evacuation in vacuum (~10^{-5} Pa) of Bi_2Te_3 polycrystal of stoichiometric composition and subsequent condensation onto glass substrates heated to temperature T_S = 500 K. Condensation rate was 0.1 – 0.3 nm/s. Prior to deposition, substrates were consecutively cleaned with hydrochloric acid, distilled water and 95% alcohol. Immediately after deposition, grown films in the same vacuum chamber were annealed at a temperature of T = 500 K for 1 hour. For a simultaneous preparation of several films of different thickness d in one technological process, three substrate holders were installed at different distances from the source. Earlier we showed [21, 22] that the properties of Bi_2Te_3 thin films are essentially dependent on the stoichiometry of source crystal, substrate temperature T_S, the presence or absence of annealing, annealing temperature, on which basis the above technological parameters were determined that corresponded to maximum values of TE power $P = S^2\sigma$ (S is the Seebeck coefficient, σ is electric conductivity).

The thickness and roughness of films, as well as condensation rate, were controlled by quartz resonator. Calibration of resonator for film thicknesses less than $d \sim 100$ nm was performed with the use of X-ray diffraction patterns of small-angle scattering by comparing the experimental and calculated diffraction patterns. At layer thicknesses $d < 100$ nm close to primary beam an interference X-ray diffraction is observed, namely the Kissing oscillations whose period can be used to determine film thickness to an accuracy of 0.5 nm. Numerical simulation was performed with the use of Frenkel’s formulae. For fitting of calculated curve to the experimental one two parameters were varied independently, namely film thickness and roughness. For large thicknesses ($d > 100$ nm), quartz resonator was calibrated using MII-4 interferometer.

Chemical composition, homogeneity degree and films morphology were studied by electron probe analysis method with the use of scanning electron microscope (SEM) JSM-6390LV (Jeol Ltd., Japan), equipped with energy-dispersive X-ray spectrometer X-max N50. The surface morphology of films was also studied using atomic force microscope (AFM) Solver Pro NT-MDT. Crystal structure, phase composition and direction of preferential films growth were determined by X-ray structural analysis methods on DRON-2 diffractometer using $Cu\ K_\alpha$ – radiation.

Experimental results

Fig. 1, a shows X-ray diffraction pattern of Bi_2Te_3 polycrystal which was used as a charge for preparation of thin films. All the lines on X-ray diffraction pattern corresponded to values given in ASTM standards for Bi_2Te_3 (№ 15-863) [46], no additional phases were found.

Fig. 1, b-h show X-ray patterns of thin films of different thickness prepared with optimal technological parameters. The films have a marked crystalline structure, and all diffraction peaks correspond to Bi_2Te_3 compound, no peaks of other phases were found. To demonstrate the influence of films preparation technology on their phase composition and structure, Fig. 2 shows X-ray patterns of films (d = 250 nm) obtained at substrate temperature T_S = 320 K without annealing (Fig. 2, a) and at substrate temperature T_S = 500 K with annealing for one hour at 500 K (Fig. 2, b), i.e. prepared by the method used in the present paper. It can be seen that in the former case the film has a structure close to amorphous, with weakly expressed diffraction peaks, and the film has additional phases of Te and Bi_3Te_4. In this connection it can be assumed that due to higher partial pressure of Te vapour as compared to bismuth, during the initial stages of film deposition tellurium excess can be created on the substrate. As long as substrate temperature is sufficiently low (T_S = 320 K), no intensive reevaporation of Te atoms occurs, and part of Te atoms precipitates into second phase. With further formation of the film, deficit of Te atoms can result in formation of Bi_3Te_4 phase. High intensity of peak corresponding to (015) planes testifies to preferential formation in the film of hexagonal planes with respective structure.

As in seen in Fig. 1, b-e, in the films with thicknesses d lower than d ~ 140 nm, the intensity of peaks (003), (006), (0 0 15), (0 0 18) and (0 0 21) is increased more than twice as compared to the bulk crystal with practically complete disappearance of peaks corresponding to other crystallographic planes. Essential increase of the intensity of peaks corresponding to these planes as compared to similar peaks of X-ray diffraction pattern of the source powder indicate the presence of texture in [001] direction. To confirm the presence of preferential orientation of crystallites along [00l] direction, fim of thickness d = 85 nm (Fig. 1, h) was measured in a standard mode (in the initial position X-ray beam was oriented perpendicular to the film), and then the sample was rotated by 21.80°. As long as planes (0 0 21) and (0 1 20) are at an angle of 21.80° to each other, in the former case there is intensive peak only from (0 0 21) plane, and in the second case – only from (0 1 20) plane, confirming the presence of preferential orientation of all grains in one direction [0 0 l].

The authors [35, 36] attribute formation of texture in [0 0 1] direction to peculiarity of Bi_2Te_3 growth on amorphous substrates which assure higher surface mobility of deposited substance atoms as compared to crystalline substance. This allows reaching sufficiently fast the state close to equilibrium, when the atoms of deposited substance occupy thermodynamically most advantageous positions on the substrate, which contrtibutes to texture formation. Moreover, epitaxial growth peculiarities of layered structures with Van der Waals bonds [36, 37] and the absence of broken bonds on the substrate surface [34] cause the arrangement of layers with Van der Waals bonds along the film plane which in turn provides for orientation of crystallites in perpendicular direction [0 0 1] [37]. Strong anisotropy of growth rate assures a more intensive growth of crystallites along the directions perpendicular to texture direction, which contributes to fast intergrowth of crystallites in film plane, and growth rate of Bi_2Te_3 films parallel to substrate surface proves to be a factor of 5 to 8 higher than growth rate perpendicular to it.

On the X-ray diffraction patterns of films with thicknesses more than d ~ 140 nm (Fig. 1 f, g) along with reflexes (0 0 l) there appear peaks from crystallographic planes different from (0 0 1), the number increasing with increase in film thickness. This testifies to disorientation of crystallites and is likely to be a consequence of dislocation density growth and stress accumulation. Nevertheless, the intensity of peaks (0 0 l) for all films is almost not changed which testifies to the absence of essential disorientation in the direction of texture.

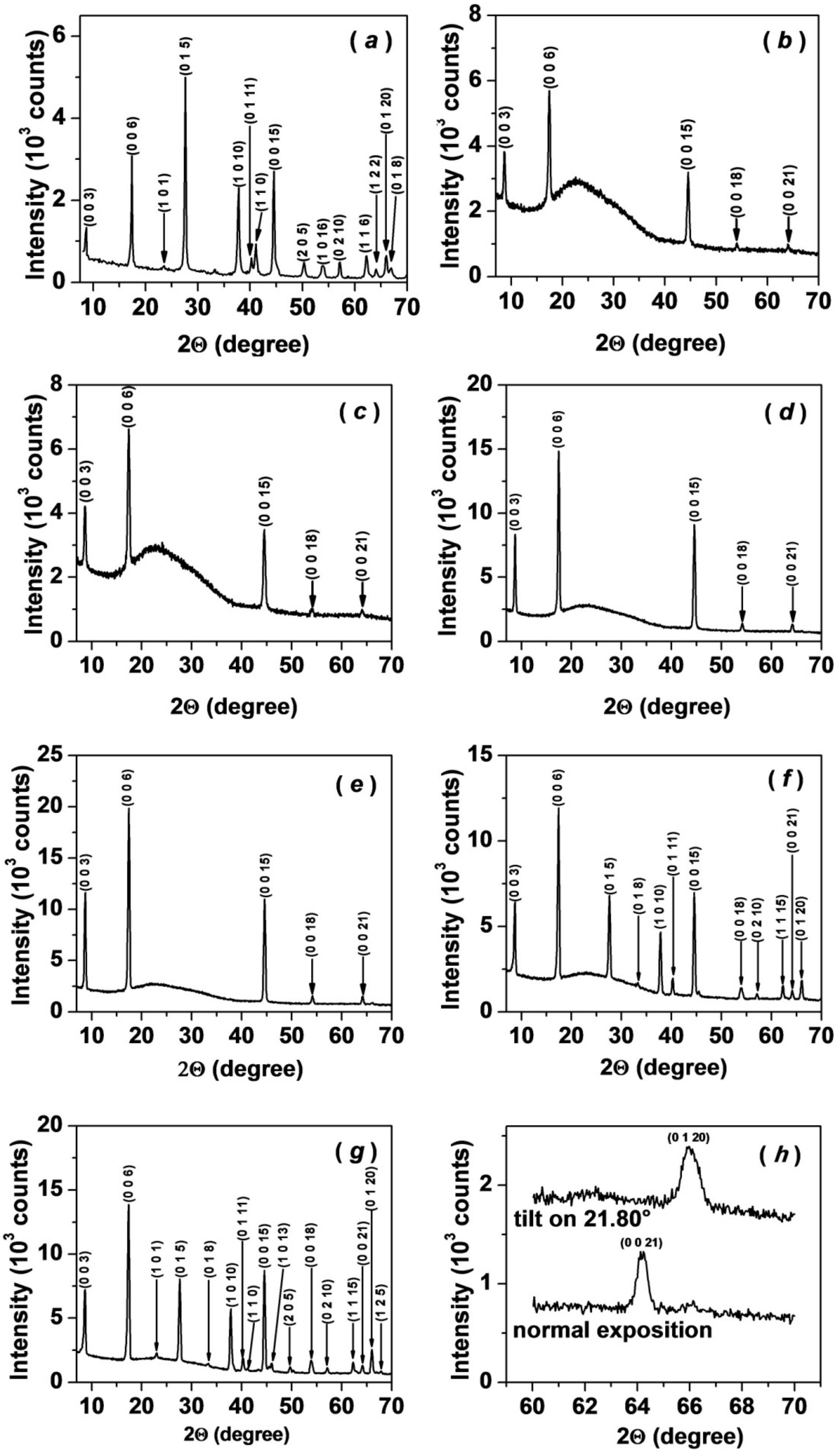

Fig. 1. X-ray diffraction patterns for polycrystalline Bi_2Te_3 powder (a) and for thin films with different thicknesses: d = 38 nm (b), 45 nm (c), 85 nm (d), 140 nm (e), 370 nm(f), 620 nm (g).
h: X-ray diffraction pattern for the thin film with d = 85 nm is measured in a standard mode (with a X-ray beam oriented perpendicular to the film surface) and after rotating the sample by 21.80° (see the text).

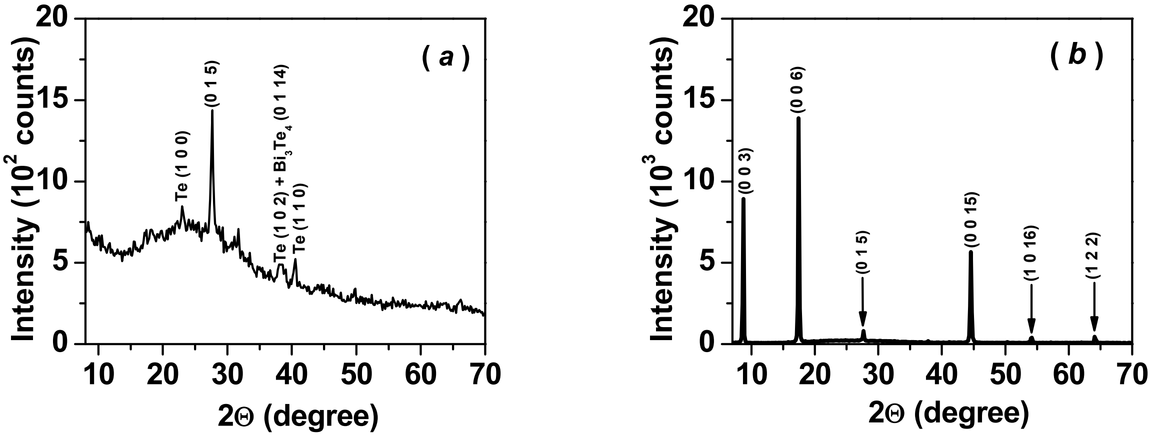

Fig. 2. X-ray diffraction patterns for Bi_2Te_3 films with thicknesses d = 250 nm prepared at the substrate temperature T_S = 320 K without annealing (a) and at T_S = 500 K with subsequent annealing at 500 K for one hour (b).

Studies of thin films by scanning electron microscopy method (Fig. 3) have confirmed that the films are polycrystalline and there are no second phase inclusions in them. The grains were of hexagonal shape (for illustrative purposes some grains are shown dashed) and their average size was increased with increase in film thickness (Fig. 4), which was in good agreement with the results of AFM. The results of energy-dispersive X-ray spectroscopy both at scanning along the sample surface and in the mode of probing from point to point have shown that all the films were characterized by high homogeneity degree and that within the error of this method one could speak of the conformity between the composition of the source polycrystal and that of grown films.

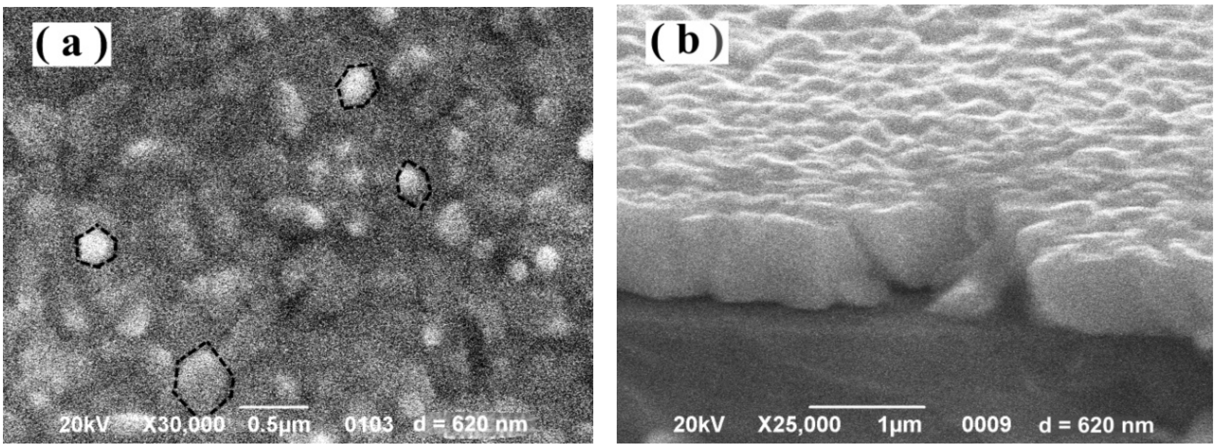

Fig. 3. Surface images obtained using a scanning electron microscope (SEM) for Bi_2Te_3 film with thickness d = 620 nm. a – no tilt, b - tilt angle 70^0.

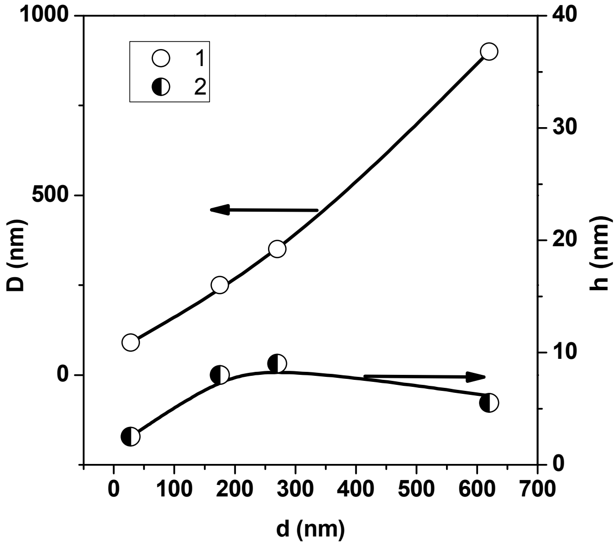

Fig. 4. Grain size D and roughness h as functions of p-Bi_2Te_3 thin film thickness d.
1 – grain size; 2 – roughness.

Fig. 5 represents the data of atomic force microscopy. On the obtained profilograms one can clearly see individual crystallites of mainly hexagonal shape, which points to their orientation in [0 0 1] direction perpendicular to film surface which is in good agreement with the results of X-ray structural analysis (Fig. 1), as well as with the data of scanning electron microscopy (Fig. 3). The sizes of crystallites D evaluated by two methods – SEM and AFM – practically coincide and show marked increase with increase in film thickness, reaching in the "thickest" of films under study (d = 620 nm) the value of D ~ 850 nm (Fig. 4). The roughness of films h with growth in their thickness d first increases (to d ~ 200 – 250 nm), following which there is a tendency to h reduction (Fig. 4).

Conclusions

A comprehensive study of growth mechanism, microstructure, and crystal structure of thin Bi_2Te_3 films with thicknesses d = 28 – 620 nm prepared by thermal evaporation of stoichiometric Bi_2Te_3 crystals in vacuum onto glass substrates heated to T_S = 500 K and subject to subsequent annealing at 500 K was performed using X-ray diffraction, scanning electron microscopy, energy dispersive spectroscopy, and atomic force microscopy.

It was established that both the initial crystal and all obtained thin films exhibited p-type conductivity and did not contain any other phases except for Bi_2Te_3.

It was shown that the obtained thin films were polycrystalline; with increasing film thickness, the grain size D of the films increased to D ~ 850 nm, and roughness h increased with increasing film thickness to ~d ~ 200-250 nm, following which there was a tendency to reduction.

It was established that the preferential orientation of crystallite growth was [00l] direction corresponding to a trigonal axis C_3 in hexagonal lattice. When the film thickness exceeded ~ 200-250 nm, along with reflections from (00l) planes, reflections from other planes appeared, which indicated a certain disorientation of crystallites.

The results obtained show that using a simple and inexpensive method of thermal evaporation from a single source and choosing optimal technological parameters, one can grow thin p-Bi_2Te_3 films of sufficiently high quality.

The work was performed with support from the State Foundation for Basic Research (Ukraine) (Grant #UU 42/006-2011) and US Civilian Research and Development Foundation (Grant # UKP-7074-KK-12).

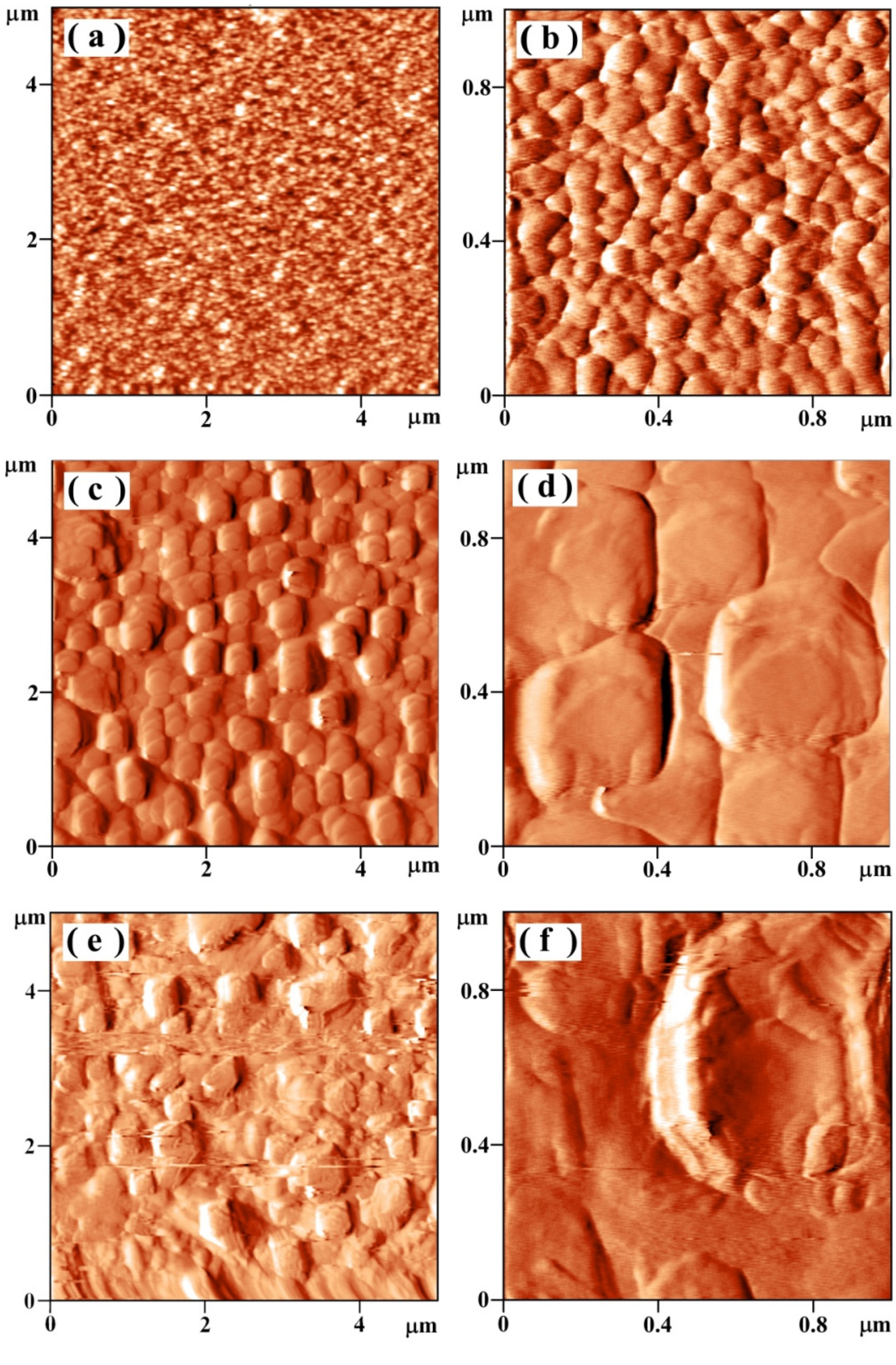

Fig.5. AFM surface profilograms for Bi_2Te_3 thin films with thickness d = 28 nm: 5x5 μm (a), 1x1 μm (b); d = 175 nm: 5x5 μm (c), 1x1 μm (d); d = 270 nm: 5x5 μm (e), b: 1x1 μm (f).

References

1. L.I. Anatychuk, *Thermoelements and Thermoelectric Devices: Reference Book*, (Kyiv: Naukova Dumka, 1979).
2. H. Scherrer, S. Scherrer, Bismuth Telluride, Antimony Telluride and their Solid Solution (*CRC Handbook of thermoelectric Edited by D.M. Rowe, 1995*), P. 213–223.
3. L.E. Bell. Cooling, Heating, Generating Power, and Recovering Waste Heat with Thermoelectric Systems, *Science* **321**, 1457 (2008).
4. B.M.Goltsman, V.A.Kudinov, and I.A. Smirnov, *Semiconducting Thermoelectric Materials Based on Bi_2Te_3* (Moscow: Nauka, 1972) (in Russian).
5. L D. Hicks, M. S. Dresselhaus, Effect of Quantum-Well Structures on the Thermoelectric Figure of Merit, *Phys. Rev. B* **47**, 12727 (1993). DOI: http://dx.doi.org/10.1103/PhysRevB.47.12727
6. M.S. Dresselhaus, Yu-Ming Lin, T. Koga, S.B.Cronin, O. Rabin, M.R. Black, and G. Dresselhaus, In *Semiconductors and Semimetals: Recent Trends in Thermoelectric Materials Research III, edited by T.M. Tritt*, (Academic Press, San Diego, CA, 2001), pp. 1–121.
7. R. Venkatasubramanian, E. Siivola, T. Colpitts, and B. O'Quinn, Thin-Film Thermoelectric Devices with High Room-Temperature Figures of Merit, *Nature* **413**, 597 (2001). DOI: http://dx.doi.org/10.1038/35098012
8. L. Fu, C. L. Kane, Topological Insulators with Inversion Symmetry, *Phys Rev. B* **76**, 045302 (2007). DOI: http://dx.doi.org/10.1103/PhysRevB.76.045302
9. L. Muchler, F. Casper, B. Yan, S. Chadov, and C. Felser, Topological Insulators and Thermoelectric Materials, *Phys. Status Solidi RRL* **7**, 91 (2013). DOI: http://dx.doi.org/10.1002/pssr.201206411.
10. D. Culcer, Transport in Three-Dimensional Topological Insulators: Theory and Experiment, *Physica E* **44**(8), 860 (2012). DOI: http://dx.doi.org/10.1016/j.physe.2011.11.003.
11. D. Teweldebrhan, V. Goyal, M. Rahman, and A. Balandin, *Appl. Phys. Lett*. **96**, 053107 (2010).
12. Y. S. Hor, A. Richardella, P. Roushan, Y. Xia, J.G. Checkelsky, A. Yazdani, M. Z. Hasan, N.P. Ong, and R.J. Cava1, *Phys. Rev. B* **79**, 195208 (2009).
13. Y.L. Chen, Z.K. Liu, J.G. Analytis, J.-H. Chu, H. J. Zhang, B. H. Yan, S.-K. Mo, R. G. Moore, and D. H. Lu, *Phys. Rev. Lett*. **105**, 266401 (2010).
14. P. Ghaemi, R.S.K. Mong, and J. Moore, *Phys. Rev. Lett*. **105**, 166603 (2010).
15. O.A. Tretiakov, Ar. Abanov, and Jairo Sinova, *Appl. Phys. Lett*. **99**, 113110 (2011).
16. Y. Sun, H. Cheng, S. Gao, Q. Liu, Z. Sun, C. Xiao, C. Wu, S. Wei, and Y. Xie, *J. Am. Chem. Soc.* **134**, 20294 (2012).
17. Z. Fan, J. Zheng, H.-Q. Wang, and J.-C. Zheng, *Nanoscale Research Letters* **7**, 570 (2012).
18. R. Takahashi and S. Murakami, *Semicond. Sci. Technol*. **27**, 124005 (2012).
19. L. Müchler, F. Casper, B. Yan, S. Chadov, and C. Felser, *Phys. Stat. Solidi RRL* **7**, 91 (2013).
20. R.F. Brebrick, Homogeneity Ranges and Te_2-Pressure along the Three-Phase Curves for Bi_2Te_3(c) and a 55–58 at.% Te, Peritectic Phase, *J. Phys. Chem. Sol*. **30**(3), 719, (1969). DOI: http://dx.doi.org/10.1016/0022-3697(69)90026-2
21. A. V. Budnik, E. I. Rogacheva, V. I. Pinegin, A. Yu. Sipatov, A. G. Fedorov, Effect of Initial Bulk Material Composition on Thermoelectric Properties of Bi_2Te_3 Thin Films, *J. Electron. Mater* **42** (7), 1324 (2013). DOI: http://dx.doi.org/10.1007/s11664-012-2439-1

22. A. V. Budnik, E. I. Rogacheva, A.Yu. Sipatov, Effect of Fabrication Technique on the Structure and Thermoelectric Properties of Bi_2Te_3 films, *J. Thermoelectricity* **4**, 19 (2013).
23. R. Sathyamoorthy, J. Dheepa, Structural Characterization of Thermally Evaporated $B_{i2}T_{e3}$ Thin Flms, *J. Phys.Chem. Solids* **68**(1), 111 (2007). DOI: http://dx.doi.org/ 10.1016/j.jpcs.2006.09.014
24. B. Jariwala, D.V. Shah, V. Kheraj, Substrate Temperature Effect on Structural Properties of Bi_2Te_3 Thin Films, *J. Nano- Electron. Phys*. **3**, 101 (2010).
25. F.S. Bahabri, Investigation of the Structural and Optical Properties of Bismuth Telluride (Bi_2Te_3) Thin Films, *Life Science Journal* **9**(1), 290 (2012).
26. Y. Deng, H. Liang, Y. Wang, Z. Zhang, M. Tan, and J. Cui, Growth and Transport Properties of Oriented Bismuth Telluride Flms, *J.Alloys and Compounds* **509**(18), 5683 (2011). DOI: http://dx.doi.org/10.1016/j.jallcom.2011.02.123
27. J.Numus, H. Bottner, H. Beyer, and A. Lambrecht, Epitaxial Bismuth Telluride Layers Grown on (111) Barium Fluoride Substrates Suitable for MQW-Growth, *18th International Conference on Thermoelectrics, 696 (2000).* DOI: http://dx.doi.org/10.1109/ICT.1999.843481
28. J. Krumrain, G. Mussler, S. Borisova, T. Stoica, L. Plucinski, C. M. Schneider, and D. Grützmacher, MBE Growth Optimization of Topological Insulator Bi_2Te_3 Films, *J. Crystal Growth* **324** (1), 115 (2011). DOI: http://dx.doi.org/ 10.1016/j.jcrysgro.2011.03.008
29. J. J. Lee, F. T. Schmitt, R. G. Moore, I. M. Vishik, Y. Ma, and Z. X. Shen, Intrinsic Ultrathin Topological Insulators Grown via MBE Characterized by in-situ Angle Resolved Photoemission Spectroscopy, *Appl. Phys. Lett*. **101**, 013118 (2012). DOI: http://dx.doi.org/
30. C.Boulanger, Thermoelectric Material Electroplating: a Historical Review, *J. Electron. Mater.* **39**, 1818-1827 (2010). DOI: http://dx.doi.org/10.1063/1.4733317
31. L. M. Goncalve, C. Couto, P. Alpuim, A. G. Rolo , F. Völklein, and J. H. Correia, Optimization of Thermoelectric Properties on Bi_2Te_3 Thin Films Deposited by Thermal Co–Evaporation, *Thin Solid Films* **518**(10), 2816 (2010). DOI: http://dx.doi.org/10.1016/j.tsf.2009.08.038
32. Luciana W. da Silva, Massoud Kaviany, and Ctirad Uher, Thermoelectric Performance of Films in the Bismuth–Tellurium and Antimony–Tellurium Systems, *J. Appl. Phys*. **97**(11), 1 (2005). DOI: http://dx.doi.org/10.1063/1.1914948
33. H. Zou, D.M. Rowe, and S.G.K.Williams, Peltier Effect in a Co-Evaporated Sb_2Te_3(P)-Bi_2Te_3(N) Thin Film Thermocouple, *J. Appl. Phys*. **408**(1-2), 270 (2002). DOI: http://dx.doi.org/ 10.1016/S0040-6090(02)00077-9
34. J. C. Tedenac, S. Dal Corso, A. Haidoux, S. Charar, and B. Liautard, Growth of Bismuth Telluride Thin Films by Hot Wall Epitaxy, Thermoelectric Properties, *Mat. Res. Soc. Symp. Proc.* 545, 93 (1998). DOI: http://dx.doi.org/ 10.1557/PROC-545-93
35. M. Ferhat, J. C. Tedenac, and J. Nagao, Mechanisms of Spiral Growth in Bi_2Te_3 Thin Films Grown by the Hot–Wall–Epitaxy Technique, *Journal of Crystal Growth* **218**(2-4), 250 (2000). DOI: http://dx.doi.org/ 10.1016/S0022-0248(00)00582-0
36. M. Ferhat, B. Liautard, G. Brun, J.C. Tedenac, M. Nouaoura, and L. Lassabatere, Comparative Studies between the Growth Characteristics of Bi_2Te_3 Thin Films Deposited on SiO_2, Si(100) and Si(111), *J. Cryst. Growth 167*(1-2), 122 (1996). DOI: http://dx.doi.org/ 10.1016/0022-0248(96)00247-3
37. O. Vigil–Galan, F. Cruz–Gandarilla, J. Fandino, F. Roy, J. Sastre–Hernandez, and G. Contreras–Puente, Physical Properties of Bi_2Te_3 and Sb_2Te_3 Films Deposited by Close Space

Vapor Transport, *Semicond. Sci. Technol.* **24**(2), 1 (2009). DOI: http://dx.doi.org/ 10.1088/0268-1242/24/2/025025

38. Z.-H. Zheng, P. Fan, G.-X. Lang, D.-P. Zhang, X.-M. Cai, and T.-B. Chen, Annealing Temperature Influence on Electrical Properties of Ion Beam Sputtered Bi_2Te_3 Thin Films, *J. Phys. Chem. Solids*. **71** (12), 1713 (2010). DOI: http://dx.doi.org/ 10.1016/j.jpcs.2010.09.012
39. Y. Deng, Zh. Zhang, Y. Wang, Y. Xu, Preferential Growth of Bi_2Te_3 Films with a Nanolayers Structure: Enhancement of Thermoelectric Properties Induced by Nanocrystal Boundaries, *J. Nanopart. Res*. **14**, 775 (2012). DOI: http://dx.doi.org/ 10.1007/s11051-012-0775-y
40. J. Krumrain, G.Mussler, S. Borisova, T. Stoica, L. Plucinski, C.M. Schneider, and D. Grutzmacher, MBE Growth Optimization of Topological Insulator Bi_2Te_3 Films, *J.Crystal Growth* **324**(1), 115 (2011). DOI: http://dx.doi.org/ 10.1016/j.jcrysgro.2011.03.008
41. A. Giani, F. Pascal-Delannoy, A. Boyer, A. Foucaran, M. Gschwind, and P. Ancey, Elaboration of Bi_2Te_3 by Metal Organic Chemical Vapor Deposition, *Thin Solid Films* **303**, (1-2), (1997) . DOI: http://dx.doi.org/10.1016/S0040-6090(97)00089-8
42. A. Dauscher, A. Thomy, amd H.Scherrer, Pulsed Laser Deposition of Bi2Te3 Thin Films, *Thin Solid Films* **280**(1-2), 61 (1996). DOI: http://dx.doi.org/10.1016/0040-6090(95)08221-2
43. Li Bassi, A. Bailini, C. S. Casari, F. Donati, A. Mantegazza, M. Passoni, V. Russo, and C. E. Bottani, Thermoelectric Properties of Bi–Te Films with Controlled Structure and Morphology, *J. Appl. Phys*. **105**(12), 124307 (2009). DOI: http://dx.doi.org/ 10.1063/1.3147870.
44. R. S. Makala, K. Jagannadham, and B.C. Sales, Pulsed Laser Deposition of Bi_2Te_3-Based Thermoelectric Thin Films, *J. Appl Phys* **94** (6), 3907 (2003). DOI: http://dx.doi.org/ 10.1063/1.1600524
45. F. Volklein, V. Baier, U.Dillner, and E. Kessler, Transport Properties of Flash-Evaporated $(Bi_{1-x}Sb_x)_2Te_3$ Films I: Optimization of Film Properties, *Thin Solid Films* **187** (2), 253 (1990). DOI: http://dx.doi.org/10.1016/0040-6090(90)90047-H.
46. Powder Diffraction File, *Joint Committee on Powder Diffraction Standards* (Philadelphia, PA: ASTM, 1967).

Submitted 16.04.2015.

L.N.Vikhor

L.N. Vikhor, P.V. Gorsky

Institute of Thermoelectricity of the NAS and MES of
Ukraine, 1, Nauky Str.,
Chernivtsi, 58000, Ukraine

P.V.Gorsky

ELECTRICAL RESISTANCE OF THERMOELECTRIC MATERIAL-METAL CONTACT

In the framework of percolation theory in the model of the Anderson chart of random links calculated is the bulk resistance and thermoEMF of transient contact layer "thermoelectric material (TEM)-metal" as a semiconductor material with diffused metal particles. Optimal diffusion profile of metal particles in transient layer is determined from considerations of maximum power factor. Following this, the electrical contact resistance is calculated both for a perfect collection and with regard to different from unity collection coefficient of metal connecting electrode. With a perfect collection it turns out that the value of contact resistance of soldered contacts for the most common solders in thermoelectricity does not exceed $9\cdot10^{-7}$ Ohm·cm^2. With regard to collection coefficient of metal electrode it turns out that for the considered solders and TEM the electrical contact resistance does not exceed $2.0\cdot10^{-4}$Ohm·cm^2. The main reason for a drastic reduction of this resistance value in the framework of existing theoretical approaches is neglect of the fact of smallness of connecting electrode collection coefficient.

Key words: contact, soldering, contact resistance, transient layer, percolation theory, diffusion profile, screening length, density of conducting dislocations, collection coefficient

Introduction

Thermal and electrical contact resistances are essential parameters of thermoelectric devices producing a dramatic effect on their final characteristics, such as generated power, efficiency, etc. At the same time, theory of thermoelectricity lacks approaches that would reliably estimate these resistances and experimental methods of their measurement often suffer from too many errors. Owing to this fact, designers of thermoelectric devices are forced to “assign” certain “guess” values of these resistances to ensure a satisfactory agreement between the predicted output parameters of devices and the experimentally observed ones.

In the framework of existing theoretical approaches [1, 2] the electrical contact resistances for the most part considered as “emission” ones, are often drastically underrated as compared to these “guess” or “experimental” values. Eventually, these resistances are calculated by rather simple formula:

$$\rho_c = \rho_b d\,, \tag{1}$$

where ρ_b is the bulk resistance of transient layer, d – its thickness. However, this formula is valid only in the case when connecting electrode ideally collects charge carriers, i.e. its entire area is active. In fact, this is by no means always the case, so formula (1) must be modified, i.e. written in the form:

$$\rho_c = \frac{\rho_b d}{K_c}\,. \tag{2}$$

In this formula, K_c is coefficient of charge carrier collection which, as it will be clear from the subsequent, is considerably lower than unity. Thus, the purpose of this paper is to estimate TEM-metal contact resistance with and without consideration of collection coefficient.

Analysis of a physical model of transient layer

A physical model of transient layer is shown in Fig.1.

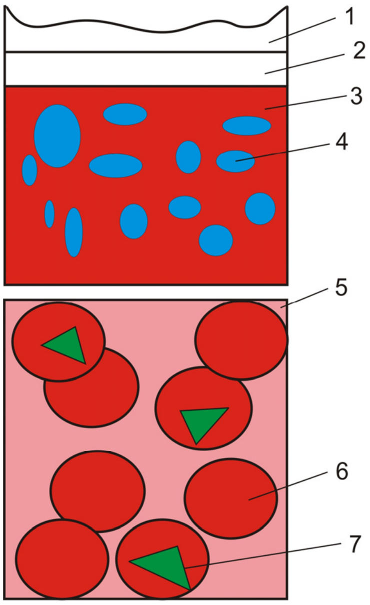

Fig.1. A physical model of transient layer:1-connecting electrode;2-barrier layer, 3-TEM;4-diffused metal particles;5-interface plane; 6-Debye sphere; 7-conducting dislocation perpendicular to interface.

This model takes into account diffusion of metal particles in TEM, and the lower part of the figure serves to explain the physical meaning of collection coefficient (see below). Their electric resistivity will be assumed to be equal to the electric resistivity of metal. Thus, transient layer can be regarded as TEM with metal particles distributed in the depth. Collection coefficient K_c is determined by the possibility of reaching the connecting electrode by charge carriers owing to their motion along conducting dislocations perpendicular to interface. But due to shielding of electrostatic attraction between the dislocation and charge carriers, only those carriers can arrive at it that are at a distance from the dislocation line which does not exceed the Debye shielding length. Thus, if each Debye sphere within the area of connecting electrode has one or more dislocations, collection is perfect. As to the figure, it corresponds to imperfect collection, i.e. to the case of $K_c < 1$. Owing to this, we first determine contact resistance at $K_c = 1$, and then correct it on the basis of the results of calculation of K_c.

Calculation of contact resistance with a perfect collection

To calculate contact resistance, we must first determine the electric resistivity of transient layer. For this purpose we will need the ratio determining the distribution of metal particles in the depth of the layer. It can be rigorously found only from diffusion equation, however, to write, the more so to solve this equation for the real process of creating a contact, for instance, by soldering method, is rather difficult. Therefore, we will use a simplified simulation approach and write the distribution $p(x)$ of a relative volumetric share of metal particles in a transient layer as follows:

$$p(x) = 1 - (x/d)^{\delta}. \tag{3}$$

“Shape parameter” δ characterizes “blurring” of transient layer. The value $\delta = 0$ corresponds to the absence of transient layer, i.e. to a perfect flat TEM-metal contact with a sharp boundary, and the value $\delta \to \infty$ corresponds to full substitution of transient layer by metal. The value $\delta = 1$ corresponds to the case of steady-state diffusion of metal in TEM with a constant diffusion factor.

With this distribution, the bulk kinetic coefficients of transient layer, namely electrical conductivity σ, thermal conductivity κ and thermoEMF α in the framework of percolation theory [3, 4] can be determined as:

$$\begin{pmatrix}\sigma\\ \kappa\end{pmatrix} \Bigg/ \begin{pmatrix}\sigma_M\\ \kappa_M\end{pmatrix} = \int_0^1 0.25\left(R - 3p^{\delta} - n_{\sigma,\kappa} + 3n_{\sigma,\kappa}p^{\delta} + 2\right)dp, \tag{4}$$

$$\alpha = \int_0^1 \frac{\left(1-p^{\delta}\right)\sigma_M\alpha_M\left(2\sigma+\sigma_{TE}\right)\left(2\kappa+\kappa_{TE}\right) + p^{\delta}\sigma_{TE}\alpha_{TE}\left(2\sigma+\sigma_M\right)\left(2\kappa+\kappa_M\right)}{\left(1-p^{\delta}\right)\sigma_M\left(2\sigma+\sigma_{TE}\right)\left(2\kappa+\kappa_{TE}\right) + p^{\delta}\sigma_{TE}\left(2\sigma+\sigma_M\right)\left(2\kappa+\kappa_M\right)}dp. \tag{5}$$

where:

$$R = \sqrt{9n_{\sigma,\kappa}^2 p^{2\delta} - 6n_{\sigma,\kappa}^2 p^{\delta} + n_{\sigma,\kappa}^2 - 18n_{\sigma,\kappa}p^{2\delta} + 18n_{\sigma,\kappa}p^{\delta} + 4n_{\sigma,\kappa} + 9p^{2\delta} - 12p^{\delta} + 4}, \tag{6}$$

In formulae (4) – (6), $\sigma_M, \sigma_{TE}, \kappa_M, \kappa_{TE}, \alpha_M, \alpha_{TE}$ are electrical conductivities, thermal conductivities and thermoEMF of metal and thermoelectric material, respectively, $n_{\sigma} = \sigma_{TE}/\sigma_M$, $n_{\kappa} = \kappa_{TE}/\kappa_M$.

Analysis shows that for given parameters of TEM and metal there is such a value of diffusion profile “shape parameter” δ_0 whereby maximum power factor $P = \alpha^2\sigma$ is achieved. In so doing, maximum thermoelectric figure of merit need not be achieved, since the ratio of electrical conductivity to thermal conductivity is weakly dependent on δ, and thermoEMF value with increase in δ is decreased, as long as replacement of semiconductor by metal should reduce it. Therefore, the resistivity of “optimized in power factor” contact layer is:

$$\rho_{b0} = \left[\sigma_M \int_0^1 0.25\left(R_0 - 3p^{\delta_0} - n_{\sigma} + 3n_{\sigma}p^{\delta_0} + 2\right)dp\right]^{-1}, \tag{7}$$

where:

$$R_0 = \sqrt{9n_{\sigma}^2 p^{2\delta_0} - 6n_{\sigma}^2 p^{\delta_0} + n_{\sigma}^2 - 18n_{\sigma}p^{2\delta_0} + 18n_{\sigma}p^{\delta_0} + 4n_{\sigma} + 9p^{2\delta_0} - 12p^{\delta_0} + 4}. \tag{8}$$

Hence, with a perfect collection contact resistance is equal to $\rho_{b0}d$.

Correction of contact resistance with regard to collection coefficient

Traditionally [5, 6], collection coefficient is determined by the formula:

$$K_c = \pi L_D^2 N_D. \tag{9}$$

In this formula, L_D is the Debye shielding length of electric potential, N_D is the density of conducting dislocations perpendicular to interface. This formula for collection coefficient has a simple physical meaning. Namely, collection coefficient is nothing but the averaged number of conducting dislocations in the electrode area perpendicular to interface and nevertheless getting into the Debye sphere of electrical potential shielding, which quite fits the above analyzed physical model. From the solution of the Poisson equation for a system of major charge carriers in TEM in the approximation linear in desired potential with regard to degeneracy degree follows the expression for L_D:

$$L_D^2 = \frac{\varepsilon\varepsilon_0 h^3}{8\pi\sqrt{2kT}e^2 m^{*3/2}}\left[\int_0^\infty \frac{\sqrt{x}\exp(x-\eta)}{\exp(x-\eta)+1}dx\right]^{-1}, \tag{10}$$

Parameter η characterizing chemical potential of free charge carrier system is found from the equation:

$$n_0 = \frac{8\pi\sqrt{2}\left(m^* kT\right)^{3/2}}{h^3}\int_0^\infty \frac{\sqrt{x}}{\exp(x-\eta)+1}dx. \tag{11}$$

In formulae (10) – (11), ε is dielectric constant of TEM, T is absolute temperature, n_0 is the bulk concentration of charge carriers in TEM, m^* is density-of-state effective mass, the rest of notations are generally accepted.

Calculation of contact resistance value

Let us apply the obtained general results to evaluation of the electrical resistance of TEM-metal contact created by soldering method. We will take into account the fact that at present soldering for creation of contacts in the manufacture of thermoelectric modules is done by such solders as eutectic alloys of bismuth with tin (melting temperature 135°C) or lead with tin (181°C), as well as pure tin (230°C), or tin with small additions of silver (217°C) or antimony (240°C). Let us determine the expected electric resistances of contacts obtained at soldering with these solders. In so doing, the influence of anti-diffusion sublayer will be ignored. Solder parameters which are necessary for the calculation, namely electric conductivity, thermal conductivity and thermoEMF also will be determined in the framework of percolation theory, based on their composition and known parameters of their constituent elements. We have to do it, since the reliable values of *all* kinetic coefficients of solders are unknown.

The plots of dependences of power factor on diffusion profile shape parameter and optimal diffusion profiles of transient layers for different TEM-solder pairs with regard to TEM parameters [7] and calculated parameters of solders are shown in Fig. 2-6.

The expected values of contact resistances for the above contact pairs at thicknesses of "optimized layers" equal to 25μm are given in Table 1.

We see that the obtained estimates of contact resistance with a perfect collection are more than an order higher than those proposed, for instance, in [1, 2]. Therefore, it seems reasonable to compare them to certain experimental data. For instance, in [8] it is shown that by doping of a near-contact layer in materials of $(Bi, Sb)_2(Se,Te)_3$ system donor impurities of iodine or acceptor impurities of silver one can obtain for *p* and *n*-type materials the electrical contact resistances of the order of $2.7\cdot10^{-7}$ and $4.5\cdot10^{-7}$ Ohm·cm^2, respectively. Thus, in this case a transient layer is close to optimal, and collection coefficient – to unity. On the other hand, the values of contact resistance obtained with regard to difference of collection coefficient from unity are approximately in the limits given in [1], where it is mentioned that soldered contacts have resistances of the order of 10^{-4} Ohm·cm^2 or less.

In this case the resistance of "metal" part of the contacts, i.e. solder-copper pairs, can be ignored. As regards comparison of the results to some other experimental data, note that the reference book [9] for soldered contacts of similar thermoelectric material with copper indicates electrical contact resistance of the order of 10^{-5} Ohm·cm^2 or less. On the other hand, contact resistance measurements by "block" method in thermoelectric cooling mode [10] show that with the aid of improved processes of soldered contacts creation this resistance can be reduced at 300 K to $1.3\cdot10^{-6}$ Ohm·cm^2 for *p*-type Bi_2Te_3 and

$1.12\cdot10^{-6}$ Ohm·cm^2 for *n*-type Bi_2Te_3, which is close to “perfect” calculated contact resistance of $(Bi_2Se_3)_{0.04}(Bi_{0.5}Sb_{1.5}Te_3)_{0.96}$-*Bi-Sn* pair corresponding to $K_c = 1$.

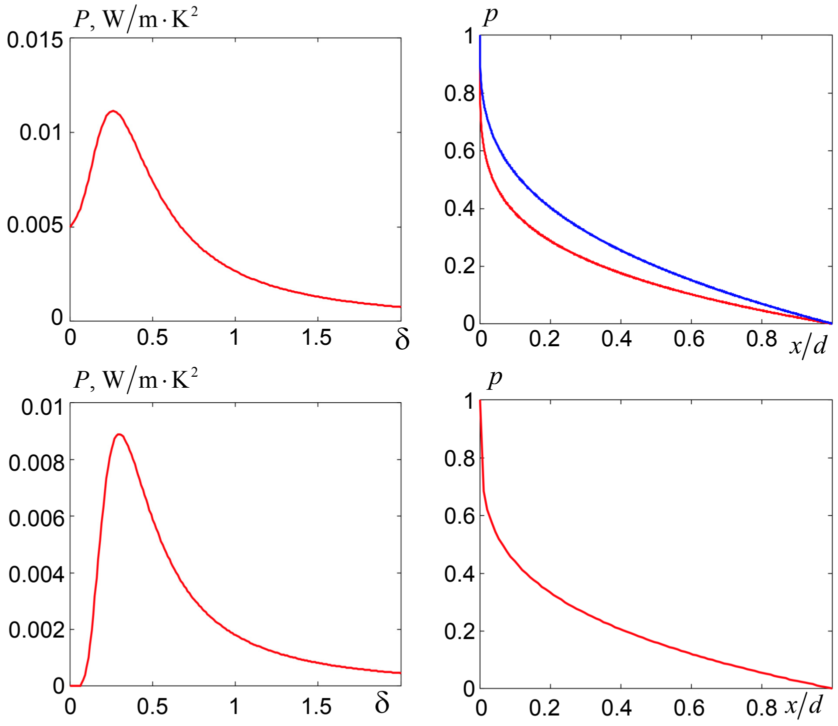

Fig. 2. Dependence of power factor on shape parameter (a) and optimal diffusion profile (b) for contact pair $Bi_{0.5}Sb_{1.5}Te_3$-Sn; c, d- the same dependences for contact pair $(Bi_2Se_3)_{0.04}(Bi_{0.5}Sb_{1.5}Te_3)_{0.96}$-Sn. Two curves in Fig.2b and subsequent similar figures denote that optimum is attained not at one δ value, but in a certain interval wherein power factor changes slowly.

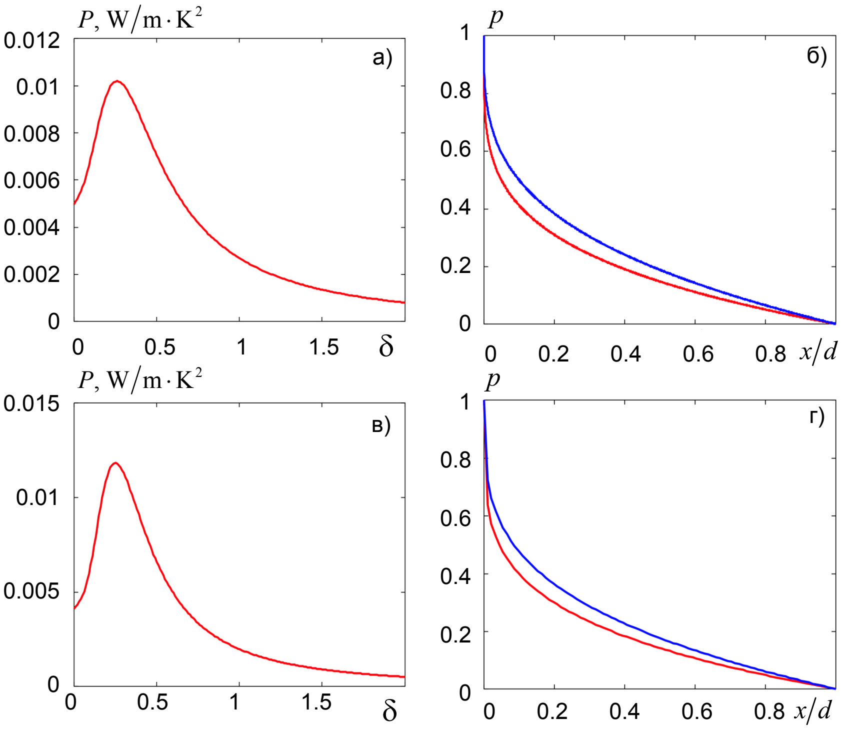

Fig.3. The same dependences as in Fig.2, but for contact pairs $Bi_{0.5}Sb_{1.5}Te_3$-Sn-Pb (a,b) and $(Bi_2Se_3)_{0.04}(Bi_{0.5}Sb_{1.5}Te_3)_{0.96}$-Sn-Pb (c,d).

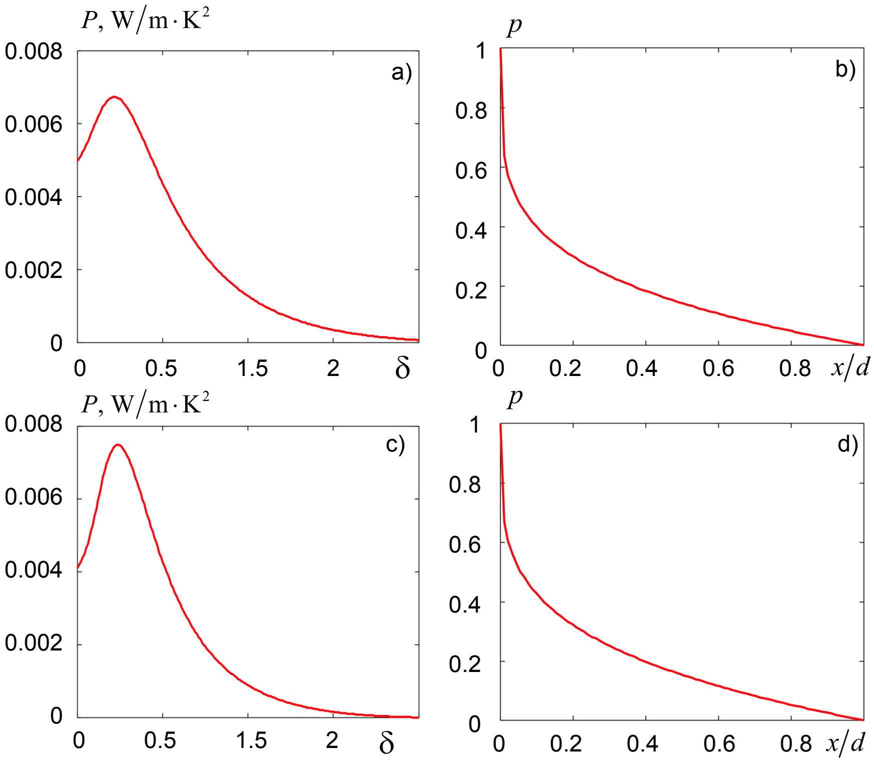

Fig. 4. The same dependences as in Fig. 2, but for contact pairs $Bi_{0.5}Sb_{1.5}Te_3$ *-Bi-Sn (a, b) and* $(Bi_2Se_3)_{0.04}(Bi_{0.5}Sb_{1.5}Te_3)_{0.96}$*-Bi-Sn (c, d).*

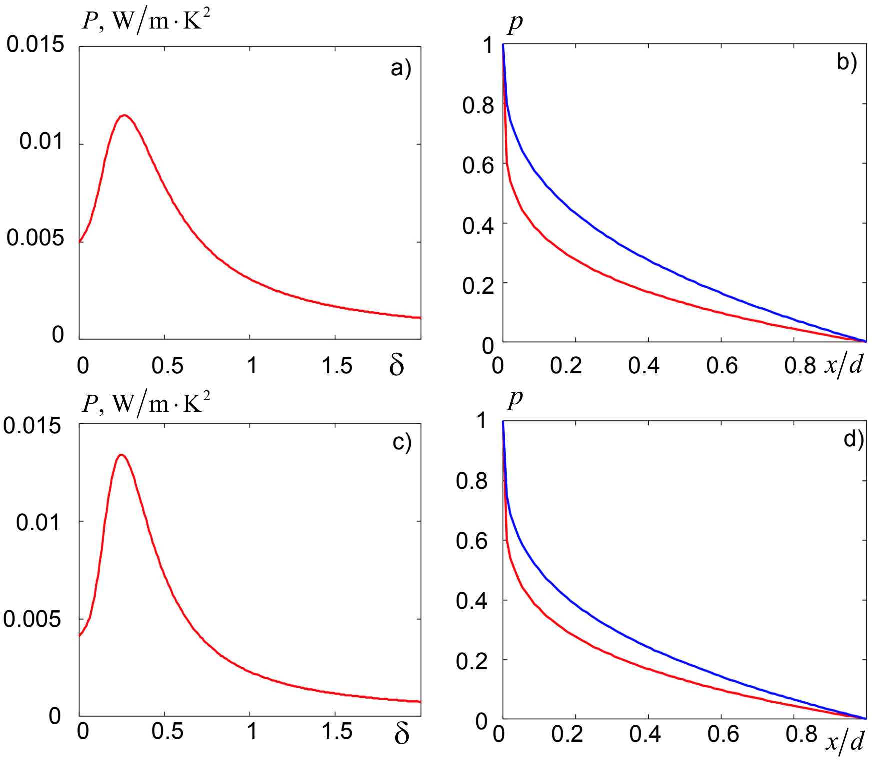

Fig. 5. The same dependences as in Fig. 2, but for contact pairs $Bi_{0.5}Sb_{1.5}Te_3$*–(Sn+Ag) (a, b) and* $(Bi_2Se_3)_{0.04}(Bi_{0.5}Sb_{1.5}Te_3)_{0.96}$*-(Sn+Ag) (c, d).*

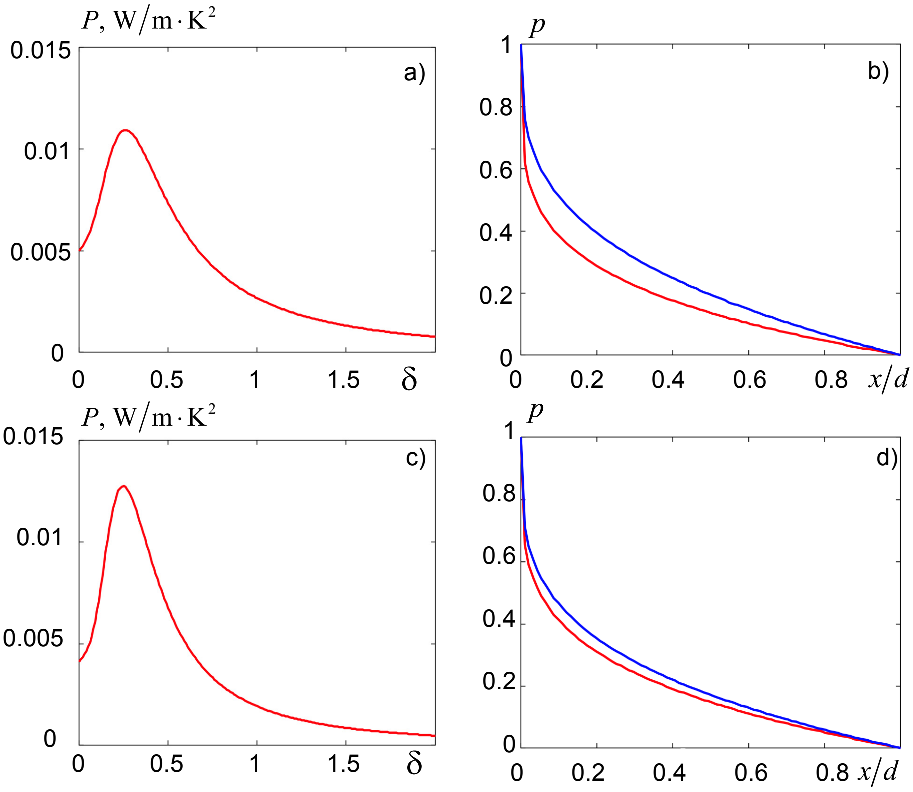

Fig.6. The same dependences as in Fig. 2, but for contact pairs $Bi_{0.5}Sb_{1.5}Te_3$*–(Sn+Sb) (a, b) and* $(Bi_2Se_3)_{0.04}(Bi_{0.5}Sb_{1.5}Te_3)_{0.96}$*-(Sn+Sb) (c, d).*

Table 1.

Expected values of contact resistances

Contact pair	Contact resistance in Ohm·cm²	
	With a perfect collection	With collection coefficient lower than 1
$Bi_{0.5}Sb_{1.5}Te_3$-Sn	$(2.70\text{-}4.63)\cdot10^{-7}$	$8.45\cdot10^{-5}\text{-}1.45\cdot10^{-4}$
$(Bi_2Se_3)_{0.04}(Bi_{0.5}Sb_{1.5}Te_3)_{0.96}$-Sn	$3.64\cdot10^{-7}$	$4.74\cdot10^{-5}$
$Bi_{0.5}Sb_{1.5}Te_3$-Sn-Pb	$(3.26\text{-}4.48)\cdot10^{-7}$	$(1.02\text{-}1.40)\cdot10^{-4}$
$(Bi_2Se_3)_{0.04}(Bi_{0.5}Sb_{1.5}Te_3)_{0.96}$-Sn-Pb	$(4.58\text{-}6.67)\cdot10^{-7}$	$(5.96\text{-}8.69)\cdot10^{-5}$
$Bi_{0.5}Sb_{1.5}Te_3$-Bi-Sn	$6.53\cdot10^{-7}$	$2.04\cdot10^{-4}$
$(Bi_2Se_3)_{0.04}(Bi_{0.5}Sb_{1.5}Te_3)_{0.96}$-Bi-Sn	$9.04\cdot10^{-7}$	$1.18\cdot10^{-4}$
$Bi_{0.5}Sb_{1.5}Te_3$-(Sn+Ag)	$(2.35\text{-}4.81)\cdot10^{-7}$	$7.33\cdot10^{-5}\text{-}1.50\cdot10^{-4}$
$(Bi_2Se_3)_{0.04}(Bi_{0.5}Sb_{1.5}Te_3)_{0.96}$-(Sn+Ag)	$(3.53\text{-}6.90)\cdot10^{-7}$	$(4.60\text{-}8.99)\cdot10^{-5}$
$Bi_{0.5}Sb_{1.5}Te_3$-(Sn+Sb)	$(2.89\text{-}4.70)\cdot10^{-7}$	$9.02\cdot10^{-5}\text{-}1.47\cdot10^{-4}$
$(Bi_2Se_3)_{0.04}(Bi_{0.5}Sb_{1.5}Te_3)_{0.96}$-(Sn+Sb)	$(4.43\text{-}5.75)\cdot10^{-7}$	$(5.78\text{-}7.49)\cdot10^{-5}$

Remarks: 1) For contact pairs for which optimum is attained in a certain range of values δ, the indicated contact resistance values correspond to the ends of this range. 2) In the calculation of collection coefficients, the density of conducting dislocations perpendicular to interface was taken to be equal to $10^{11}\,cm^{-2}$*.*

Conclusions

1. The main reason for a drastic discrepancy between theoretical and observed electrical resistance values of TEM-metal contacts created by means of soldering is neglect of the fact of smallness of coefficient of charge carrier collection by metal electrode.
2. If charge carrier collection coefficient were equal to 1, the electrical resistance of TEM-metal contact created by soldering with the use of the most common solders would be $(2.35–9.04)\cdot10^{-7}$ Ohm·cm^2.
3. With regard to collection coefficient smallness, the upper assessed value of the above contact resistance of soldered contact is $2.04\cdot10^{-4}$ Ohm·cm^2.

The Authors are grateful to academician L.I. Anatychuk for the formulation of the problem and helpful constructive discussion of the results of the work contributing to its quality enhancement.

References

1. L.W. Da Silva, M. Kaviany, Micro-Thermoelectric Cooler: Interfacial Effects on Thermal and Electrical Transport, *Int. J. Heat and Mass Transfer* **478,** 2417-2435 (2004).
2. L.I. Anatychuk, V.K. Dugaev, V.I. Litvinov, and V.L. Volkov, Contact Resistance between Metal and Thermoelectric Material, *J.Thermoelectricity* **1**, 70-77 (1994).
3. J. Zaiman, *Disorder Models* (Moscow: Mir, 1982), 592 p.
4. A.A. Snarskii, M.I. Zhenirovsky, and I.V. Bezsudnov, On the Wiedemann-Franz Law in Thermoelectric Composites, *J.Thermoelectricity* **3**, 59-65 (2006).
5. A.V. Sachenko, A.E. Belyaev, N.S. Boltovets, V.N. Ivanov, R.V. Konakova, Ya.Ya. Kudrik, L.A. Matveeva, V.V. Milenin, S.V. Novitsky, and V.N. Sheremet, Effect of Microwave Irradiation on the Resistance of Au-TiB$_x$-Ge-Au-n-n$^+$-n^{++}-GaAs(InP) Ohmic Contacts, *Semiconductors* **46**(4), 558-561 (2012).
6. T.V. Blank, Yu.A. Goldberg, and E.A. Popov, Current Flow along Metal Shunts in Ohmic Contacts to Wide-Gap Semiconductors $A^{III}B^{V}$, *Semiconductors* **43**(9), 1204-1209 (2009).
7. L.D.I vanova, Yu.V. Granatkina, A. Dauscher, B. Lenoir, and H. Sherrer, Influence of the Purity and Perfection of Czochralski-Grown Single Crystals of Bismuth and Antimony Chalcogenides Solid Solution on their Thermoelectric Properties, *Proc. of 5th European Workshop on Thermoelectrics (Pardubice, Czech Republic, 1999), p.175-178.*
8. P.J. Taylor, J.R. Maddux, G. Meissner, R. Venkatasubramanian, G. Bulman, J. Piers, R. Gupta, J. Biershenk, C. Caylor, J. D'Angelo, and Zh. Ren, Controlled Improvement in Specific Contact Resistivity for Thermoelectric Materials by Ion Implantation, *Appl. Phys. Let.* **103** (043902), 1-4 (2013).
9. L.I. Anatychuk, *Thermoelements and Thermoelectric Devices*, *Reference Book* (Kyiv: Naukova Dumka, 1979), 764 p.
10. R.P. Gupta, R. McCarty, and J. Sharp, Practical Contact Resistance Measurement Method for Bulk Bi_2Te_3 Based Thermoelectric Devices, *J. El. Mat.*,Oct.2013, doi 10.1007/s11664-013-2806-6.

Submitted 27.04.2015.

S.I.Menshikova[1], E.I.Rogacheva[1], A.Yu.Sipatov[1], S.I.Krivonogov[2], P.V.Matychenko[2]

[1]National Technical University “Kharkiv Polytechnic Institute”,
21 Frunze St., Kharkiv 61002, Ukraine
[2]Institute for Single Crystals NAS of Ukraine, 60 Lenin Ave., Kharkiv, 61001, Ukraine

SIZE EFFECTS IN CHLORINE DOPED *PbSe* THIN FILMS

The possibility of obtaining strongly degenerate (≈ $3\cdot10^{20}$ cm^{-3}) PbSe thin films (d = 5 – 220 nm) with n-type conductivity by thermal evaporation in vacuum of PbSe crystals doped with $PbCl_2$, with subsequent condensation onto (001) KCl substrates was established. It was shown that the films had high homogeneity degree, no grain structure was observed. The thickness dependences of thermoelectric properties (the Seebeck coefficient S, the Hall coefficient R_H and the electric conductivity σ) of thin films were obtained. In the thickness range d ≈ 5 ÷ 30 nm, oscillation properties were observed with growth of d that are attributable to electron gas quantization. The calculation of S(d) dependence on the assumption of size quantization with regard to contribution of several subbands and the thickness dependence of the Fermi energy was shown to be in agreement with the experimental data. In the region of d > 30 nm there was growth of S and σ with thickness, which is attributable to manifestation of classical size effect and interpreted in the framework of Fuchs-Sondheimer and Mayer theories.

Key words: lead selenide, thin film, thickness, size effect.

Introduction

As is known, the range of application of IV-VI semiconductors is very wide: IR engineering [1], lasers [2], solar cells [3], thermoelectricity (TE) [4] and other fields of science and technology [5]. Lead selenide (*PbSe*) has proved itself as material used in thermoelectric power converters (thermal generators) [6]. Efficient use of *PbSe* is possible at high concentrations of charge carriers ($n \sim 2\text{-}3\cdot10^{19}$ cm^{-3}) which do not seem possible to be obtained due to deviations from stoichiometry. In this connection, *PbSe* is doped with different impurities. Introduction of chlorine, iodine, sodium, bismuth into *PbSe* lattice allows achieving concentration values up to ~ 10^{20} - 10^{21} cm^{-3} [6].

Increase in TE figure of merit of material which is in a low-dimensional state was experimentally shown for superlattices based on IV-VI compounds [7, 8]. With practical application of thin films, it is important to take into account the influence of size effects (classical and quantum) that can change drastically the kinetic properties of material [9].

Quantum size effects (QSE) manifested in the oscillations of galvanomagnetic and TE properties with growth in film thickness, were observed in *PbX* films (*X* = *S*, *Se*, *Te*) with *n*-type conductivity and concentration ~ 10^{18} cm^{-3} [10-13] and in *PbTe* films with high degeneracy degree of the hole ($p \sim 10^{19}$ cm^{-3}) [14] and electron ($n \sim 10^{20}$ cm^{-3}) charge carrier gases [15]. For *PbSe* films obtained by thermal evaporation in vacuum of crystals of stoichiometric *PbSe* with hole concentration $p \sim 10^{18}$ cm^{-3}, there was increase in the electric conductivity and mobility with growth of film thickness, which was attributed to manifestation of classical size effect (ClSE) [16, 17]. By example of PbSe films the possibility of a simultaneous investigation of ClSE and QSE on the same object by changing film thickness was shown [17].

Few works are concerned with the investigation of the thickness dependences of TE properties of *PbSe* films with a high degree of electron gas degeneracy. In [18] we showed that chlorine-doped *PbSe* films show a complicated dependence of TE properties on film thickness, and an assumption was made on the superposition of QSE and ClSE.

The purpose of this paper is to study in more detail the influence of thickness d of *PbSe* films with a high degree of electron gas degeneracy ($n = 3{\cdot}10^{20}$ cm^{-3}) on their TE properties at room temperature.

Procedure

PbSe films with thicknesses d = 5-220 nm were obtained by the method of thermal evaporation in vacuum (10^{-5}-10^{-6} Pa) of *PbSe* crystals doped with 2 mol.% $PbCl_2$, with subsequent condensation onto (001) *KCl* cleavages, maintained at a temperature of (520 ± 10) K. Using electron beam method, the films were coated by Al_2O_3 layer 20-25 nm thick. The thickness d of the films was controlled with the aid of precalibrated quartz resonator.

Surface morphology and chemical composition of the films were studied by means of electron probe microanalysis with the use of scanning electron microscope JSM-6390 LV (Jeol, Japan) with a system of energy-dispersive spectrometer X-Max^n 50 (Oxford Inst., United Kingdom) with accelerating voltage 10 kV. Surface morphology and average roughness were studied by means of atomic force microscope (AFM) Solver Pro NT-MDT with Nova software, the images were obtained in the air in contact mode.

The electric conductivity σ and the Hall coefficient R_H were measured by standard *dc* method with an error not exceeding 5 %. As material for soldering of contacts, use was made of indium. The Hall concentration of charge carriers n was calculated on the assumption of one sort of carriers by the formula $n = r/R_H{\cdot}e$, where the Hall factor $r = 1$, e is electron charge. The Hall mobility μ_H was calculated as $\mu_H = R_H \cdot \sigma$. The Seebeck coefficient S was measured by the compensation method with respect to copper to an accuracy of ± 3 %. The type of charge carriers was determined by the sign of R_H and S.

Theoretical calculation for the description of oscillating character of $S(d)$ dependence was made with the use of mathematical package Maple 15; dependences of S and σ on the thickness of films were calculated in the framework Fuchs-Sondheimer and Mayer theories with the use of mathematical package MatLAB 6.5.

Results

Measurements of R_H and S have shown that the films possess n-type conductivity over the entire range of studied thicknesses, just as $PbSe\langle PbCl_2\rangle$ crystal which was used as a charge for preparation of films. For the crystal the following values of kinetic coefficients were obtained: S = 20 μV/K, σ = 4600 (Ohm·cm)$^{-1}$, $n = 3 \cdot 10^{20}$ cm^{-3}, μ_H = 100 cm^2/(V·s). In the films one succeeded to reach 2-4 fold values of n and the values of mobility comparable to crystal μ_H . The electron conductivity type and high values of carrier concentration result from the introduction of chlorine into *PbSe* lattice and agree with the data reported in the literature [6].

Electron probe microanalysis of films surface in the mode of scanning over the area and probing by points has shown that the films possessed high degree of homogeneity on the microlevel (the ratio between the elements (*Pb*, *Se*, *Cl*) from one analyzed area to another was retained within the error of the method). Studies in the mode of secondary electrons (resolution 10 nm) have shown that no grain structure was observed in the films and the surface was homogeneous (Fig. 1).

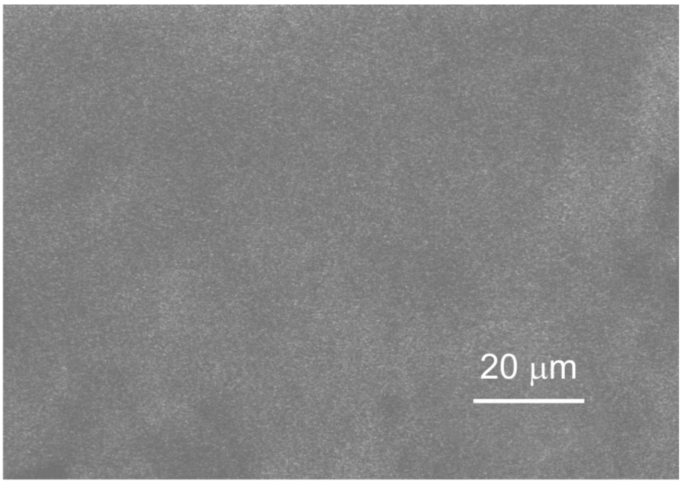

Fig. 1. Surface micro image of film with thickness d = 220 nm.

The results of AFM investigation of the films surface are given in Fig. 2. As is seen, the surface of the films is mostly smooth, though one can observe elongated asperities along <100> direction, with a flat apex (Fig. 2). The height of asperities was ≈ 12-18 nm, the base width did not exceed 40 ÷ 60 nm, and the length – 170 ÷ 240 nm. The average distance between the asperities was ≈ 350 nm. Note that the value of average roughness in the area between the asperities was R_a ≈ 1.03 nm. One of possible reasons for the appearance of asperities can be inheritance by $PbSe\langle PbCl_2\rangle$ layer of substrate surface, owing to which along the surface steps there appear dislocations penetrating the film and outcropping to the surface as asperities.

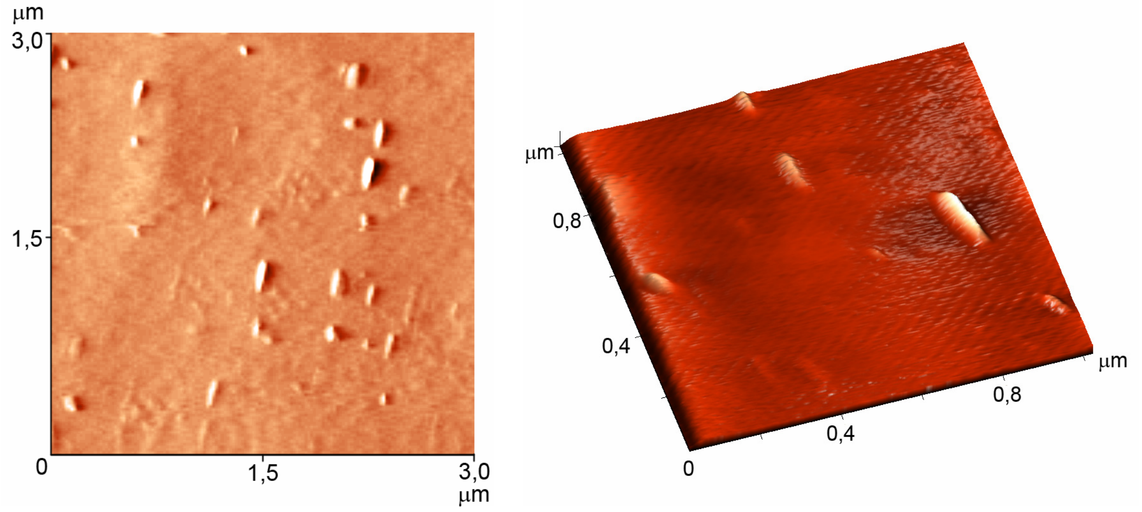

(*a*) (*b*)

Fig. 2. AFM-topography (a) and 3D AFM surface image (b) of film with thickness d = 56 nm.

It is known that in lead chalcogenides films grown in alkali-halide crystals the dominant effects are dislocations sliding in (100) plane [19, 20]. According to the data from transparent electron microscopy, the dislocation density in *PbTe* films grown on *KCl* cleavages is generally equal to ≈ $10^8 cm^{-2}$ [19]. Assuming that elongated along <100> direction structures in Fig. 2, *a* are outcropping dislocations, one can determine their density. Evaluation of the density of dislocations outcropping to film surface yields the value ≈ $2.5\cdot10^8$ cm^{-2} which is in good agreement with the literature data [20].

Thus, it can be assumed that the asperities on the surface of films are caused by dislocations appearing along the surface steps due to inheritance of substrate surface, arranged at quite a distance from each other (≈ 350 nm). Nevertheless, *PbSe<PbCl*$_2$*>* films are characterized by high level of homogeneity (Fig. 1), smooth surface and absence of macrodefects (cracks and pores, etc.).

Fig. 3 shows dependences of S, σ and R_H on the thickness of films at room temperature, black squares are used to mark the values of kinetic coefficients of crystal which served as a charge for preparation of films. On dependences $S(d)$, $R_H(d)$ and σ(d) one can see extremes at thicknesses 8, 11, 15, 18 and 23 nm, the maxima on the curve σ(d) corresponding to minima on dependences $S(d)$ and $R_H(d)$ and vice versa. The average distance between the two neighbouring minima or two maxima is Δd = (7 ± 1) nm. In the area d > ~ 30 nm the kinetic coefficients are monotonically increased with film thickness and tend to the values S, R_H and σ of the crystal.

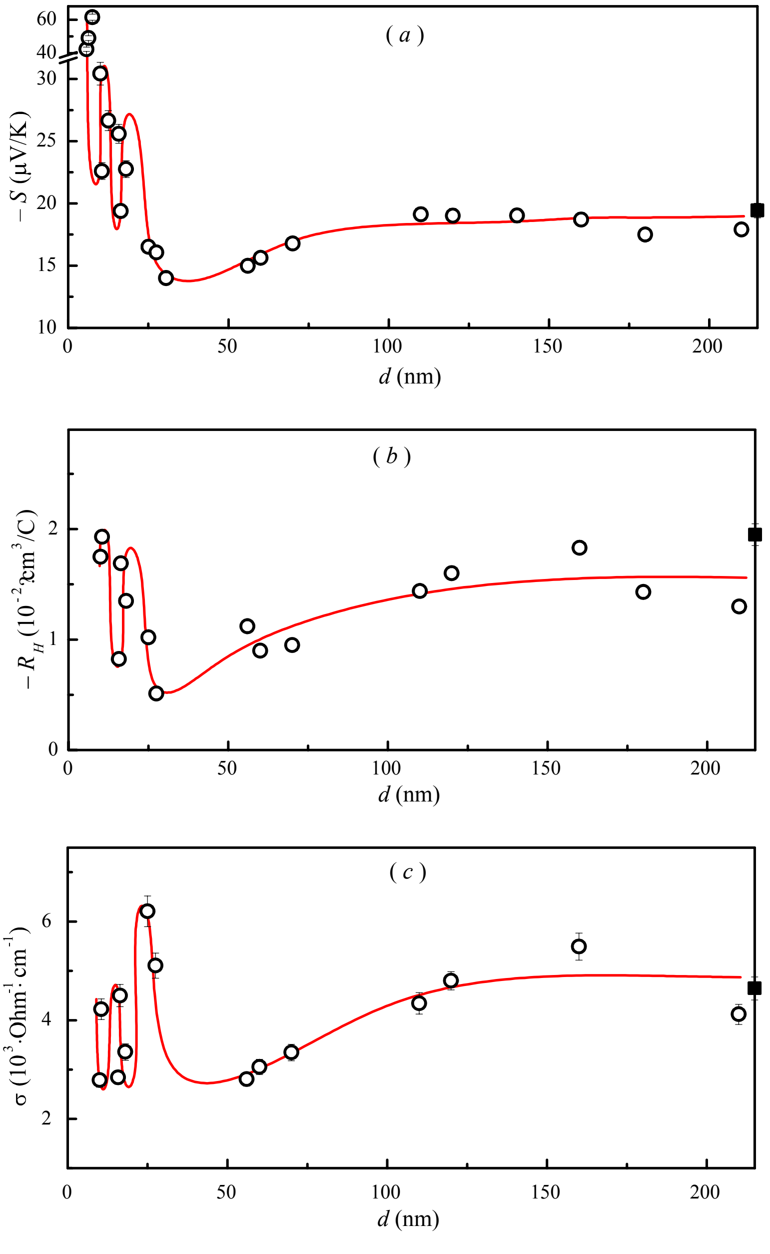

Fig.3. Dependences of the Seebeck coefficient S (a), the Hall coefficient R_H *(b) and the electric conductivity σ (c) on the thickness of PbSe<PbCl*$_2$*> films.*

Rather high structural perfection of the films, their homogeneity and smooth surface suggest that the reason for oscillating character of change in galvanomagnetic and thermoelectric properties of films with growth of d can be QSE.

The $PbSe<PbCl_2>$ film can be presented as a quantum well located between two insulators – KCl substrate and Al_2O_3 protective coating. Electron movement in the direction perpendicular to film surface is restricted, which results in quantization of quasi pulse transverse component and formation of two-dimensional energy subbands. In the other two directions electron quasi-pulse is not quantized. On the assumption that all charge carriers occupy only the lower subband [21] in the approximation of effective mass, assuming square dispersion law, the energy of carriers in quantum size film can be written as follows:

$$E = \frac{\hbar^2}{2m_\perp^*}\frac{\pi^2}{d^2}n^2 + \frac{\hbar^2 k_x^2}{2m_x^*} + \frac{\hbar^2 k_y^2}{2m_y^*}, \qquad (1)$$

where $m_\perp^*$ is effective mass of charge carriers along the direction perpendicular to quantum well, k_x, k_y and m_x*, m_y* are components of wave vector and effective mass, respectively, with motion of charge carriers parallel to quantum well, n is quantum number (n = 1, 2,…). With increase in d, two-dimensional subbands will consecutively cross the Fermi level ε_F, which will involve the oscillating character of change in the density of states. Density of states oscillations will lead to the oscillations of kinetic properties with the period [9]:

$$\Delta d = \frac{h}{\sqrt{8m_\perp^*\varepsilon_F}} \qquad (2)$$

Thickness d_1 whereby the first subband (N = 1) crosses ε_F, coincides with the value Δd [22], so to determine the oscillation period, it is enough to record the position of the first extremum on the thickness dependences of transport properties.

As is known, QSE can be manifested, provided the following conditions are met [9]:

1) the distance between the energy subbands ΔE, determined as $\Delta E = \frac{h^2}{8m_\perp^* d^2}(2n+1)$, must exceed thermal blurring of the levels $\Delta E \geq k_B T$ (k_B is the Boltzmann constant);

2) charge carrier scattering partially blurs quasi-discrete spectrum, so to preserve the quasi-discrete character of spectrum, blurring h/τ (τ is relaxation time) must be smaller than the distance between neighbouring subbands $\Delta E > \frac{\hbar}{\tau} = \frac{h \cdot \mathrm{e}}{2\pi \cdot m \cdot \mu}$;

3) it is necessary to have high quality of surfaces restricting the motion of carriers in quantum wells and reflection specularity, i.e. roughness dimensions must be smaller than the de Broglie wavelength λ_F;

4) nanocrystallite size must exceed thickness d, otherwise charge carriers on grain boundaries will be scattered, and QSE observation will be impossible.

It can be easily demonstrated that in the films under study these conditions are realized. For instance, for *n-PbSe* ($m_\perp^* = 0.04\, m_0$ [6]) film of thickness d = 10 nm the value ΔE at n = 1 is $\Delta E \approx 283$ meV, and thermal blurring of subbands at room temperature k_BT = 25.8 meV, which indicates to fulfillment of the first condition. Rather high values of charge carrier mobility in thin films comparable to the values of μ in crystal, point to the possibility of fulfillment of the second condition. De Broglie wavelength ($\lambda_F = 2\Delta d$) exceeds the value of films roughness ($R_a \approx 1.03$ nm), determined by means of AFM, showing sufficiently high surface quality. The absence of grain structure, confirmed by the results of probe microanalysis, also makes possible the fulfillment of the last condition. The foregoing indicates the possibility of consideration and interpretation of the observed oscillations within the concepts of QSE.

The calculation of quantum oscillation period by formula (2) with regard to the value of transverse component of electron effective mass in *PbSe* [6] and ε_F, determined by the R_H values of crystal, yielded the value $\Delta d = (3 \pm 0.5)$ nm. The resulting value Δd proved to be almost half the experimentally observed average distance between the nearest minima (or maxima) on d-dependences of kinetic coefficients ($\Delta d = 7 \pm 1$ nm). Such a difference can be due to simplifications used in the model of a rectangular potential well with infinitely high walls. Moreover, in the calculation it was assumed that the contribution to kinetic coefficients is only from charge carriers occupying the lower subband, and that the Fermi energy does not depend on the film thickness.

To specify the value Δd, calculation was made with regard to contribution of several energy subbands to the value of the Seebeck coefficient. Using the assumption of the energy independence of charge carrier relaxation time, the expression for the Seeebeck coefficient S in a two-dimensional system can be written as follows [23]:

$$S = \frac{1}{eT}\left(\varepsilon_F - \frac{\sum\limits_{n=1}^{E_n<\varepsilon_F}\int\limits_0 E\varepsilon\left(\frac{\partial f}{\partial \varepsilon}\right)d\varepsilon}{\sum\limits_{n=1}^{E_n<\varepsilon_F}\int\limits_0 \varepsilon\left(\frac{\partial f}{\partial \varepsilon}\right)d\varepsilon}\right), \tag{3}$$

where f is the Fermi distribution function, $\varepsilon = E - E_n$, $E_n = \frac{\pi^2\hbar^2}{2m_\perp^* d^2}N^2$. On rearrangement, the expression for S takes on the form:

$$S = \frac{k_B}{e}\left[\xi - \frac{\beta + \gamma}{\alpha}\right], \tag{4}$$

where $\alpha = \sum\limits_{n=1}^{E_n \le \varepsilon_F}\left(\ln z - y\right)$; $\beta = b\cdot\sum\limits_{n=1}^{E_n \le \varepsilon_F} n^2\cdot\left(\ln z - y\right)$; $\gamma = \sum\limits_{n=1}^{E_n \le \varepsilon_F}\left(2\cdot di\log z + y^2 + \frac{\pi^2}{3}\right)$, $z = 1 + e^{bn^2 - \xi}$, $y = bn^2 - \xi$, $b = \frac{1}{k_B T}\frac{\pi^2\hbar^2}{2m_\perp^* d^2}$, $\xi = \frac{\varepsilon_F}{k_B T}$. Note that in Eq. (4) the summation is done over several energy subbands, and it is also assumed that the value of ε_F does not depend on the film thickness.

An assumption of the constancy of ε_F with growth of d is not precise: according to [24], the Fermi energy in 2D-degenerate gas of charge carriers oscillates with thickness. Depending on d and the number of filled levels N in the potential quantum well, on fulfillment of condition $E_N \le \varepsilon_F \le E_{N+1}$ the value ε_F is of the form [25]:

$$\varepsilon_F = \varepsilon_F^0 \cdot \frac{4}{3}\left[\frac{d}{\lambda_F N} + \frac{\lambda_F^2}{32}\frac{(N+1)(2N+1)}{d^2}\right], \tag{5}$$

where ε_F^0 is the value of Fermi energy in the bulk of the crystal, where dimensional quantization is inessential. Note that N is maximum number of a subband located below ε_F and depends on d and ε_F as $N = \frac{d\sqrt{8m_\perp^*\varepsilon_F(d)}}{h}$.

The result of calculation of $S(d)$ dependence with the use of Eqs.(3)-(5) is given in Fig. 4, *a* (solid blue curve). As the input parameters, the values of effective masses of charge carriers in *n-PbSe* and crystal electron concentration were used. As can be seen from Fig. 4, *a*, the value S oscillates with the period $\Delta d = (5 \pm 0.5)$ nm, which is close to experimental Δd. The insert in Fig. 4, *a* shows for comparison the experimental points and the theoretical curve. It is worthwhile to emphasize that account of all subbands located below ε_F, and of dependence $\varepsilon_F(d)$ in the calculation of the Seebeck coefficient yields a higher value of Δd, close to experimental, unlike the calculation that takes into consideration carriers that occupy only lower subband. Still, small number of experimental points in the area with $d < \sim 25$ nm prevents from speaking about full coincidence between calculation and experiment, though experimental results do not contradict theoretical calculation even in S value.

From Fig. 4, *a* it is evident that the amplitude of quantum oscillations S decays very fast with thickness, and at $d > \sim$ 25-30 nm one cannot describe dependence $S(d)$ in the approximation of dimensional quantization. Smooth growth of S and σ with thickness in the area of $d > 30$ nm can be related to manifestation of classical size effect. Taking into account high degree of electron gas degeneracy in the films, an attempt was made to describe the results in the framework of Fuchs-Sondheimer theory [26] and Mayer theory [27].

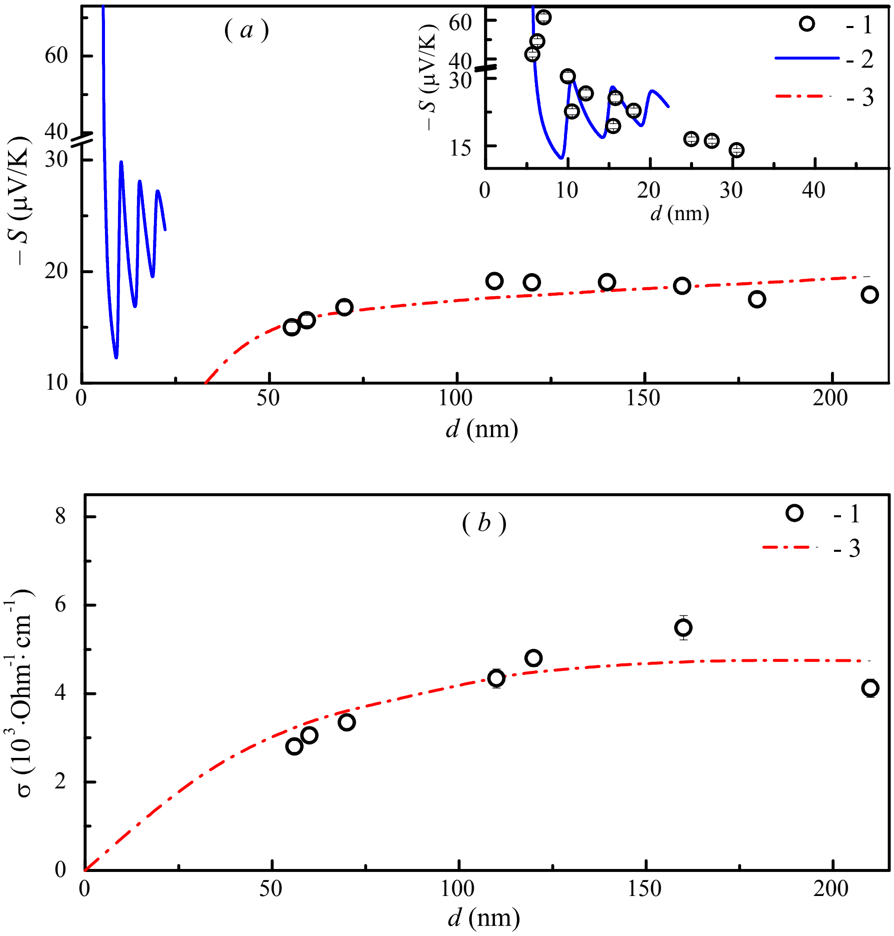

Fig. 4. Theoretical calculation of the dependence of the Seebeck coefficient S (a) and the electric conductivity σ (b) on the thickness of films: 1 – experimental data; 2 – calculation by formulae (3)-(5); 3 –calculation by formulae (6) and (7).

As a model, Fuchs-Sondheimer theory considers a metal with a spherical Fermi surface and isotropic carrier mean free path l independent of film thickness d. Specularity parameter p is introduced which determines the share of electrons elastically reflected from the surface, equal for both surfaces, independent of *d*, the trajectory and incidence angle of electrons on the surface. With fully diffused scattering $p = 0$, and with fully specular $p = 1$.

In the approximation of thin films ($d << l$) the expressions for σ and *S* (at $p \sim 0$) are of the form [26, 27]:

$$\sigma_d = \sigma_\infty \cdot \frac{3}{4} \cdot \frac{1+p}{1-p} \cdot \frac{d}{l} \ln\left(\frac{l}{d}\right), \tag{6}$$

$$S = S_\infty \left(1 + \frac{U}{1+U} \cdot \frac{\ln\left(d/l\right) - 1.42}{\ln\left(d/l\right) - 0.42} \right), \quad p \sim 0, \tag{7}$$

where σ_∞, S_∞ are the values of σ and *S* in a sample of infinitely large thickness, and parameter $U = \left(\partial \ln l / \partial \ln E\right)_{E=\varepsilon_F}$ characterizes the energy dependence of *l*. With a square dispersion law $U = 2$. As σ_∞ and S_∞, we took the values of kinetic coefficients of the crystal of which the films were prepared. Using formulae (6) and (7), the theoretical dependences *S*(*d*) and *σ*(*d*) were constructed (Fig. 4, curve 3) and the values *p* and *l* were determined whereby the best agreement is observed between the experimental data and the theoretical curve, determined by the lowest value of mean-square deviation. It turned out that dependence σ(*d*) is best described at $p = 0.58 \pm 0.02$ and $l = (490 \pm 40)$ nm, and dependence *S*(*d*) – at $l = (380 \pm 40)$ nm. Note that for films of undoped *PbSe* the calculation of dependence σ(*d*) by formula (6) yielded the following values of *p* and *l*: $p = 0.57 \pm 0.02$ and $l = (800 \pm 40)$ nm [17]. It can be seen that the calculated values of *l* in *PbSe<PbCl₂>* films proved to be considerably lower than for the undoped *PbSe* films which is naturally attributable to the presence of considerable amount of chlorine impurity in the films under study.

Conclusions

The method of thermal evaporation in vacuum of *PbSe* crystals doped with $PbCl_2$ on (001) *KCl* substrates was used to grow thin films of thicknesses $d = 5$-220 nm, having *n*-type conductivity.

By the methods of electron probe microanalysis and atomic force microscopy it was established that high degree of homogeneity is observed in the films, the surface is mostly smooth, gain structure is not manifested.

The oscillating character of dependences of the Seebeck coefficient *S*, electric conductivity σ and the Hall coefficient R_H on film thickness *d* was established in the range of $d \approx 5 \div 30$ nm, which is related to manifestation of QSE. The experimental data are in agreement with the theoretical calculation of dependence *S*(*d*) on the assumption of dimensional quantization with regard to contribution of several energy subbands and dependence of the Fermi energy on *d* both in the value of oscillation period and the values of *S*. The possibility of observation of electron spectrum quantization in *n-PbSe* with high degree of charge carrier degeneracy at room temperature was shown.

Increase in *S* and σ with film thickness in the area $d > 30$ nm was discovered, which is attributed to manifestation of ClSE. Interpretation of *S*(*d*) and σ(*d*) dependences was given in the framework of Fuchs-Sondheimer and Mayer theories.

The work was performed with support from the State Foundation for Basic Research (Ukraine) (Grant #UU 42/006-2011) and US Civilian Research and Development Foundation (Grant # UKP-7074-KK-12).

References

1. J.M.Martin, J.L.Hernandez, L.Adell, A.Rodriguez, and F.Lopez, Arrays of Thermally Evaporated PbSe Infrared Photodetectors Deposited on Si Substrates Operating at Room Temperature, *Semicond. Sci. Technol*. **11**, 1740-1744 (1996).
2. H.Preier, Recent Advances in Lead-Chalcogenide Diode Lasers, *Appl. Phys*. **20**, 189-206 (1979).
3. J.J.Choi, Y.F.Lim, M.B.Santiago-Berrios, M.Oh, B.R.Hyun, L.F.Sun, A.C.Bartnik, A.Goedhart, G.G.Malliaras, H.D.Abruna, F.W.Wise, T.Hanrath, PbSe Nanocrystal Excitonic Solar Cells, *Nano Lett*. **9**, 3749-3755 (2009).
4. L.I.Anatychuk, *Thermoelements and Thermoelectric Devices*. Reference book (Kyiv: Naukova dumka, 1979), 768 p. (In Russian).
5. D.M.Rowe, *CRC Handbook of Thermoelectrics* (CRC Press, Boka Raton, London, New York, Washington, 1995), 701 p.
6. Yu.I.Ravich, B.A.Efimova, and I.A.Smirnov, *Methods of Research on Semiconductors as Applied to Lead Chalcogenides PbTe, PbSe and PbS (*Moscow: Nauka, 1968), 384 p.
7. T.C.Harman, D.L.Spears, M.J.J.Manfra, High Thermoelectric Figures of Merit in PbTe Quantum Wells, *J. Electron. Mater*. **25**, 1121-1127 (1996).
8. T.C.Harman, D.L.Spears, and M.P.Walsh, PbTe/Te Superlattice Structures with Enhanced Thermoelectric Figures of Merit, *J. El. Mater*. **28**, L1-L5 (1999).
9. Yu.F.Komnik, *Physics of Metal Films* (Moscow: Atomizdat, 1979), 264 p.
10. E.I.Rogacheva, T.V.Tavrina, O.N.Nashchekina, S.N.Grigorov, K.A.Nasedkin, M.S.Dresselhaus, and S.B.Cronin, Quantum Size Effects in PbSe Quantum Wells, *Appl. Phys. Lett*. **80**, 2690-2693 (2002).
11. E.I.Rogacheva, O.N.Nashchekina, Y.O.Vekhov, M.S.Dresselhaus, and S.B.Cronin, Effect of Thickness on the Thermoelectric Properties of PbS Thin Films, *Thin Solid Films* **423**, 115-118 (2002).
12. E.I.Rogacheva, O.N.Nashchekina, T.V.Tavrina, M.Us, M.S.Dresselhaus, S.B.Cronin, and O.Rabin, Quantum Size Effects in IV-VI Quantum Wells, *Physica E* **17**, 313-315 (2003).
13. S.I.Olkhovskaya, E.I.Rogacheva, Size Effects in Lead Telluride Thin Films and Thermoelectric Properties, *J.Thermoelectricity* **5**, 22-27 (2013).
14. Rogacheva E.I., Vodorez O.S., Nashchekina O.N., Sipatov A.Yu., Fedorov A.G., Olkhovskaya S.I., Dresselhaus M.S., Oscillatory Behavior of Thermoelectric Properties in p-PbTe Quantum Wells, J. Electronic Materials, 39(9), 2010, p. 2085-2091.
15. Rogacheva E.I., Lyubchenko S.G., Volobuev V.V., Sipatov A.Yu., Quantum size effects in PbTe/mica films, Proc. IV European Conference on Thermoelectrics, Wales (UK), 2006, p. 1-4.
16. Rogacheva E.I., Ol’khovskaya S.I., Sipatov A.Yu., Fedorov A.G., Size effect in lead selenide thin films, Bulletin of Kharkov National University, Ser. Physics, 914 (13), 2010, P. 115-118.
17. Rogacheva E.I., Nashchekina O.N., Olkhovskaya S.I., and Dresselhaus M.S., Size Effects in PbSe Thin Films, J. Thermoelectricity, 4, 2012, p. 25-32.
18. S.I.Ol'khovskaya, E.I.Rogacheva, A.Yu.Sipatov, Thickness Dependences of PbSe<Cl> Films Thermoelectric Properties, *Metallofizika i Noveishie Tekhnologii* **33**, 213-220 (2011).
19. P.Pongratz, H.Sitter, TEM Analysis of Lead Telluride Films Grown by Hot-Wall Epitaxy on KCl and BaF_2, *J. Cryst. Growth* **80**, 73-78 (1987).

20. G.Springholz, *Molecular Beam Epitaxy of IV-VI Semiconductors: Multilayers, Quantum Dots and Device Applications*, Chapter 13, 2013, p. 263-310.
21. M.S.Dresselhaus, G.Dresselhaus, X.Sun, Z.Zhang, B.Cronin, and T.Coga, Low-Dimensional Thermoelectric Materials, *Physics of the Solid State* **41**(5), 679-682 (1999).
22. E.I.Rogacheva, M.S.Dresselhaus, Quantum Size Effects and Thermoelectric Transport in IVVI-Based 2D-Structures, *Proc. ECT (Odessa, Ukraine, 2007)*, p. 29-34.
23. M.P.Singh, C.M.Bhandari, Non-Monotonic Thermoelectric Behavior of Lead Telluride in Quantum-Well-Like Structures, *Solid State Communications* **133** (1), 29-34 (2005).
24. F.K.Schulte, A Theory of Thin Metal Films: Electron Density, Potentials and Work Function, *Surface Science* **55**, 427-444 (1976).
25. V.D. Dymnikov, Fermi Energy of Electrons in a Thin Metallic Plate, *Physics of the Solid State* **53** (5), 901-907 (2011).
26. E.H.Sondheimer, The Mean Free Path of Electrons in Metals, *Adv.Phys*. **1**(1), 1-42 (1952).
27. H.Mayer, *Physik dunner Schichten, V. 2* (Wissenschaftliche Verlag, Stuttgart, 1955).

Submitted 07.04.2015

L.I. Anatychuk

L.I. Anatychuk, V.M. Polyak

Institute of Thermoelectricity
of the NAS and MES of Ukraine,
1, Nauky Str., Chernivtsi, 58029, Ukraine

V.M. Polyak

COMPUTER DESIGN OF THERMOELECTRIC OTEC

Method for computer design of thermoelectric OTEC (Ocean thermal energy conversion) plants is developed which allows optimization of electric power plant in many parameters and take into account the losses in OTEC operation. The efficiency of the method is demonstrated by an example of a concrete physical model of OTEC. Optimal parameters of TEG are defined, whereby its maximum generated power is achieved with regard to losses for in-house needs. Economic parameters of a 100 kW thermoelectric OTEC are calculated: relative capital investments are 25 $/W, the cost of electric energy is 0.15 – 0.3 $/kW·h, which confirms the economic viability of such projects.

Key words: thermoelectric generator, Ocean thermal energy, Ocean power station

Introduction

General characterization of the problem. The relevance of creating efficient renewable energy sources is generally known. Among them, increasing interest is aroused by the sources using low-grade heat due to its huge amount, for instance industrial waste heat, the exhaust heat from thermal electric power plants, etc. However, the major of these low-grade heat sources is global ocean where the difference in temperatures between its surface and the depth of 1-2 km reaches 20-25°. Creation of ocean thermal into electric energy converters (OTEC) can have a significant impact on solving the problem of power supply to mankind. In fact, these are solar energy converters, but OTEC can work day and night, offering a number of principal advantages. Such attractive opportunities stimulate development of electric power pants working on this heat.

For realization of this opportunity, developments of OTEC with the use of heat engines are underway [1]. Their efficiency can reach 3%. This relatively low efficiency cannot become the basic obstacle on the way to using OTEC, since the advisability of their creation primarily depends on its economic factors, rather than efficiency. In [2,3] it was established that OTEC based on heat engines can be competitive to solar electric power plants at powers higher than 10 MW. At lower powers, relative capital investments increase. Therefore, low-power OTEC are economically unviable. Creation of high-power OTEC is also problematic because of considerable investments with insufficiently defined risks.

Thermoelectric OTEC are free from this disadvantage, since they are almost insensitive to scale factor, which accounts for intense interest in them.

In 1980-1982, in Japan, company Kawasaki Heavy Industries was the first to manufacture a thermoelectric generator (TEG) for OTEC [4]. It experimentally confirmed the possibility of electric energy production at low temperature differences. The generator employed conventional cooling modules. No optimization results for modules and TEG were reported.

Ref. [5] describes the results of theoretical and experimental investigations of TEG design for low temperature differences, including ocean temperature difference. Optimization was performed with a view to achieve maximum efficiency. Calculations were made without regard to loses on pumping of cold water from the bottom of the ocean and hot water from the ocean surface to TEG.

Ref. [1, 6, 7] give the results of optimization of thermoelectric OTEC for the achievement of maximum power. Calculations of relative capital investments for 400 MW OTEC are made. It is established that they are close to capital investments in OTEC with a heat engine. The latter is a convincing proof of the advisability of using thermoelectric generators in OTEC at low powers. In so doing, the losses of electric energy on pumping of cold water from the bottom of the ocean are taken into account, and the losses due to warm water pumping from the ocean surface are disregarded.

A 100 kW thermoelectric OTEC is calculated in [8]. The cost of electric energy 0.15 $/kW·h is obtained, which proves the viability of using low-power thermoelectric OTEC.

However, designing of such OTEC is rather cumbersome due to the necessity of optimization of many structural components. The above results were obtained by direct mathematical calculations that become increasingly productive with increasing number of variables for OTEC optimization. Therefore, for further progress in this area it is important to pass to computer simulation of thermoelectric OTEC. Below are given the main approaches of this simulation and the results of computer design for a concrete physical model of OTEC.

1. Physical model of thermoelectric OTEC

A general model of thermoelectric OTEC of power W_{OTEC} is given in Fig. 1, *a*. It consists of a thermoelectric generator (TEG) 1 and heat pipes for the hot 2, mixed 3 and cold water 4, with their lengths L_1, L_2 and L_3, and lowering heights H_1, H_2 and H_3, respectively. The outer surface of the cold water pipeline is thermally insulated. Water in the pipes is pumped by two pumps: 5 – of power W_{hp} for the hot water, 6 – of power W_{cp} for the cold water. The model of TEG is shown in Fig. 1, *b*. It comprises rows of thermoelectric modules 7, arranged between the hot 8 and cold 9 heat exchangers in the form of pipes of rectangular shape from the outside. Water flowing in adjacent heat exchangers has equal temperature. The hot and cold water is fed to heat exchangers through inlet collectors 10 and 11 and flows out of heat exchangers through collectors 12 and 13.

The model of TEG can be conveniently described by identical block-sections 14. They are composed of one module located between the hot and cold heat exchangers. Each TEG row comprises *N* block-sections. The TEG consists of *n* rows.

Fig. 1, *c* shows a model of TEG block-section. Here, a thermoelectric module consists of n- and p-type legs 15 of height *h,* length *a* and width *b*, connecting plates 16 and electrically isolating ceramic plates 17. The internal shape of heat exchangers is determined by effective diameter *d.* The module generates power Wm_i which is equal to the difference between thermal power that came to the module from the hot heat carrier Qh_i and thermal power given to the cold heat carrier Qc_i.

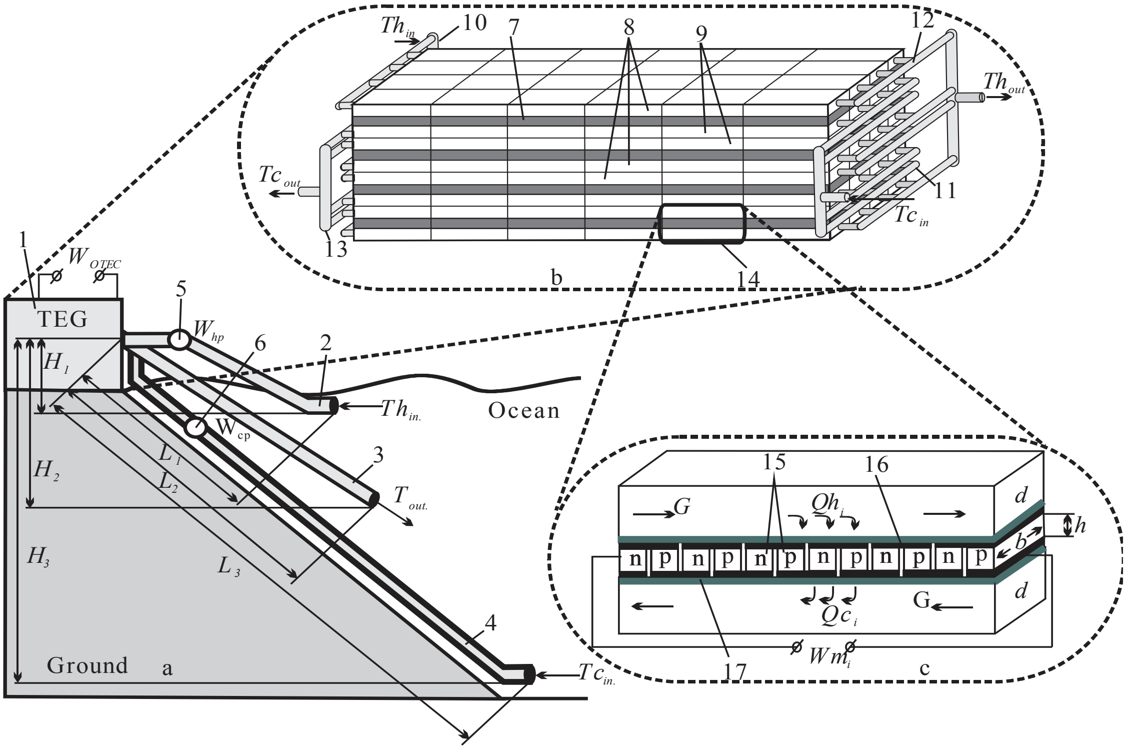

Fig. 1. Physical model of thermoelectric OTEC: A – thermoelectric OTEC; B - TEG; C – block-section of TEG.

The power of TEG is affected by the following parameters:

- pipeline lengths L_1, L_2 and L_3;
- pipeline lowering heights H_1, H_2 *and* H_3;
- pipeline diameter D;
- inlet hot water temperature Th_{in};
- inlet cold water temperature Tc_{in};
- number of TEG rows n;
- number of block-sections in a row N;
- block-section length l;
- local resistance coefficients ξ at pipe inlets and outlets and on collectors;
- pumps efficiency η;
- heat carrier flow rate in one row G;
- heat exchanger channel diameter d;
- thickness of heat exchanger wall x;
- height of thermoelectric module legs h;
- width of thermoelectric module legs b;
- length of thermoelectric module legs a;
- distance between the legs l_1;
- connecting plates thickness h_1;
- ceramic plate thickness h_2.

Parameters to be optimized in this model include G, d, h, b, N. All other parameters during optimization are assigned as input data. Having optimal parameter values, one can determine the number of TEG rows n which are necessary for construction of electric power plant of assigned power.

2. Mathematical description of the model

To describe heat and electricity fluxes, we use the laws of conservation of energy

$$\operatorname{div}\vec{E}=0 \tag{1}$$

and electrical charge

$$\operatorname{div}\vec{j}=0, \tag{2}$$

where

$$\vec{E}=\vec{q}+U\vec{j}, \tag{3}$$

$$\vec{q}=\kappa\nabla T+\alpha T\vec{j}, \tag{4}$$

$$\vec{j}=-\sigma\nabla U-\sigma\alpha\nabla T, \tag{5}$$

where $\vec{E}$ is energy flux density, $\vec{q}$ is heat flux density, $\vec{j}$ is electric current density, U is electrical potential, T is temperature, α, σ, κ are the Seebeck coefficient, electrical conductivity and thermal conductivity.

Taking into consideration (3) - (5), one can get

$$\vec{E}=-(\kappa+\alpha^2\sigma T+\alpha U\sigma)\nabla T-(\alpha\sigma T+U\sigma)\nabla U. \tag{6}$$

Then the laws of conservation (1), (2) will take on the form:

$$-\nabla\left[(\kappa+\alpha^2\sigma T+\alpha U\sigma)\nabla T\right]-\nabla\left[(\alpha\sigma T+U\sigma)\nabla U\right]=0, \tag{7}$$

$$-\nabla(\sigma\alpha\nabla T)-\nabla(\sigma\nabla U)=0. \tag{8}$$

These nonlinear second-order differential equations in partial derivatives (7) and (8) are determined by the distributions of temperature T and potential U in thermoelements.

Equation describing the process of heat transfer in heat exchanger walls in the steady-case case is written as follows

$$\nabla(-k_1\cdot\nabla T_1)=Q_1 \tag{9}$$

where k_1 is thermal conductivity coefficient of heat exchanger walls, ∇T_1 is temperature gradient, Q_1 is heat flux.

The processes of heat and mass exchange of heat carriers in heat exchanger channels in the steady-case are written by equations [9]

$$-\Delta p-f_D\frac{\rho}{2d_h}v|\vec{v}|+\vec{F}=0, \tag{10}$$

$$\nabla(A\rho\vec{v})=0, \tag{11}$$

$$\rho\mathrm{AC_p}\vec{v}\cdot\nabla T_2=\nabla\cdot Ak_2\nabla T_2+f_D\frac{\rho A}{d_h}|\vec{v}|^3+Q_2+Q_{wall}, \tag{12}$$

where p is pressure, ρ is heat carrier density, A is cross-section of the pipe, $\vec{F}$ is the sum of all forces, C_p is heat carrier heat capacity, T_2 is temperature, $\vec{v}$ is velocity vector, k_2 is heat carrier thermal conductivity, f_D is the Darcy coefficient, $d=\frac{4A}{Z}$ is effective diameter, Z is pipe wall perimeter, Q_2 is heat released due to viscous friction [W/m] (from heat exchanger unit length), Q_{wall} is heat flux coming from heat carrier to pipe walls [W/m].

$$Q_{wall}=h\cdot Z\cdot(T_1-T_2), \tag{13}$$

where h is heat exchange coefficient found from equation

$$h = \frac{Nu \cdot k_2}{d}. \tag{14}$$

The Nusselt number is found with the use of the Gnielinski equation (3000 $<Re<$ $6 \cdot 10^6$, 0.5 $<$Pr$<$ 2000)

$$Nu = \frac{\left(\frac{f_d}{8}\right)(Re - 1000)Pr}{1 + 12.7\left(\frac{f_d}{8}\right)^{\frac{1}{2}}\left(Pr^{\frac{2}{3}} - 1\right)}, \tag{15}$$

where the Prandtl number $Pr = \frac{C_p \mu}{k_2}$, μ is dynamic viscosity, $Re = \frac{\rho v d}{\mu}$ is the Reynolds number.

To determine the Darcy coefficient f_D, we use the Churchill equation for the entire spectrum of the Reynolds numbers and all values e / d (e is wall surface roughness)

$$f_D = 8\left[\frac{8}{Re}^{12} + (A + B)^{-1.5}\right]^{1/12}, \tag{16}$$

where $A = \left[-2.457 \cdot \ln\left(\left(\frac{7}{Re}\right)^{0.9} + 0.27(e / d)\right)\right]^{16}$, $B = \left(\frac{37530}{Re}\right)^{16}$.

Solving equations (7)-(12), we obtain the distribution of temperatures, electrical potential (for thermoelements), velocities and pressure (for heat carrier).

The objective function during optimization of the block-section is the net power (module power with regard to losses for pumping of heat carriers in heat exchangers) which is calculated by the formula:

$$W_i = Wm_i - Wn_{hot} - Wn_{cold}, \tag{17}$$

where

$$Wm_i = \left(\frac{\Delta U}{R + r}\right)^2 R, \tag{18}$$

$$Wn_{hot} = \frac{G \cdot \Delta p_h}{\eta}, \tag{19}$$

$$Wn_{cold} = \frac{G \cdot \Delta p_c}{\eta}. \tag{20}$$

Here Wn_{hot}, Wn_{cold} are powers spent on pumping of the hot and cold heat carriers, respectively, ΔU is potential difference between extreme interconnects of block-sections, R is electrical load resistance, r is thermoelement resistance, Δp_h, Δp_c is hydraulic resistance of the hot and cold heat exchangers (pressure drop), η is pump efficiency.

Module efficiency can be calculated by the formula

$$\eta_m = \frac{Wm_i}{Qe_i}. \tag{21}$$

The power of all modules in a row and the net power of one TEG row are determined by the formulae

$$Wm = \sum_{i=1}^{N} Wm_i, \tag{22}$$

$$W = \sum_{i=1}^{N} W_i \,. \tag{23}$$

After optimization of block-section geometrical dimensions, determination of power and efficiency of optimal block-section, one can find the number of TEG rows *n* which is necessary for building of electric power plant of power W_{OTEC}. For this purpose, we use the equation

$$W_{OTEC} = n \cdot N \cdot Wm_i - W_{hp}(n) - W_{cp}(n)\,. \tag{24}$$

The efficiency of electric power plant is found by the formula

$$\eta_{OTEC} = \frac{W_{OTEC}}{n \cdot N \cdot Qh_i}\,. \tag{25}$$

The power consumed by the pumps can be determined by the formulae

$$W_{hp}(n) = W_h(n) + \frac{1}{2} W_{exit}(n) + n \cdot N \cdot Wn_{hot}\,, \tag{26}$$

$$W_{cp}(n) = W_c(n) + \frac{1}{2} W_{exit}(n) + n \cdot N \cdot Wn_{cold}\,. \tag{27}$$

Power that must be spent on pumping of water by pipelines in the general case is calculated by the formula [10]:

$$W_{c,h,exit}(n) = \frac{1}{\eta}\left[(\rho_1 - \rho_2) G_v(n) g H + \left(\lambda \frac{L}{D} + \xi\right) \cdot \frac{\rho G_v^{\,3}(n)}{2S^2}\right], \tag{28}$$

where G_v is water consumption in all TEG rows (for mixed water it is twice as large), ρ is the average water density, ρ_1, ρ_2 are the densities of cold and hot water, respectively, *g* is free fall acceleration, H is the required height of water lift, $\lambda = \frac{0.316}{\sqrt[4]{\mathrm{Re}}}$ is pipe friction number, *D* is pipe diameter, *L* is pipe length, ξ is local resistance coefficient (takes into account local resistances at pipe inlets and outlets and on collectors 10 - 13), *S* is pipe cross-sectional area, $\mathrm{Re} = \frac{4\rho G_v}{\mu \pi D}$ is the Reynolds number.

3. Computer model of TEG block-section

Design of thermoelectric power plant is composed of two phases:

1) optimization of one row of TEG block-sections;
2) calculation of thermoelectric power plant.

For solving of the first phase of the problem it is reasonable to use finite-element method that can be realized in Comsol Multiphysics program environment. This method allows solving differential equations (6)-(12) for different values of TEG parameters (*G, d, h, b, N*). Of these parameters one can select such whereby the function of TEG input power (17) will reach maximum.

Let us consider construction of a computer model of TEG block-section by example of a TEG with heat exchangers of round shape from inside. This shape of heat exchangers is due to the fact that their hydraulic resistance is 15% lower than that of rectangular heat exchangers. This is determined by means of computer simulation in Comsol of two pipes of identical length and cross section. The results are given in Fig. 2.

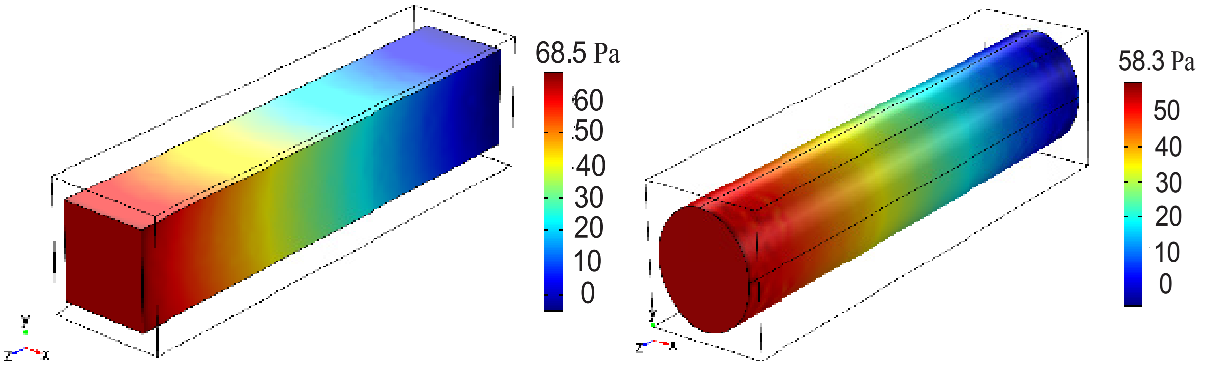

a *b*

Fig. 2. Pressure difference in a pipe of rectangular A and round B shape from inside.

Fig. 3 shows finite element geometry and mesh built in Comsol for simulation of thermoelectric block-section. The input data are as follows:

- block-section length $l = 60$ mm;
- pump efficiency $\eta = 80$ %;
- heat exchanger wall thickness $x = 2$ mm;
- length of thermoelectric module legs $a = 4$ mm;
- distance between the legs $l_1 = 1$ mm;
- thickness of connecting plates $h_1 = 0.5$ mm;
- thickness of ceramic plates $h_2 = 0.5$ mm.

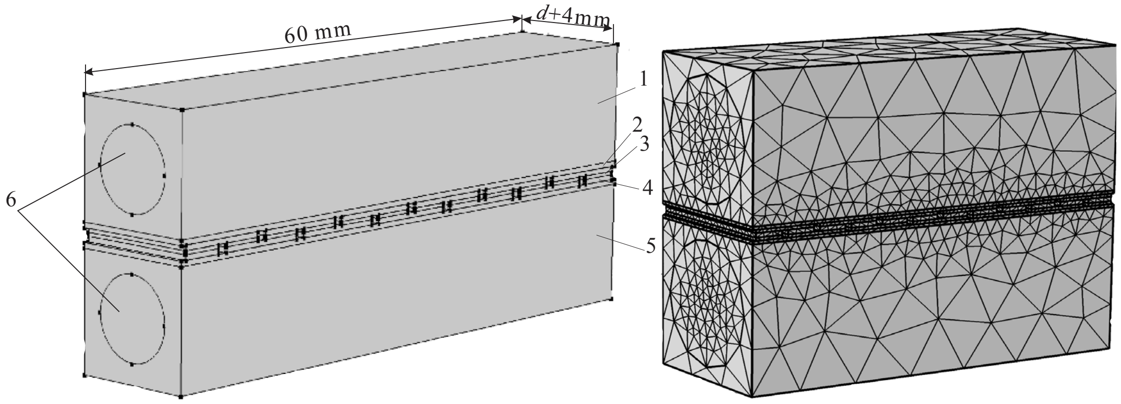

a *b*

Fig.3. Geometry A and mesh B built in Comsol for TEG block-section:
1 – hot heat exchanger; 2 – ceramic plate; 3 –thermoelectric material; 4 – connecting plate; 5 – cold heat exchanger; 6 – channels of diameter d with a heat carrier.

Material of heat exchangers is aluminum. Material of connections is copper. The model takes into account contact and connecting resistance of thermoelements. Contact resistance is equal to 10^{-5} Ohm·cm^2. To take into account the temperature dependence of α, σ, κ of *n*-type and *p*-type thermoelectric material *Bi-Te*, they were assigned as polynomials obtained from the experimental data. The net power was calculated in the mode of matched load ($R = r$).

Simulation parameters variation range:

- channel diameter $d = 2..140$ mm;
- leg height $h = 0.04..10$ mm;
- leg width $b = 12…200$ mm;

- heat carriers flow rate *G* = 1..2000 ml/s;
- the number of block-sections *N* = 1..400 pcs.Net simulation conditions:
- Hot water inlet temperature *Th* = 29 °C.
- Cold water inlet temperature *Tc* = 4 °C.
- Heat carrier flow rate at channel inlets *G*.
- Pressure at channel outlets *p* = 0 Pa.
- Electrical potential on the first interconnect *U* = 0 V.
- The rest of the boundaries are imposed with thermal and electrical insulation conditions.

4. Computer simulation results

Fig. 4 shows typical distributions of temperature and electrical potential in the block-section.

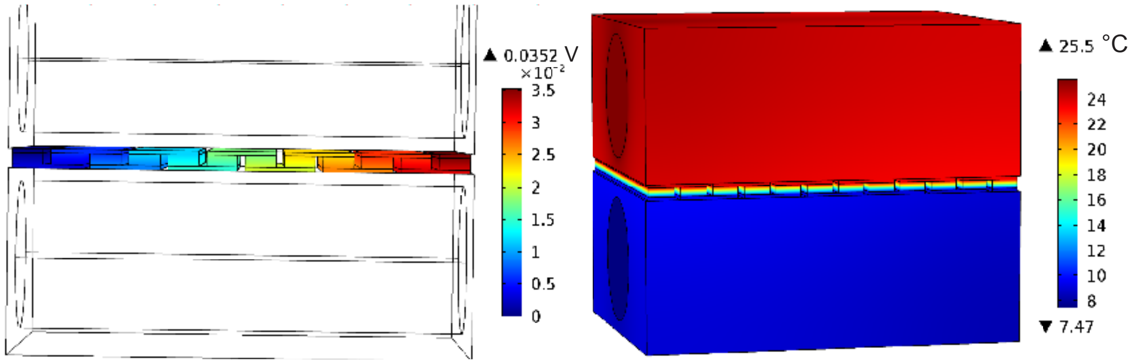

a) *b)*

Fig.4. Typical distribution of temperatures a) and electrical potential b) in the block-section.

Figs. 5, 6 show a series of dependences of net power (17) on legs height *h* for optimal *d*, heat carrier flow rate *G* for optimal *h* and channel diameter *d* for optimal *h* (*b* = 12 mm).

Fig. 7 presents the results of optimization for the number of block-sections in one row.

The following optima are seen from the plots:

- leg height $h_{opt}^* = 0.35$ mm;
- heat carrier flow rate $G_{opt} = 300$ ml/s;
- channel diameter $d_{opt} = 20$ mm;
- number of block-sections in one row *N* = 175 pcs.

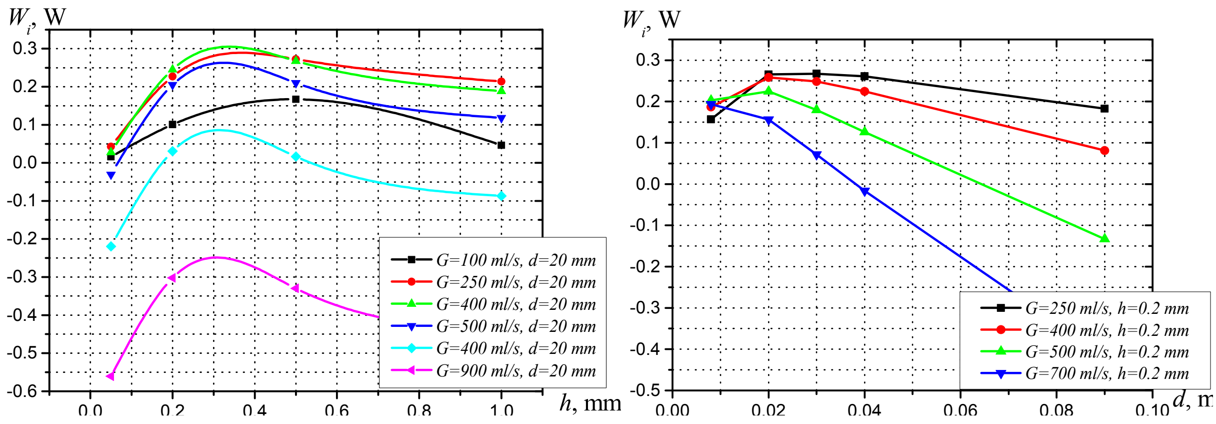

a) *b)*

Fig.5. a) Dependence of net power (17) on legs height h for optimal d, b) Dependence of net power on heat carrier flow rate G for optimal h.

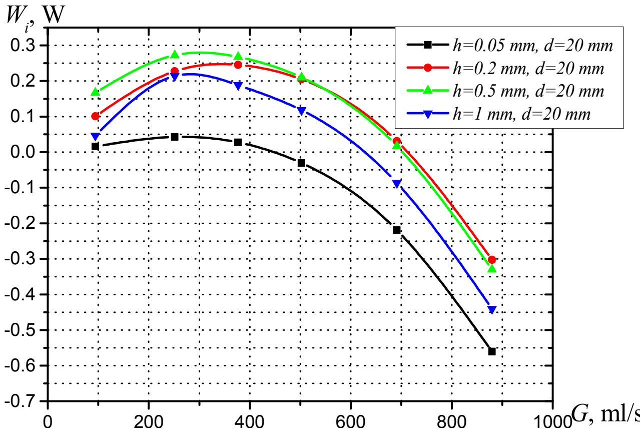

Fig. 6. Dependence of net power on channel diameter d for optimal h.

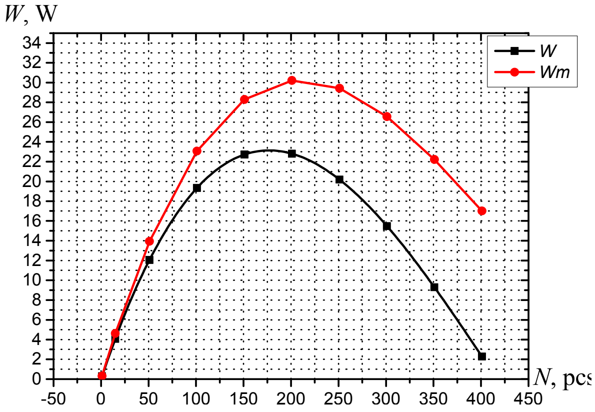

Fig. 7. Dependence of all modules power (22) and net power (23) on the number of block-sections in one row.

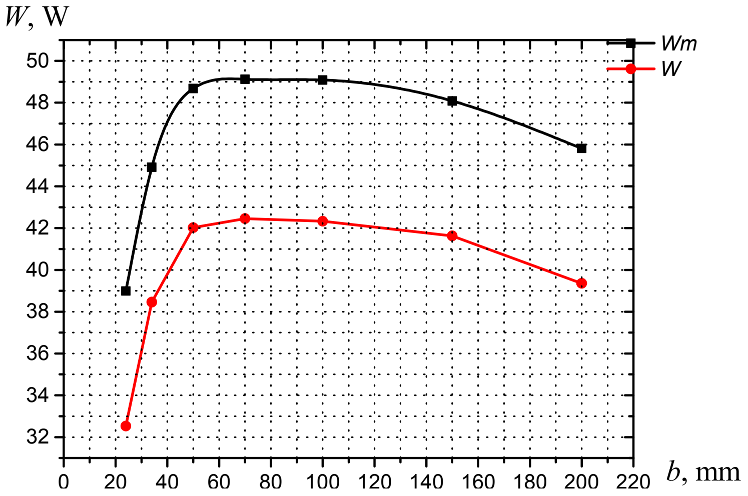

Fig.8. Dependence of all modules power (22) and initial power (23) on leg width.

These results were obtained for a thermoelement with leg width b = 12 mm. In order to increase power due to increased area of contact between heat exchanger and module and reduced effect of contact resistance, one should increase the width and height of leg proportionally in such a way that thermoelectric material completely filled the space between heat exchangers. With further increase of leg width, one should accordingly increase the width of heat exchanger. Simulation showed that optimum is achieved with leg width b_{opt} = 50 mm and the respective height h_{opt} = 1.5 mm (Fig.8).

As a result of calculation of a model with final optimal parameters h_{opt} = 1.5 mm, b_{opt} = 50 mm, G_{opt}=300 ml/s, d_{opt} = 20 mm, N = 175 pcs, the following energy characteristics of one row of block-sections were obtained:

- net power W_{max} = 42 W;
- modules power Wm_{max} = 49 W;
- voltage U_N = 2.8 V;
- current I = 17.5 A;
- generator efficiency η_{TEG} = 0.76 %;
- modules efficiency η_{m} = 0.88 %.

5. Calculation of thermoelectric power plant

The second phase of electric power plant design consists of calculation of power losses on pumping of water pipelines and calculation of the number of TEG rows that are necessary to achieve the required power of electric power plant W_{OTEC}. For this purpose, one should solve Eq. (24) which can be easily done in Mathcad program.

Consider, as an example, an electric power plant of power W_{OTEC} = 100 kW. One row of modules with regard to power losses on heat carrier pumping generates 42 W of electric energy with water flow rate 2×300 ml/s. It is necessary to use n rows of TEG. Each pump must provide for flow rate $Gv = n \cdot 300 \cdot 10^{-6}$ m^3/s.

Input data for calculations:

- pipeline lengths $L_1 = 2000$ m, $L_2 = 200$ m, $L_3 = 20$ m;
- pipeline lowering heights $H_1 = 1000$ m, $H_2 = 100$ m, $H_3 = 10$ m;
- local resistance coefficients at pipe inlets $\xi_{in} = 0.5$, pipe outlets $\xi_{out} = 1$, on the bends $\xi_b = 0.7$, on inlet collectors $\xi_{\text{c.in}} = 1.2$, on outlet collectors $\xi_{\text{c.out}} = 0.8$;
- pipeline diameter $D = 2\ldots10$ m.

Fig. 9 shows the results of calculation of the number of rows and power losses on water pumping in the pipelines for electric power plant of power W_{OTEC} = 100 kW. From the plot it is apparent that for diameters smaller than $D = 3$ m, power losses on water pumping and the number TEG rows increase considerably. The use of pipelines with large diameters is complicated due to increase of mechanical loads on the pipe and its cost.

Making calculations for D = 3 m we obtain the necessary number of module rows $n = 3313$; powers that should be spent pumping $W_c = 36.31$ kW, $W_h = 1$ kW and $W_{exit} = 1.94$ kW; power that generated by thermoelectric modules– 162.3 kW; power spent on pumping of heat carriers in TEG channels – 23.1 kW; electric power plant efficiency – 0.54%.

It is readily calculated that with the cost of thermoelectric module 3$ (under mass production conditions), the cost of heat exchanger material 2.5 $/kg, the cost of pipelines 60 $/m, pipes 0.45 $/W, inverter 0.1 $/W and other expenses 10%, the relative capital investments to such plant will be up to 25 $/W. For comparison, the same relative capitals investments are made in heat engines of power 6 MW [2]. The cost of electric energy in so doing is 0.15 – 0.3 $/kW·h. Thus, thermoelectric OTEC offer advantage over heat engines in the range of low powers, since they are less sensitive to scale factor.

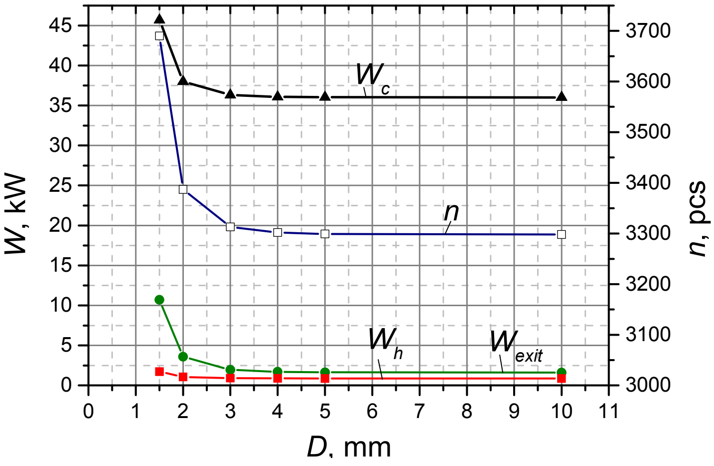

Fig. 9. Dependence of the number of TEG rows and power losses on water pumping on pipeline diameter.

Moreover, the specific cost of solar power plants with all their structural components varies from 3\$/W to 6 \$/W [11]. Considering that capacity use factor within 24 hours in solar electric power plants is 20% [12], and in OTEC – 100%, one can speak about the competitive ability of these technologies.

Conclusions

1. Design method for thermoelectric OTEC has been developed.
2. Optimal parameters have been determined for a row of TEG block-sections, whereby maximum generated power $W_{\max} = 42$ W is achieved with regard to losses for in-house needs: leg height $h_{opt} = 1.5$ mm, leg width $b_{opt} = 50$ mm, heat carrier flow rate $G_{opt} = 300$ ml/s, heat exchanger channel diameter $d_{opt} = 20$ mm, number of block-sections in one TEG row $N = 175$ pcs.
3. A 100 kW electric power plant has been calculated, the relative capital investments in the plant have been determined as 25 \$/W, and the cost of electric energy as 0.15 – 0.3 \$/kW·hour.

References

1. D.K. Benson, T.S. Jayadev, Thermoelectric Energy Conversion, *Proc.3-rd Int. Conf. Thermoel. Convers*. (Arlington, Tex.,1980, N.Y.,1980), P.27-56.
2. Luis A. Vega, Ph.D, Economics of Ocean Thermal Energy Conversion (OTEC): An Update, *2010 Offshore Technology Conference* (Houston, Texas, USA, 3–6 May 2010).
3. Yu.M.Lobunets, Thermoelectricity and Ocean, *J.Thermoelectricity* **3**, 82 – 86(2014).
4. Kin-Ichi Uemura, History of Thermoelectricity Development in Japan, *J.Thermoelectricity* (2002).
5. K Matsuura, D.M.Rowe, K.Koumoto, G.Min, and A. Tsuyoshi, Design Optimization for a Large Scale, Low Temperature Thermoelecric Generator, *Proc. of the 11 Int. Conf. on Thermoel*. (1992, USA, Texas, Arlington), P.10-16.
6. Bohn, Benson, Jayadev, Thermoelectric OTEC, *Journal of Solar Energy Engineering* 102, 119-127(1980).
7. J. Henderson, Analysis of a Heat Exchanger - Thermoelectric Generator System, *14th Intersociety Energy Conversion Engineering Conference* (Boston, 1979).
8. Yu.M.Lobunets, Performance Evaluation of OTEC with Thermoelectric Power Converter, *J.Thermoelectricity* **1,** 62 – 67 (2013).
9. Michael V. Lurie, *Modeling of Oil Product and Gas Pipeline Transportation* (WILEY-VCH Verlag Gmbh & Co. Kgaa, Weinheim, 2008), p. 214
10. Ya.M.Vilner, *Reference Manual on Hydraulics, Hydraulic Machines and Hydraulic Drives* (Moscow: Vyschaya Shkola, 1976), 411 p.
11. International Renewable Energy Agency. Renewable energy technologies: cost analysis series. 2012 p., 46 c.
12. Economics of Renewable Energy Plants/ http://www.greenrhinoenergy.com/renewable/context/economics.php

Submitted 16.04.2015.

V.Ya. Mykhailovsky, L.M. Vykhor, M.V. Maksimuk, R.M. Mochernyuk

Institute of Thermoelectricity of the NAS and MES of Ukraine,
1, Nauky Str., Chernivtsi, 58029, Ukraine

DESIGN OF THERMOELECTRIC STAGED MODULES WITH SEGMENTED LEGS BASED ON *Bi_2Te_3-PbTe-TAGS*

The results of computer design of generator staged modules based on Bi_2Te_3-PbTe-TAGS with segmented legs for improved efficiency of thermoelectric power conversion are presented. A three-dimensional model was used to find the optimal parameters of leg segment materials for each stage and the inter-stage temperature whereby the efficiency of staged module achieves maximum value. Comparative energy characteristics of such modules in the operating temperature range 30 – 500 °C are given. Design was performed with regard to the temperature dependences of material parameters, the thermal and electrical losses on segment contacts and stage connections.

Key words: computer design, three-dimensional model, staged generator modules, segmented legs, efficiency, thermoelement.

Introduction

At present, traditional methods for improvement of thermoelectric power conversion efficiency are mainly limited to creation of materials with high values of figure of merit *ZT* [1, 2]. However, despite numerous investigations, no real improvement of the figure of merit has been achieved in recent 40 years [3, 4]. For crystalline thermoelectric materials currently used in industry (materials based on *Bi-Te*, *Pb-Te*, *Ag-Sb-Ge-Si*), the values of *ZT* 1.0-1.6 were achieved as far back as the mid of the previous century [5]. Whereas nanostructured materials, though possessing higher *ZT* values as compared to crystalline ones, are economically unsound because of the high cost of their manufacturing techniques [6]. In this connection, of current concern become basically new approaches to thermoelectric conversion efficiency improvement that are not related to increase in material figure of merit, but are aimed at developing rational recovery schemes of supplied heat [7-9].

Practical application of such schemes has resulted in creation of staged thermoelectric modules based on Bi_2Te_3-*PbTe-TAGS*, where each stage is oriented at its own level of operating temperatures, which allowed improving the efficiency of thermoelectric conversion by a factor of ~1.5 [10-12]. In turn, for further efficiency improvement of staged structures none of the variants of thermal schemes is used yet.

On the other hand, the efficiency of thermoelectric converters can be increased by making thermoelement legs in the form of segments, rather than of homogeneous materials. In so doing, for each segment one can choose different material in the corresponding temperature range, so as to assure maximum figure of merit of leg as a whole [13, 14].

So, the purpose of our work is to estimate the possibility of efficiency improvement of staged thermoelectric modules of materials based on Bi_2Te_3-*PbTe-TAGS* through use of segmented legs in thermoelements of each stage.

Physical model of a staged module with segmented legs and its description

A physical model of a staged module with segmented legs is given in Fig. 1, *a*. Each stage is composed of thermoelements in the form of segments of different thermoelectric materials, connected electrically in series and thermally in parallel. For computer design use was made of a model of elementary structural unit of such module, namely a block of two thermoelements composed of N segments. Each thermoelement is optimized for the level of working temperatures of the “hot” and “cold” stage, respectively (Fig. 1, *b*).

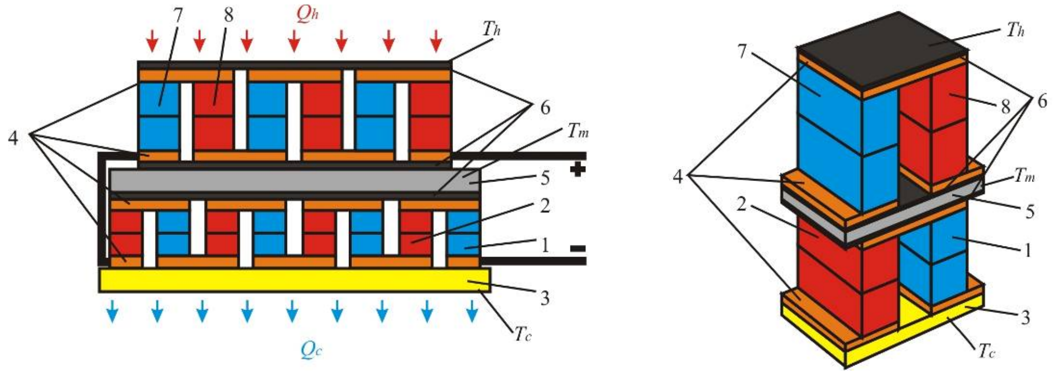

a) *b)*

Fig. 1. Physical model of a two-staged module (a) and its elementary structural unit (b):
1, 2 – segmented n-andi p-legs of the cold stage; 3 – ceramic plate;
4 – connecting plates; 5 –heat-conductive plate;
6 – electric insulation; 7, 8 – segmented n-and p-legs of the hot stage.

The model takes into account contact resistance between the legs, leg segments and connecting plates. The temperatures on the heat releasing and heat absorbing thermoelement surfaces T_h and T_c are fixed, the lateral surface is adiabatically isolated. Parameters of thermoelectric materials are a function of temperature and concentration of doping impurities. The space between the legs is filled with the air of thermal conductivity κ_{air}. To determine maximum efficiency, it is necessary to find optimal distribution of current density in the stages and optimal inter-stage temperature.

The formulated problem is solved by a numerical method of successive approximations with the use of “Comsol Multiphysics” program [15]. The choice of geometrical dimensions of thermoelements helps to achieve the electrical compatibility of stages and matching between stages in thermal flux.

Mathematical description of the model

For the description of heat and electric current fluxes in such thermoelement we used the laws of conservation of energy

$$\operatorname{div}\vec{W} = 0, \tag{1}$$

and electric charge

$$\operatorname{div}\vec{j} = 0, \tag{2}$$

where

$$\vec{W} = \vec{q} + U\vec{j}, \tag{3}$$

$$\vec{q} = \kappa\nabla T + \alpha T\vec{j}, \tag{4}$$

$$\vec{j} = -\sigma\nabla U - \sigma\alpha\nabla T, \tag{5}$$

where $\vec{W}$ is energy flux density, $\vec{j}$ is electric current density, U is electric potential, T is temperature, α, σ, κ are the Seebeck coefficient, electric conductivity and thermal conductivity of materials.

Taking into account (3) - (5), we obtain:

$$\vec{W} = -(\kappa + \alpha^2\sigma T + \alpha U\sigma)\nabla T - (\alpha\sigma T + U\sigma)\nabla U\,. \tag{6}$$

Then the laws of conservation (1), (2) acquire the form:

$$-\nabla\left[(\kappa + \alpha^2\sigma T + \alpha U\sigma)\nabla T\right] - \nabla\left[(\alpha\sigma T + U\sigma)\nabla U\right] = 0\,, \tag{7}$$

$$-\nabla(\sigma\alpha\nabla T) - \nabla(\sigma\nabla U) = 0\,. \tag{8}$$

Exactly these nonlinear second-order differential equations in partial derivatives (7) and (8) determine the distributions of temperature T and potential U in materials of the legs, the contact, connecting and isolation layers of thermoelement.

The boundary conditions for solving of equations (7) and (8) were selected as follows. The temperatures of heat absorbing and heat releasing thermoelement surfaces T_h = 200 °C and T_c = 30 °C were recorded. The zero potential value was assigned on the connecting plate of *n*-type leg. On the other connecting plate of *p*-type leg, the value U was assigned, that is half of thermopower generated by thermoelement. In turn, the value of generated thermopower was determined by a system of equations (7) and (8) in the absence of current through thermoelement.

At the boundaries of the legs and contact layer, the contact layer and connecting plates, the insulation and connecting plates, conditions of equality of temperatures and heat fluxes were taken into account.

The general equation of "Comsol Multiphysics" program is of the form:

$$\nabla\left(-C\nabla M + \alpha M + \gamma\right) + \delta M + \beta\nabla M = f\,, \tag{9}$$

where

$$C = \begin{bmatrix} C_{11} & C_{12} \\ C_{21} & C_{22} \end{bmatrix},\ \alpha = \begin{bmatrix} \alpha_{11} & \alpha_{12} \\ \alpha_{21} & \alpha_{22} \end{bmatrix},\ \gamma = \begin{bmatrix} \gamma_{11} & \gamma_{12} \\ \gamma_{21} & \gamma_{22} \end{bmatrix},\ \delta = \begin{bmatrix} \delta_{11} & \delta_{12} \\ \delta_{21} & \delta_{22} \end{bmatrix},$$

$$\beta = \begin{bmatrix} \beta_{11} & \beta_{12} \\ \beta_{21} & \beta_{22} \end{bmatrix},\ f = \begin{bmatrix} f_1 \\ f_2 \end{bmatrix},\ M = \begin{bmatrix} T \\ U \end{bmatrix}. \tag{10}$$

From the analysis of equations (7) – (10) it follows that equation (9) can be simplified as follows:

$$\nabla\left(-C\nabla M\right) = 0\,. \tag{11}$$

A differential equation for matrix components M is given by:

$$\left.\begin{aligned} \nabla\left(-C_{11}\nabla T\right) + \nabla\left(-C_{12}\nabla U\right) = 0 \\ \nabla\left(-C_{21}\nabla T\right) + \nabla\left(-C_{22}\nabla U\right) = 0 \end{aligned}\right\}. \tag{12}$$

Comparison of the laws of conservation in the form of (7), (8) to equations (12) yields coefficients for computer model:

$$C = \begin{pmatrix} \kappa + \alpha^2\sigma T + \alpha U\sigma & \alpha\sigma T + U\sigma \\ \sigma\alpha & \sigma \end{pmatrix}. \tag{13}$$

Investigation results

The above method was used to calculate the energy characteristics of two-staged modules with two- and three-segmented legs. As the input data, the experimentally measured in [16-18] temperature dependences of thermoelectric parameters α, σ, κ of materials based on *n*- and *p-*Bi_2Te_3 for the cold stage and *n-PbTe* and *p-TAGS* for the hot stage, respectively, were used.

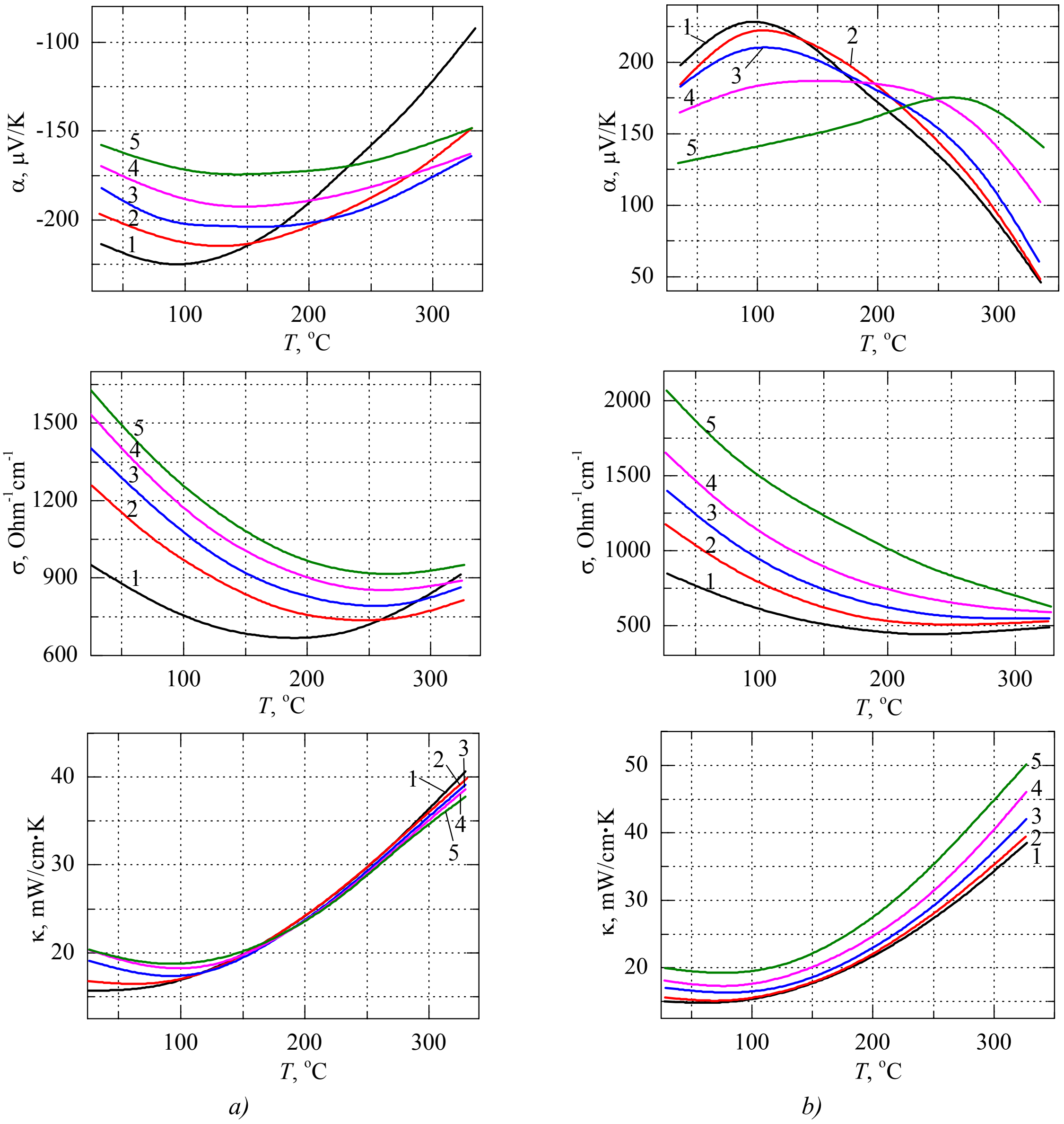

a) *b)*

Fig. 2. Temperature dependences of thermoelectric parameters of the cold stage materials with different electric conductivity values σ_0^n, σ_0^p *at T=300 K [16]:*

a) n- $(Bi_2Te_3)_{0.90}(Sb_2Te_3)_{0.05}(Sb_2Se_3)_{0.05}$*, doped with iodine*

(1 – σ_0^n *=970 Ohm*$^{-1}$*cm*$^{-1}$*; 2 –* σ_0^n *=1250 Ohm*$^{-1}$*cm*$^{-1}$*;*

3 – σ_0^n *=1400 Ohm*$^{-1}$*cm*$^{-1}$*; 4 –* σ_0^n *=1550 Ohm*$^{-1}$*cm*$^{-1}$*; 5 –* σ_0^n *=1650 Ohm*$^{-1}$*cm*$^{-1}$*);*

b) p- $(Bi_2Te_3)_{0.25}(Sb_2Te_3)_{0.72}(Sb_2Se_3)_{0.03}$*, doped with lead*

(1 – σ_0^p *=880 Ohm*$^{-1}$*cm*$^{-1}$*; 2 –* σ_0^p *=1100 Ohm*$^{-1}$*cm*$^{-1}$*; 3 –* σ_0^p *=1380 Ohm*$^{-1}$*cm*$^{-1}$*;*

4 – σ_0^p *=1660 Ohm*$^{-1}$*cm*$^{-1}$*; 5 –* σ_0^p *=2000 Ohm*$^{-1}$*cm*$^{-1}$*).*

The temperature dependences given in Figs. 2, 3 were approximated by two-dimensional polynomials (Fig. 4, 5) in the form of $\alpha^{n,p} = \alpha^{n,p}(x_0^{n,p}, T)$, $\sigma^{n,p} = \sigma^{n,p}(x_0^{n,p}, T)$, $\kappa^{n,p} = \kappa^{n,p}(x_0^{n,p}, T)$ whose coefficients were introduced into computer program.

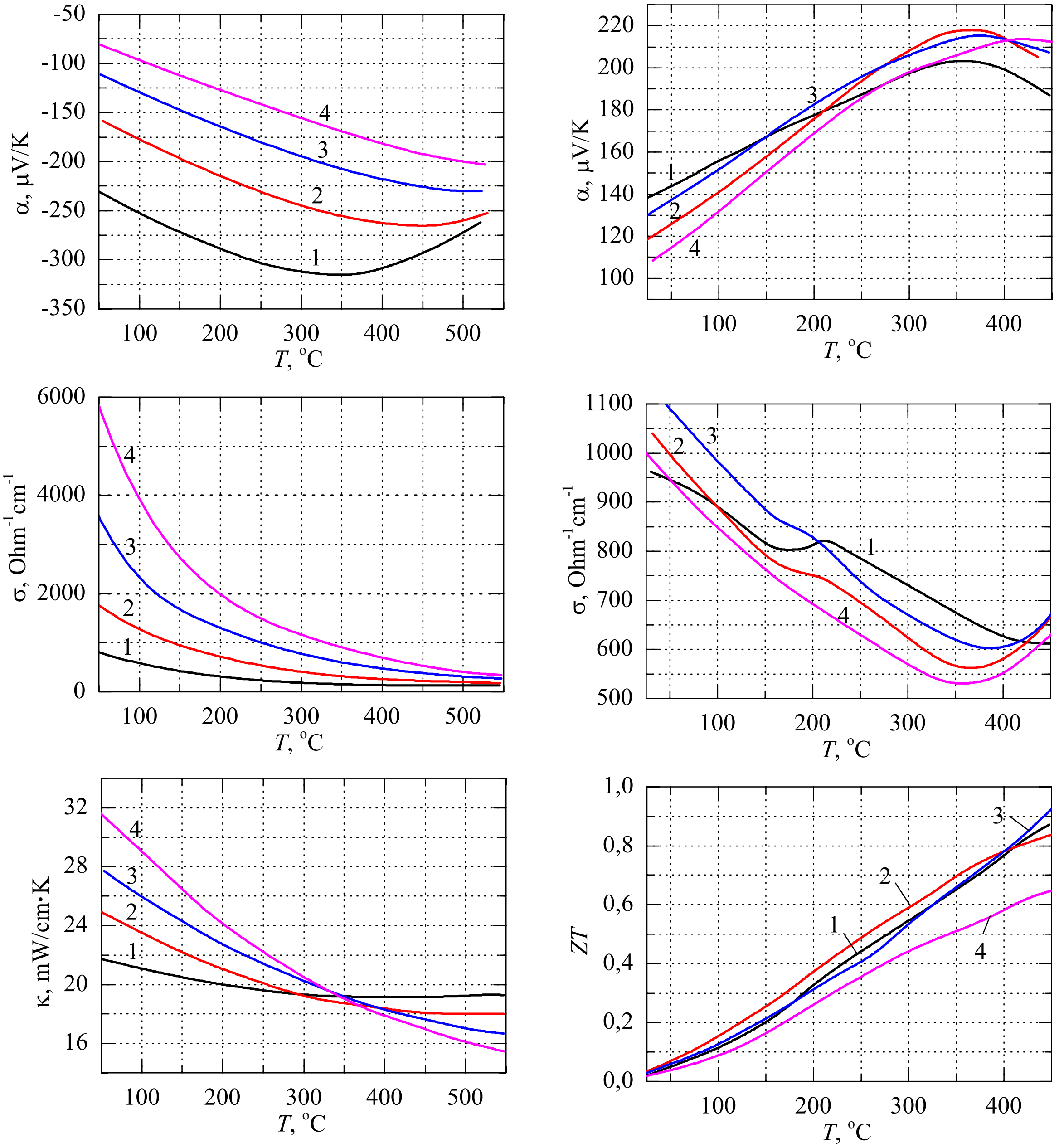

a)

b)

Fig. 3. Temperature dependences of thermoelectric parameters of the hot stage materials n-PbTe and p-TAGS:
a) PbTe <x mol.% PbI_2> (1 – x=0.01; 2 – x=0.03; 3 – x=0.055; 4 – x=0.1) [17];
b) $(GeTe)_{80}(Ag_ySb_{2-y}Te_{3-y})_{20}$ (1 – y= 0.8; 2 – y= 1.0; 3 – y= 1.2; 4 – y= 1.4) [18].

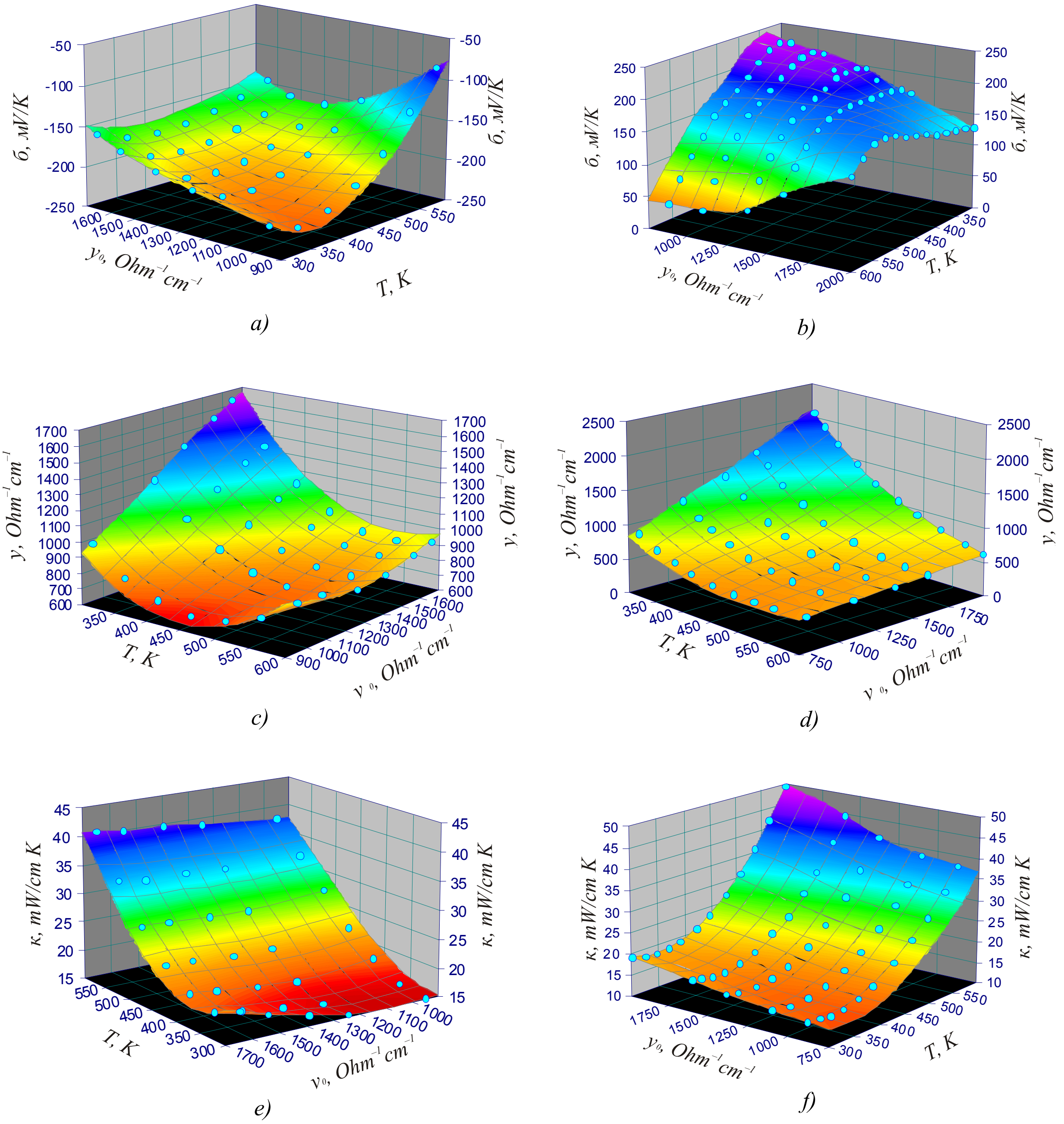

a) *b)*

c) *d)*

e) *f)*

Fig. 4. Temperature-concentration dependences of thermoelectric parameters of the cold stage materials
a), c), e) n-$(Bi_2Te_3)_{0.90}(Sb_2Te_3)_{0.05}(Sb_2Se_3)_{0.05}$, doped with iodine.
b), d), f) p-$(Bi_2Te_3)_{0.25}(Sb_2Te_3)_{0.72}(Sb_2Se_3)_{0.03}$, doped with lead.

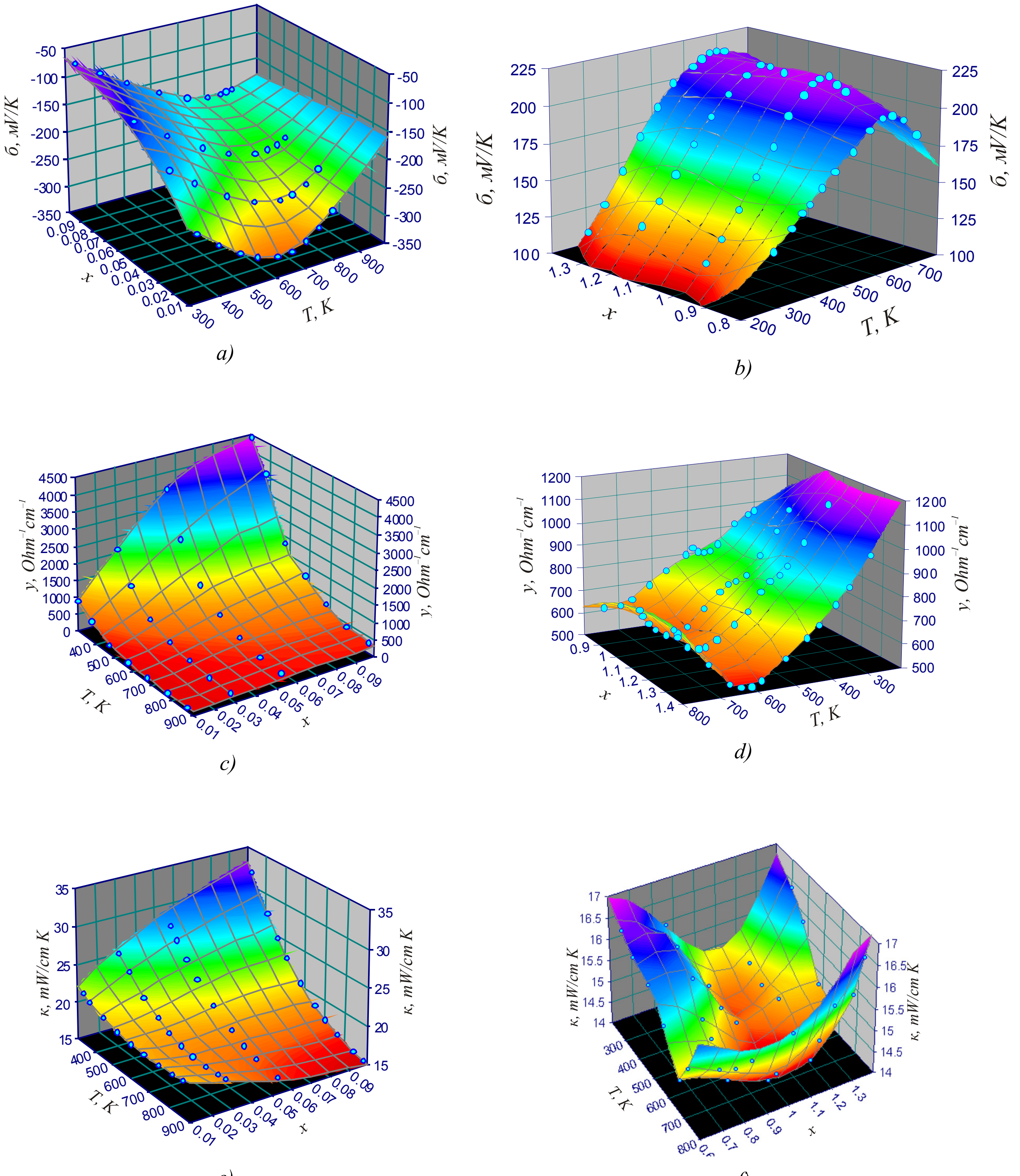

a) *b)*

c) *d)*

e) *f)*

Fig. 5. Temperature-concentration dependences of thermoelectric parameters of the hot stage materials: a), c), e) n-PbTe < x mol.% PbI_2 > ;b), d), f) p-$(Ag_{0.5}Sb_{0.5}Te1_{1-x}(Pb_{0.16}Ge_{0.84}Te)_x$.

As a result of simulation, the distributions of temperature and electric potential in a two-stage module with two-segmented and three-segmented legs were obtained (Figs. 6, 7).

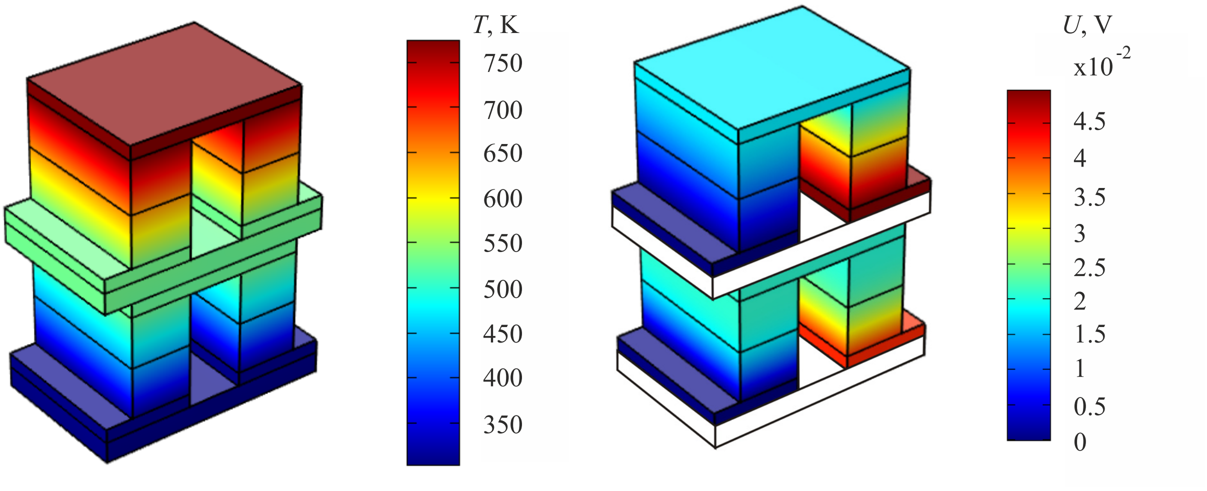

a) *b)*

Fig. 6. Distribution of temperatures (a) and potential (b) in a staged module with two-segmented legs.

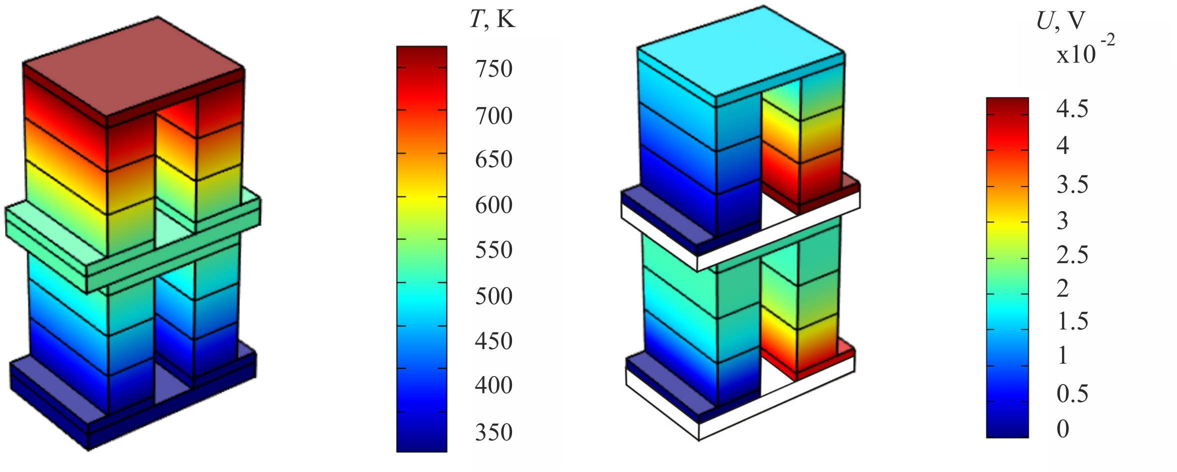

a) *б)*

Fig. 7. Distribution of temperatures (a) and potential (b) in a staged module with three-segmented legs.

Optimal parameters of segment materials for a staged module are given in Table 1. Optimization was carried out by determination of such impurity concentrations in each segment materials whereby the efficiency of a staged module in the temperature range of 30–250 °C and 250–500 °C reaches its maximum value. The values of contact resistances in the calculations were taken to be $5\cdot10^{-6}$ Ohm·cm on thermoelement junctions and $1\cdot10^{-5}$ Ohm·cm on the boundaries between leg segments.

Table 1

Optimal segment materials in a staged module

Module	Stage	Leg	Segment	Material	Concentration
Staged with two-segmented legs	cold	*n*-type	First	$(Bi_2Te_3)_{0.90}(Sb_2Te_3)_{0.05}(Sb_2Se_3)_{0.05}$, doped with iodine	σ_0 =1250 Ohm^{-1}cm^{-1}
			Second		σ_0 = 1400 Ohm^{-1}cm^{-1}
		p-type	First	$(Bi_2Te_3)_{0.25}(Sb_2Te_3)_{0.72}(Sb_2Se_3)_{0.03}$, doped with lead	σ_0 = 1100 Ohm^{-1}cм$^{-1}$
			Second		σ_0 = 2000 Ohm^{-1}cm^{-1}
	hot	*n*-type	First	$PbTe+x$ mol.% PbI_2	$x = 0.055$
			Second		$x = 0.1$
		p-type	First	$(Ag_{0.5}Sb_{0.5}Te)_{1-x}(Pb_{0.16}Ge_{0.84}Te)_x$	$x = 0.58$
			Second		$x = 0.6$
Staged with three-segmented legs	cold	*n*-type	First	$(Bi_2Te_3)_{0.90}(Sb_2Te_3)_{0.05}(Sb_2Se_3)_{0.05}$, doped with iodine	σ_0 = 1380 Ohm^{-1}cm^{-1}
			Second		σ_0 = 1660 Ohm^{-1}cm^{-1}
			Third		σ_0 = 2000 Ohm^{-1}cm^{-1}
		p-type	First	$(Bi_2Te_3)_{0.25}(Sb_2Te_3)_{0.72}(Sb_2Se_3)_{0.03}$, doped with lead	σ_0 = 1250 Ohm^{-1}cm^{-1}
			Second		σ_0 = 1400 Ohm^{-1}cm^{-1}
			Third		σ_0 = 1550 Ohm^{-1}cm^{-1}
	hot	*n*-type	First	$PbTe+x$ mol.% PbI_2	$x = 0.6$
			Second		$x = 0.6$
			Third		$x = 0.6$
		p-type	First	$(Ag_{0.5}Sb_{0.5}Te)_{1-x}(Pb_{0.16}Ge_{0.84}Te)_x$	$x = 0.055$
			Second		$x = 0.055$
			Third		$x = 0.1$

Fig. 8 *a, b* shows the efficiency of a staged module with two- and three-segmented legs as a function of inter-stage temperature.

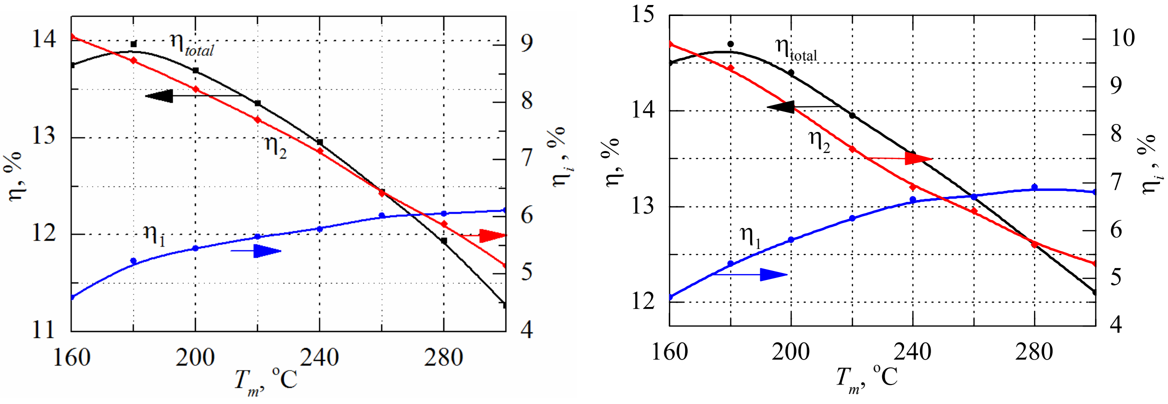

a) *b)*

Fig. 8. Efficiency of the cold η_1 and hot η_2 stages, as well as total efficiency η_{total} of a two-stage module with: a) two-segmented legs; b) three-segmented legs versus inter-stage temperature T_m (T_h=500°C, T_c= 30°C).

As is evident from the above data, maximum efficiency of a staged module with two-segmented legs is 14% at inter-stage temperature 180°C. With this inter-stage temperature, the hot side temperature 500°C, and the cold side temperature 30°C, the distribution of efficiency between the stages is as follows: the cold stage – 5.2%, the hot stage – 8.8% (Fig. 8, *a*). In the case of three-segmented legs (Fig. 8, *b*) maximum efficiency of a staged module increases to 14.7 %, which is mainly related to increase in hot stage η (η_2 = 9.4%). The use of the third segment in the cold stage has no significant impact on the increase in total efficiency η_{total} of the module (η_1 = 5.3%).

Fig. 9 presents comparative dependences of the efficiency of a two-staged module based on *Bi_2Te_3-PbTe-TAGS* materials with the homogeneous, two- and three-segmented legs on the inter-stage temperature.

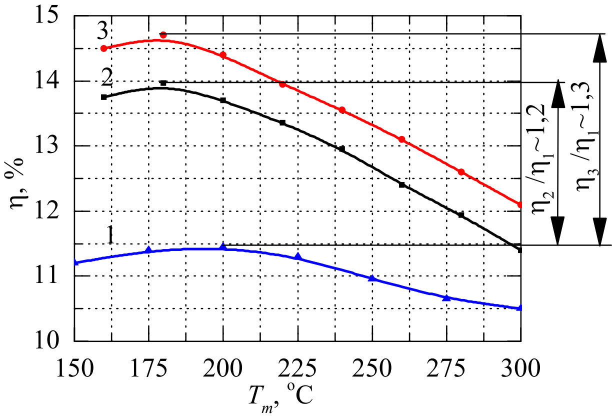

Fig. 9. The efficiency of a two-staged module with
1 – homogeneous legs; 2 – two-segmented legs;
3 –three-segmented legs versus inter-stage temperature T_m.

From the analysis of Fig. 9 it follows that maximum efficiency increase of a two-staged module of *Bi_2Te_3-PbTe-TAGS* in the operating temperature range 30-500 °C is observed when passing from one- to two-segmented leg and makes ~ 20%. Due to introduction of the third segment the efficiency of thermoelectric conversion can be increased by another 5%.

In order to investigate the influence of the number of segments on total module efficiency, similar calculations were performed for a two-stage module with four-segmented legs (Fig. 10).

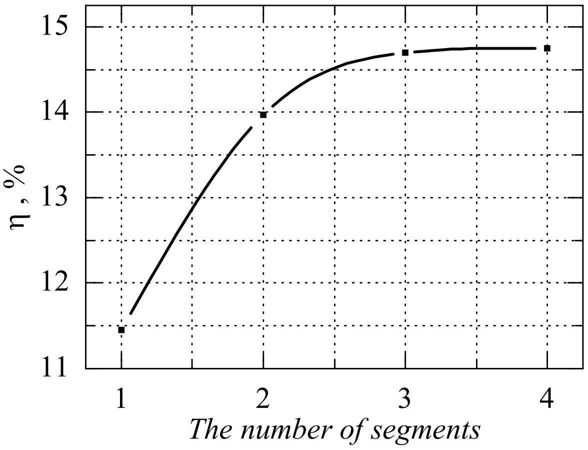

Fig. 10. Dependence of maximum efficiency of a two-stage module of materials based on Bi_2Te_3-PbTe-TAGS on the number of segments in thermoelement legs.

Calculations show that the use of four segments in the legs of each stage is unreasonable, since the efficiency of such module will make ~14.75%. The contribution of the fourth segment to maximum efficiency increase does not exceed 0.5% as compared to a module with three-segmented legs. Such efficiency behaviour is caused primarily by additional contact resistance at points of segments connection, which in turn leads to the Joule heat increase.

Based on the results of computer design, the electrical parameters of elementary structural unit of a two-staged module were calculated for the case of two- and three-segmented legs (Table 2).

Table 2

Electrical parameters of the elementary structural unit
of a two-staged module with two- and three-segmented legs.
Cross-section of legs is 1.8×4.3 mm

Number of segments	U, V	I, A	P, W	Height of stage legs, mm
2 segments	0.09	2.76	0.25	h_1=3 mm h_2=7 mm
3 segments	0.09	3.1	0.28	h_1=3 mm h_2=7,5 mm

Using the data given in Table 2, one can design a thermoelectric generator module with the required electrical characteristics. For instance, for creation of a two-staged module with two-segmented legs of electric power 5 W, on condition of a series connection of thermoelements, it is necessary to have 20 “blocks”. In so doing, the output electric voltage of such module will be 1.8 V.

Conclusions

1. The method for efficiency improvement of thermoelectric two-staged generator modules of materials based on *Bi_2Te_3-PbTe-TAGS* through use of segmented legs in thermoelements of each stage is presented .
2. Computer methods were used in the design and to determine the efficiency of such modules with two- and three-segmented legs in the operating temperature range 30–500°C. It is shown that maximum efficiency of staged modules with two- and three-segmented legs is achieved at inter-stage temperature 180 °C and makes 14% and 14.7%, respectively.
3. The use in module stages of thermoelements with two- and three-segmented legs allows improving the efficiency of thermoelectric power conversion by 20-25% as compared to a conventional staged module based on *Bi_2Te_3-PbTe-TAGS*. Further increase in the number of leg segments in stages is ineffective because of increased heat release at points of contact resistances.

References

1. A.F. Ioffe, Thermoelectricity in Semiconductors, *Zhurnal Tekhnicheskoi Fiziki* **23**(8), 1452 − 1459 (1953).
2. A.F. Ioffe, On the Improvement of Semiconductor Thermocouple Efficiency, *DAN SSSR* **106**(6), 981–983 (1956).
3. B.M. Goltsman, V.A. Kudinov, and I.A. Smirnov, *Semiconductor Thermoelectric Materials Based on Bi_2Te_3* (Moscow: Nauka, 1972), 320 p.
4. W.M. Yim, F.D. Rosi, Compound Telluride and Their Alloys for Peltier Cooling, *Solid-State Electronics* **15**(10), 1121 – 1134 (1972).

5. L.I. Anatychuk, L.N. Vikhor, *Thermoelectricity: Functionally Graded Thermoelectric Materials*, Vol.IV (Chernivtsi, 2012), 172 p.
6. L.P. Bulat, L.V. Bochkov, I.A. Nefedova, and R. Ahiska, Nanostructurization as a Method for Efficiency Improvement, *Scientific and Technical Journal of Information Technologies, Mechanics and Optics* **4**(92), 48-56 (2014).
7. L.I. Anatychuk, O.J. Luste, and V.Ya. Mykhailovsky, Organic–Fueled Sectional Thermoelectric Generators, *J.Thermoelectricity* **4**, 20-25 (2005).
8. V.Ya. Mykhailovsky, Physical Models of Organic-Fueled Thermogenerators. Main Ways for Their Efficiency Improvement and Expansion of Practical Application, *J.Thermoelectricity* **2**, 7-42 (2005).
9. L.I. Anatychuk, V.Ya. Mykhailovsky, Two-Sectional Gas-Fueled Thermoelectric Generator, *J.Thermoelectricity* 1, 76-86 (2008).
10. L.I. Anatychuk, L.N. Vikhor, Computer Design of Staged Generator Modules, *J.Thermoelectricity* 4, 19 – 27 (2002).
11. V.Ya. Mykhailovsky, V.R. Bilinsky-Slotylo, Thermoelectric Staged Modules of Materials Based on Bi_2Te_3-*PbTe-TAGS*, *J.Thermoelectricity* 4, 67-74 (2012).
12. L.M. Vikhor, V.Ya. Mikhailovsky, and R.M. Mochernyuk, Materials Optimization and Performance Evaluation of Generator Modules for Heat Recuperators, *Physics and Chemistry of the Solid State* 1(15), 206-213 (2014).
13. L.I. Anatychuk, L.M.Vikhor, I.Yu. Ludchak, and I.S. Termena, Design and Technology of Generator Modules of Segmented Thermoelements Based on Bi-Te, *J.Thermoelectricity* **1**, 58-69 (2010).
14. L.T. Strutynska, V.R. Bilinsky-Slotylo, and V.Ya. Mykhailovsky, Design of Segmented Modules Based on *PbTe/TAGS* for Thermoelectric Generators, *Physics and Chemistry of the Solid State* **4**(13), 1032-1036 (2012).
15. http://www.comsol.com
16. L.N. Vikhor, L.I. Anatychuk, Generator Modules of Segmented Thermoelements, *Energy Conversion and Management* **50**, 2366 (2009).
17. V.N. Shperun, D.M. Freik, and R.I. Zapuklyak, *Thermoelectricity of Lead Telluride and Its Analogs* (Ivano-Frankivsk: Plai, 2000), 250 p.
18. A. Yusufu, K. Kurosaki, T. Sugahara et al., Thermoelectric Properties and Microstructures of $AgSbTe_2$-Added *p*-type $Pb_{0.16}Ge_{0.84}Te$, *Phys. Status Solidi A* **209** (1), 167 (2012).

O.V. Yevdulov, D.V. Yevdulov


O.V. Yevdulov

Federal State Budgetary Educational Institution of
Higher Professional Education “Dagestan State
Technical University”, 70, Imam Shamil avenue,
Makhachkala, 367015, Russia


D.V. Yevdulov

THEORETICAL STUDIES OF A LAYER-STRUCTURED THERMOELECTRIC ELEMENT

This paper is concerned with a model of a layer-structured thermoelectric element and presents the results of its theoretical studies. The thermoelement model makes it possible to study the thermophysical and thermomechanical processes occurring in it on the basis of solving the unsteady-state equation of thermal conductivity, the equilibrium, the continuity and the Duhamel-Neumann equations for a multi-layered system by a numerical finite element method. The results are represented as two-dimensional and one-dimensional plots of temperature, thermomechanical stresses and deformations at different thermoelement points.

Key words: thermoelement, cooling plant, temperature field, thermomechanical stresses and deformations, model, numerical finite element method.

Introduction

A continuous and stable operation of a number of devices can be achieved only under the necessary temperature conditions created for them. As a rule, the temperature operating conditions of thermally loaded devices are assured by special cooling systems, cooling plants. The latter are rather versatile, complicated, can have considerable dimensions, mass and energy consumption. In many cases, mass, dimensions and reliability of thermal-control systems are not always comparable to the respective parameters of cooled objects, which is particularly relevant for microminiature devices with high specific thermal fluxes. In this case, the problem of temperature stabilization of such equipment can be solved by using thermoelectric devices as cooling plants, optimally matched with this equipment in the most important energy and weight-size parameters.

The basic element of any thermoelectric device is a semiconductor thermoelement the types of which are covered adequately in [1-3]. Among them one should mention thermocouple, anisotropic, eddy and short-circuited thermoelements, thermoelements working in a magnetic field and at high temperature gradients, as well as piezothermoelements. The most widespread is classical flat-topped embodiment of these elements, when electric current is supplied perpendicular to heat flux on their cold and hot junctions. However, in the design of relatively high-power small-size cooling plants (of more than 1 kW power) based on this type of thermoelement, it is relevant to assure their reliable operation during the entire cycle of cooled equipment operation.

Thus, the existing low-current thermopiles, when used in large quantities, offer insufficient reliability due to increasing number of thermoelements, and, accordingly, soldered connections, as well as low thermodynamic characteristics. Low-current flat-topped thermopiles in this respect are better, but due to the presence of large heat fluxes on the junctions they have low thermomechanical characteristics.

To improve them, copper connecting plates are most often used with lead damping pads [4] which owing to their elasticity relieve thermoelement legs from stresses, though the electrical and thermal contact resistance is simultaneously increased. With low temperature differences, split connecting plates are sometimes used [5], with their thin jumpers offering elasticity and a low electric resistance due to their small length. In a number of designs, application has been found by compensated connecting plates and plates with different length on the cold and hot thermoelement sides [4]. Both designs call for the presence of increased gaps between thermoelement legs, which increases the value of heat flux from the hot to cold junctions through isolation and decreases useful cooling capacity.

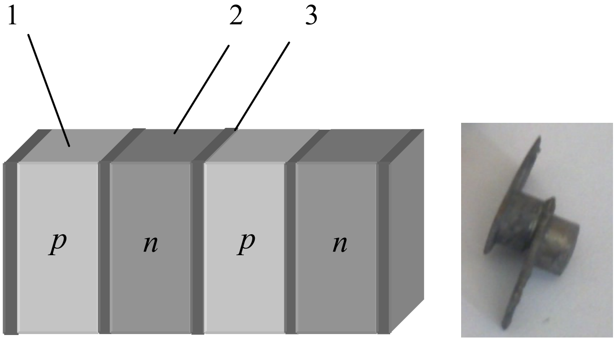

Fig.1. Design and external view of a layer-structured thermopile fragment.
1 and 2 – p- and n-type leg, 3 – connecting plates.

Under such conditions, it seems advisable to employ layer-structured thermopiles (Fig.1) wherein the direction of electric current along thermolement does not change, the design is not rigid, owing to which the emerging thermomechanical stresses can be eliminated or reduced considerably.

Dagestan Technical University has patented a number of solutions [6-14] implementing said concept that are different in the method of heat supply to and rejection from connecting elements, as well as in some other structural features.

The purpose of this paper is to develop a model and perform theoretical studies of a layer-structured thermoelement serving the basis for given technical solutions that will make it possible to optimize and determine the most advisable operating modes of the latter.

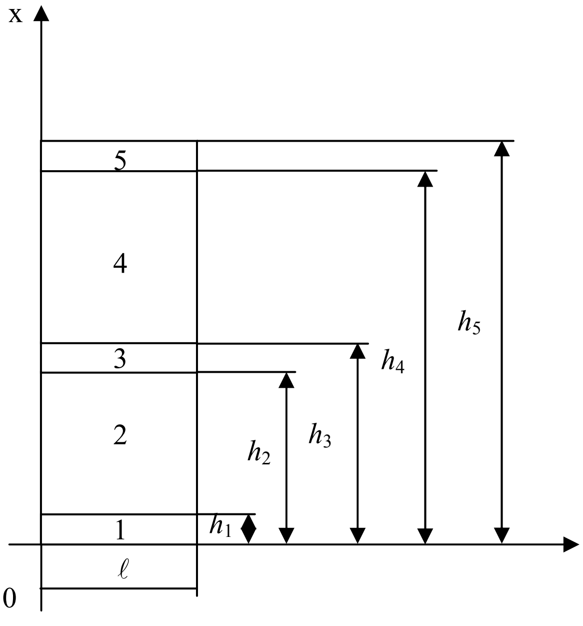

Fig.2. Calculation diagram of a layer-structured thermoelement.

Simulation of a layer-structured thermoelement includes calculation of its temperature field and thereupon determination of the respective thermomechanical characteristics.

Simulation of thermophysical processes and calculation of temperature field of a layer-structured thermoelement

In practice, in the majority of cases in operation of a thermopile, thermal isolation along its lateral surface is provided, except for contact surfaces with cooled object and heat rejection system. Therefore, with a sufficient degree of accuracy at simulation of a thermoelement one can consider a two-dimensional thermal conductivity problem. The calculation diagram for these conditions is shown in Fig. 2. The areas 1, 3 and 5 are connecting plates, 2 and 4 – thermoelectric material.

A system of differential heat transfer equations for this schematic is given by:

$$\begin{gathered}
\lambda_1 \frac{\partial^2 T_1}{\partial x^2} + \lambda_1 \frac{\partial^2 T_1}{\partial y^2} + j^2 \Omega_1 = C_1 \frac{\partial T_1}{\partial t}, \\
\lambda_2 \frac{\partial^2 T_2}{\partial x^2} + \lambda_2 \frac{\partial^2 T_2}{\partial y^2} + j^2 \Omega_2 = C_2 \frac{\partial T_2}{\partial t}, \\
\lambda_3 \frac{\partial^2 T_3}{\partial x^2} + \lambda_3 \frac{\partial^2 T_3}{\partial y^2} + j^2 \Omega_3 = C_3 \frac{\partial T_3}{\partial t}, \\
\lambda_4 \frac{\partial^2 T_4}{\partial x^2} + \lambda_4 \frac{\partial^2 T_4}{\partial y^2} + j^2 \Omega_4 = C_4 \frac{\partial T_4}{\partial t}, \\
\lambda_5 \frac{\partial^2 T_5}{\partial x^2} + \lambda_5 \frac{\partial^2 T_5}{\partial y^2} + j^2 \Omega_5 = C_5 \frac{\partial T_5}{\partial t},
\end{gathered} \tag{1}$$

where λ_i is thermal conductivity coefficient, Ω_i is electric resistivity, j is electric current density, C_i is volumetric heat capacity, T_i is temperature, $i = 1,\ldots, 5$, t is time.

The initial, boundary and matching conditions are as follows:

$$\begin{gathered}
T_{1,2,3,4,5} = T_{amb} \text{ at } t = 0, \\
\lambda_1 \frac{\partial T_1}{\partial x} = \beta_{hr}\left(T_1 - T_{hr}\right) \text{ at } x = 0,\ 0 < y < \ell, \\
\lambda_1 \frac{\partial T_1}{\partial x} = \lambda_2 \frac{\partial T_2}{\partial x} + \alpha_{12} j T_2 \text{ at } x = h_1,\ 0 < y < \ell, \\
\lambda_2 \frac{\partial T_2}{\partial x} - \alpha_{23} j T_2 = \lambda_3 \frac{\partial T_3}{\partial x} \text{ at } x = h_2,\ 0 < y < \ell, \\
\lambda_3 \frac{\partial T_3}{\partial x} = \lambda_4 \frac{\partial T_4}{\partial x} - \alpha_{34} j T_4 \text{ at } x = h_3,\ 0 < y < \ell, \\
\lambda_4 \frac{\partial T_4}{\partial x} + \alpha_{45} j T_4 = \lambda_5 \frac{\partial T_5}{\partial x} \text{ at } x = h_4,\ 0 < y < \ell, \\
\lambda_5 \frac{\partial T_5}{\partial x} = \beta_{hr}\left(T_5 - T_{hr}\right) \text{ at } x = h_5,\ 0 < y < \ell, \\
\lambda_1 \frac{\partial T_1}{\partial y} = \beta\left(T_1 - T_{amb}\right) \text{ at } y = 0,\ \ell,\ 0 \le x \le h_1, \\
\lambda_2 \frac{\partial T_2}{\partial y} = \beta\left(T_2 - T_{amb}\right) \text{ at } y = 0,\ \ell,\ h_1 < x \le h_2, \\
\lambda_3 \frac{\partial T_3}{\partial y} = \beta\left(T_3 - T_{amb}\right) \text{ at } y = 0,\ \ell,\ h_2 < x \le h_3, \\
\lambda_4 \frac{\partial T_4}{\partial y} = \beta\left(T_4 - T_{amb}\right) \text{ at } y = 0,\ \ell,\ h_3 < x \le h_4, \\
\lambda_5 \frac{\partial T_5}{\partial y} = \beta\left(T_5 - T_{amb}\right) \text{ at } y = 0,\ \ell,\ h_4 < x \le h_5,
\end{gathered} \tag{2}$$

where T_{amb} is ambient temperature, α is the Seebeck coefficient, β is coefficient of heat exchange with the environment, β_{hr} is coefficient of heat exchange with heat rejection system, T_{hr} is temperature of heat rejection system.

The system of equations (1) with the respective initial and boundary conditions (2) was solved with the use of finite element method.

Figs. 3, 4 show, accordingly, a two-dimensional temperature field of a layer-structured thermoelement, as well as a distribution of heat flux density on reaching the steady-state mode. As the initial data there were used: $\lambda_1 = \lambda_3 = \lambda_5 = 395$ W/(m·K), $\lambda_2 = \lambda_4 = 1.5$ W/(m·K), $\rho_1 = \rho_3 = \rho_5 = 0.0172\cdot10^{-6}$ Ohm·m, $\rho_2 = \rho_4 = 10.65\cdot10^{-6}$ Ohm·m, $C_1 = C_3 = C_5 = 383$ J/(kg·K), $C_2 = C_4 = 123$ J/(kg·K), $T_{amb} = 293$ K, $T_0 = 291$ K, $\alpha = 0.2\cdot10^{-3}$ V/K, $\beta = 10$ W/(m^2·K), $T_{hr} = 291$ K, $\beta_{hr} = 70$ W/(m^2·K).

The value of heat flux was found from the ratio:

$$F_{xi} = \lambda_i \frac{\partial T_i}{\partial x},\ F_{yi} = \lambda_i \frac{\partial T_i}{\partial y},\ \text{where } i = 1,\ldots,5.$$

Figs. 5-6 show, accordingly, the distribution of thermoelement temperature along its longitudinal axis at different supply current values, as well as a variation of temperature in time at different points of a layer-structured thermoelement.

As it follows from the resulting data, with the use of a layer-structured thermoelement one can obtain a considerable temperature difference between the cold and hot connecting plates with a large heat flux value. Thus, at temperature difference between connecting plates 47 K, heat flux on the cold junction of thermoelement, proportional to its cooling capacity, is of the order of 18000 W/m^2, which corresponds at given thermoelement geometry to supply current 140 A. With a decrease in supply electric current, the value of heat flux on the cold junction of thermoelement and temperature difference between its junctions are also reduced. In so doing, the reduction of thermoelement supply current from 140 A to 80 A reduces temperature difference between thermoelement junctions from 47 K to 31 K, consequently heat flux on the cold junction is reduced from 18000 W/m^2 to 12000 W/m^2.

Fig. 6 shows the variation of temperature of the cold and hot connecting plates, as well as different points of thermoelement leg in time at supply current 140 A. According to the represented data, the temperature at above points reaches the steady-state mode in about 900 sec. This fact is related to sufficiently large overall dimensions of thermoelement. With the thickness of connecting plates 2 mm and thermoelement legs height 4 mm, the cross-section area is $400\cdot10^{-6}$ m^2. In so doing, as it follows from the calculated data, it would be advisable to provide for heat rejection not only from the hot connecting plates, but also from the adjacent surface of thermoelement legs. In this design it is possible to propose additional heat rejection from about 1/3 of thermoelement lateral surface.

Simulation of thermomechanical processes in a layer-structured thermoelement

To estimate thermomechanical characteristics of a layer-structured thermoelement, calculation of mechanical stresses and deformations emerging in it due to thermal expansion of materials has been made.

The relations between mechanical stresses σ_x, σ_y, τ_{xy} and deformations ε_x and ε_y are given by the Duhamel-Neumann relations:

$$\varepsilon_x = \frac{1}{E}(\sigma_x - \nu\sigma_y) + \gamma T,$$

$$\varepsilon_y = \frac{1}{E}(\sigma_y - \nu\sigma_x) + \gamma T,$$

$$\gamma_{xy} = \frac{2(1+\nu)}{E}\tau_{xy},$$

where E is Young's modulus, ν is the Poisson coefficient, γ is linear expansion coefficient, indexes x, y, xy define the direction of values action, whereby index xy means the diagonal pattern of values action.

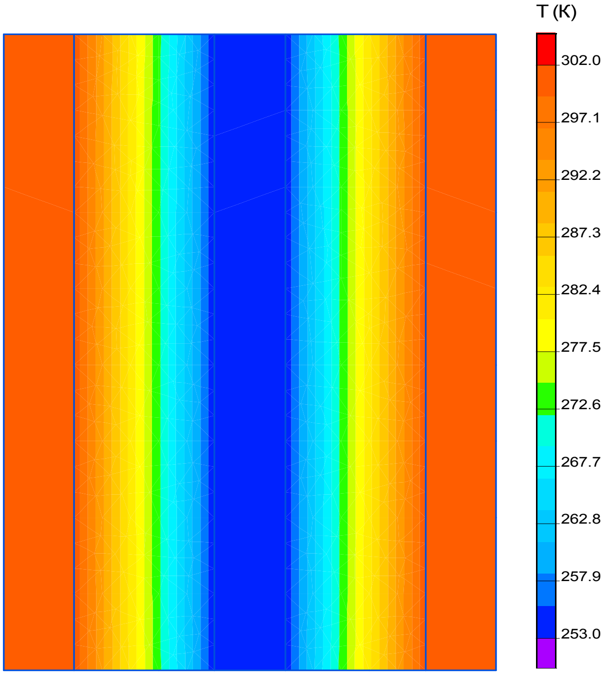

Fig.3. Temperature field of a layer-structured thermoelement.

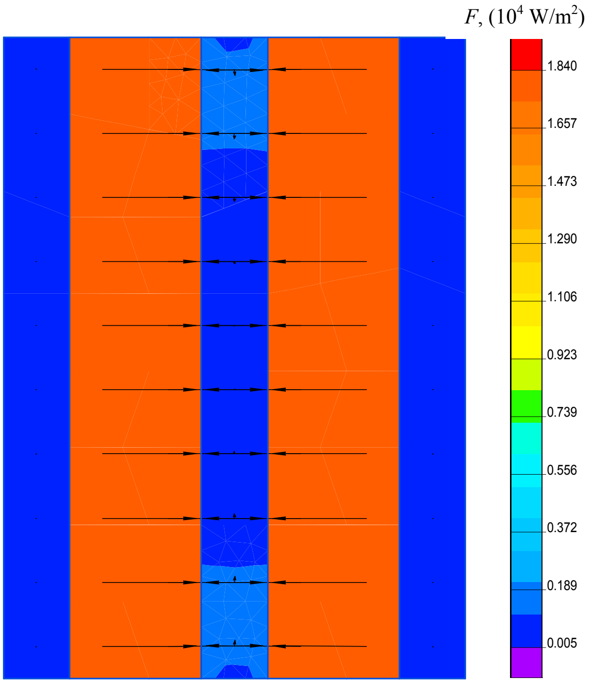

Fig.4. Thermal flow pattern in a layer-structured thermoelement.

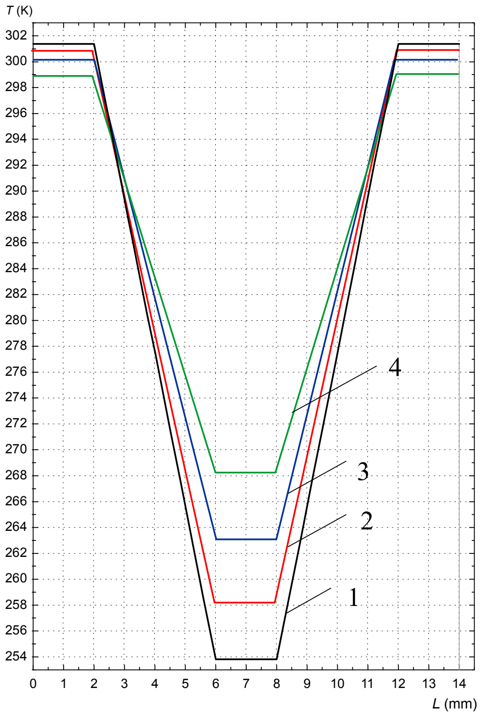

Fig. 5. Temperature distribution along the longitudinal axis of a layer-structured thermoelement at different supply current values: 1 – 140 A, 2 – 120 A, 3 – 100 A, 4 – 80 A.

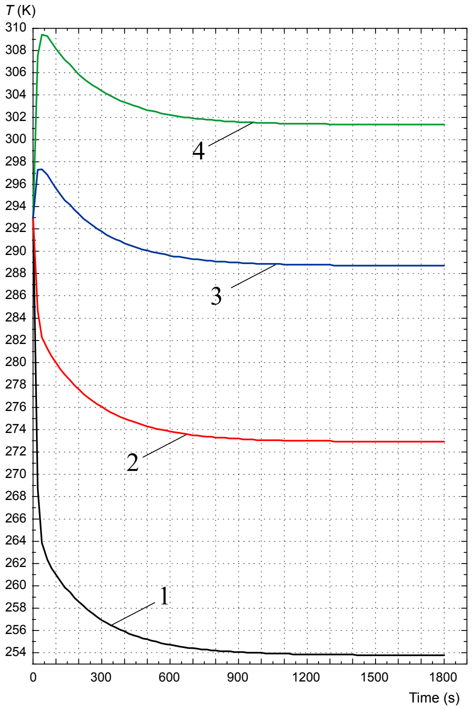

Fig. 6. Temperature variation at different points of a layer-structured thermoelement along the longitudinal axis in time: 1 – cold connecting plate, 2 – thermoelement leg at a distance of 1.5 mm from the cold connecting plate, 3 – thermoelement leg at a distance of 1.5 mm from the hot connecting plate, 4 – hot connecting plate.

Deformation ε_z is determined by means of ε_x and ε_y by the formula

$$\varepsilon_z = \frac{\nu}{\nu - 1}(\varepsilon_y + \varepsilon_y) + \frac{1+\nu}{1-\nu}\gamma T .$$

When solving a plane thermoelasticity problem, the unknown stress values are assumed as σ_x, σ_y and τ_{xy}.

In the state of plane stress one can write

$$\nabla^2\left(\sigma_x + \sigma_y\right) + E\gamma\nabla^2 T = 0 .$$

Partial solution of thermoelasticity problem is given by:

$$\sigma_x^{(T)} = -2G\frac{\partial^2\Phi}{\partial y^2},\ \sigma_y^{(T)} = -2G\frac{\partial^2\Phi}{\partial x^2},\ \tau_{xy}^{(T)} = 2G\frac{\partial^2\Phi}{\partial x\partial y}, \tag{3}$$

$$G = \frac{E}{2(1+\nu)} .$$

For the state of plane stress we have

$$\nabla^2\Phi = \left(1+\nu\right)\alpha T , \tag{4}$$

where Φ is thermoelastic dislocation potential.

For the steady-state temperature fields:

$$\nabla^2 T = \frac{\partial^2 T}{\partial x^2} + \frac{\partial^2 T}{\partial y^2} = 0 ,$$

therefore, application of operator ∇^2 to Eq. (4) can yield

$$\nabla^2\nabla^2\Phi = \frac{\partial^4\Phi}{\partial \mathrm{x}^4} + 2\frac{\partial^4\Phi}{\partial \mathrm{x}^2\partial y^2} + \frac{\partial^4\Phi}{\partial y^4} = 0 . \tag{5}$$

Thus, if thermoelastic dislocation potential is found from Eq. (5), then stresses are found by simple differentiation in conformity with formula (3).

Due to the fact that elastic dislocation potential gives only partial solution, stresses (3) obtained with its help in the general case will not satisfy homogeneous boundary conditions.

Therefore, to free the boundary from the external effects, one must apply such a solution of elasticity theory equations which on the body surface will give stresses equal in value and opposite in sign to those that follow from Eq.(3).

Solution of this problem can be found through the Airy stress function by the formulae:

$$\sigma_x^{(P)} = \frac{\partial^2\varphi}{\partial y^2},\ \sigma_y^{(P)} = \frac{\partial^2\varphi}{\partial x^2},\ \tau_{xy}^{(P)} = -\frac{\partial^2\varphi}{\partial x\partial y}, \tag{6}$$

where φ is a biharmonic function.

The final solution of thermoelastic problem can be obtained by summation of Eqs. (3) and (6):

$$\sigma_x = \sigma_x^{(T)} + \sigma_x^{(P)} = \frac{\partial^2\left(\varphi - 2G\Phi\right)}{\partial y^2},$$

$$\sigma_y = \sigma_y^{(T)} + \sigma_y^{(P)} = \frac{\partial^2\left(\varphi - 2G\Phi\right)}{\partial x^2},$$

$$\tau_{xy} = \tau_{xy}^{(T)} + \tau_{xy}^{(P)} = \frac{\partial^2\left(2G\Phi - \varphi\right)}{\partial x\partial y}.$$

Introducing the Airy stress function related to stresses σ_x, σ_y, τ_{xy} by formulae similar to (6), and substituting them to (5) we obtain

$$\nabla^2\nabla^2\varphi + E\alpha\nabla^2 T = 0 .$$

The general solution of this equation can be represented as

$$\varphi = \varphi^{(P)} + \varphi^{(T)} ,$$

where $\varphi^{(P)}$ is a general solution of the biharmonic equation

$$\nabla^2\nabla^2\varphi^{(P)} = 0 ,$$

and $\varphi^{(T)}$ is a partial solution of equation

$$\nabla^2\varphi^{(T)} + E\alpha\nabla^2 T = 0 .$$

Solution of thermal elasticity equations together with the boundary conditions defining the presence on all system faces of zero normal pressure, temperature distribution found when solving Eqs. (1)-(2), yields a two-dimensional pattern of mechanical stresses, deformations and dislocations.

The results of calculations are given in Figs. 7-8. The calculations were performed with the following initial data: $E = 1.2{\cdot}10^6$ N/m^2, $\nu = 0.3$ $\gamma = 22.2{\cdot}10^{-6}$ 1/K for thermoelectric material and $E = 1.2{\cdot}10^{11}$ N/m^2, $\nu = 0.34$ $\gamma = 16.8{\cdot}10^{-6}$ 1/K for copper connecting plates [15]. The ultimate strength of thermoelectric material is $1.0{\cdot}10^7$ N/m^2, of connecting plates – $3.2{\cdot}10^8$ N/m^2.

Fig. 7 shows a two-dimensional field of mechanical stresses for a layer-structured thermoelement with supply current 120 A, which corresponds to thermal flux value 16000 W/m^2.

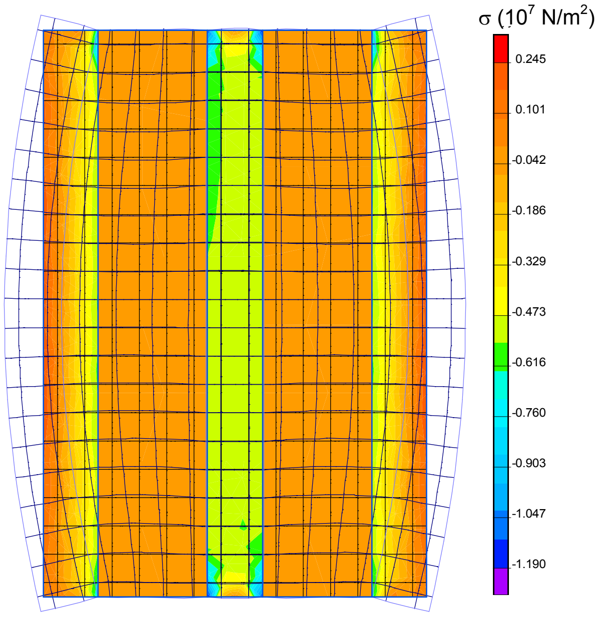

Fig. 7. Mechanical stress pattern in a layer-structured thermoelement.

From the foregoing data it follows that for the above thermoelement design the value of mechanical stresses does not go beyond the permissible values. Maximum load falls on points of contact between connecting plates and thermoelement legs. Here, mechanical load reaches the value of $0.9{\cdot}10^7$ N/m^2 for connecting plate. The greatest mechanical stresses in thermoelectric material do not exceed $0.2{\cdot}10^7$ N/m^2. Fig. 7 also depicts a deformed thermoelement boundary. As it appears from the figure, in the case of a layered thermoelement structure, the deformations are relatively small and are primarily due to elongation and extension of thermoelement on the sides, which is due to the absence of its rigid fixation along the edges. In so doing, maximum dislocation value according to calculated data does not exceed 0.18 mm.

For comparison, Fig. 8 shows a pattern of mechanical stresses under the same conditions for a classical flat-topped thermoelement. In this case deformations are rather large, and with a supply current of 120 A, without the use of special measures for reduction of thermomechanical loads, the mechanical loads exceed the respective ultimate strength of material.

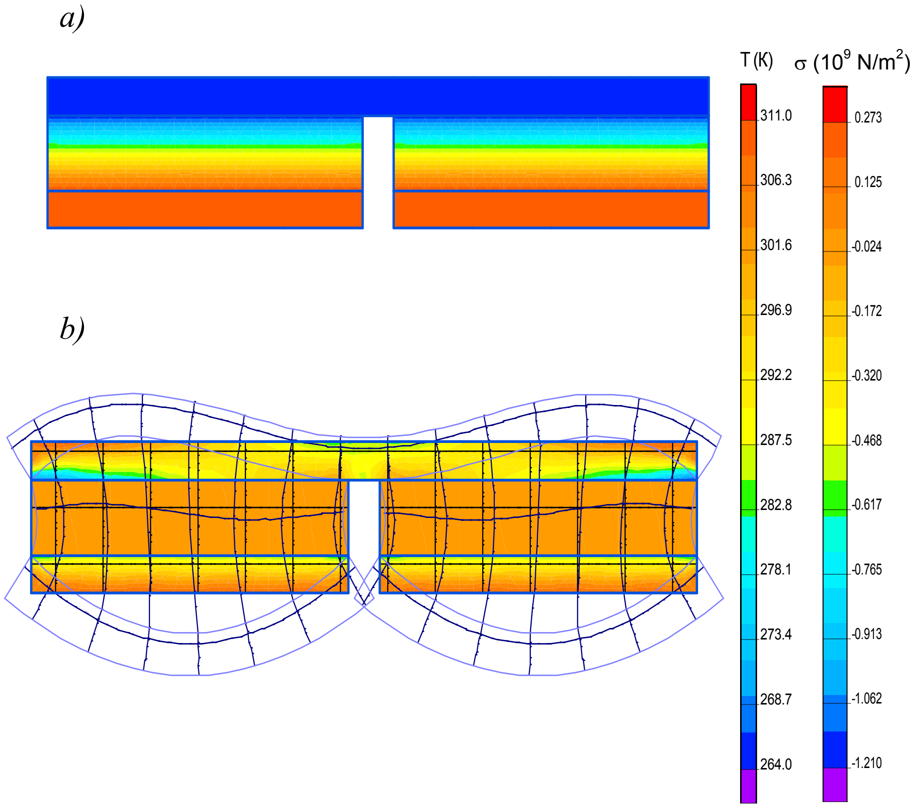

Fig. 8. Temperature field (a) and mechanical stress field (b) of a classical flat-topped thermoelement structure.

For instance, for connecting plates in conjunction with thermoelement leg the value of mechanical stress is above $7\cdot10^8$ N/m^2, which exceeds more than twice the ultimate strength of copper, for thermoelectric material the relation between mechanical loads and ultimate strength in this case is even higher. In so doing, in conformity with the calculations, it was established that for given thermoelement structure the largest supply current without excess of permissible value of mechanical loads in the system is electric current that does not exceed 82 A, i.e. almost a factor of 1.7 lower than in the case of using a layered thermoelement for which maximum supply current as per calculation is 140 A.

Conclusions

On the basis of investigations performed, the following conclusions can be made:

1. In the design of relatively high-power small-size cooling systems based on thermopiles, difficulties emerge in assuring their reliable operation. In this case, when low-current thermopiles are used, the reliability is affected by a large number of thermoelements, and in the case of high-current thermopiles – by the presence of essential thermomechanical stresses.

2. To reduce the value of thermomechanical stresses and deformations in high-current thermopiles, it is advisable to design them in the form of a layered structure where the directions of

electric current and thermal flow coincide.

3. Simulation of a layer-structured thermoelement includes its temperature field calculation and determination of corresponding thermomechanical characteristics. In so doing, temperature field calculation of a layer-structured thermoelement is done on the basis of solving the unsteady-state thermal conductivity equation for a multi-layered system, and determination of mechanical stresses and deformations is done, accordingly, when solving the equilibrium, continuity and Duhamel-Neumann equations by finite element numerical method.

4. The results of theoretical investigations of a layer-structured thermoelement have demonstrated its definite advantages over a classical flat-topped thermoelement as regards thermomechanical characteristics at high supply currents.

References

1. L.I. Anatychuk, *Thermoelectricity. Thermoelectric Power Converters* (Kyiv, Chernivtsi: Institute of Thermoelectricity, 2003).
2. L.I. Anatychuk, Basic Elements of Thermoelectricity, *Proc. of IX Interstate Workshop “Thermoelectrics and Their Applications”* (Saint-Petersburg, 2004).
3. L.I. Anatychuk, On the Physical Models of Thermoelements, *J.Thermoelectricity* **1**, (2003).
4. B.S. Pozdnyakov, E.A. Kokteylev, *Thermoelectric Power Engineering* (Moscow: Atomizdat, 1974).
5. B.E.-Sh. Malkovich, Thermoelectric Modules Based on Bismuth Telluride Alloys, *Proc. of XI Interstate Workshop “Thermoelectrics and Their Applications”* (Saint-Petersburg, 2008).
6. *Patent RF № 2280919*. Thermopile / T.A. Ismailov, M.G. Verdiev, O.V. Yevdulov, 2006.
7. *Patent RF* № 2280920. Thermopi le / T.A. Ismailov, M.G. Verdiev, O.V. Yevdulov, 2006.
8. *Patent RF* № 2280921. Thermopile / T.A. Ismailov, M.G. Verdiev, O.V. Yevdulov, 2006.
9. *Patent RF* № 2270495. Method for Support of Thermopile Operation / T.A. Ismailov, M.G. Verdiev, O.V. Yevdulov, 2006.
10. *Patent RF* №2335036. Thermopile / T.A. Ismailov, M.G. Verdiev, O.V. Yevdulov, D.V. Yevdulov, 2008.
11. *Patent RF* № 2357330. Thermopile / T.A. Ismailov, M.G. Verdiev, O.V. Yevdulov, 2009.
12. *Patent RF* № 2380787. Thermopile / T.A. Ismailov, O.V. Yevdulov, D.V. Yevdulov, 2010.
13. *Patent RF* № 2379790. Thermopile / T.A. Ismailov, O.V. Yevdulov, D.V. Yevdulov, 2010.
14. *Patent RF* № 2417484. Thermopile / T.A. Ismailov, O.V. Yevdulov, D.V. Yevdulov, 2011.
15. A.I.Voronin, A.S.Osilkov, and T.A. Gorbatovskaya, On the Issue of Mechanical Strength of Thermoelement Legs Based on Bi_2Te_3, *Proc. of XI Interstate Workshop “Thermoelectrics and Their Applications”* (Saint-Petersburg, 2008).

Submitted 14.04.2015

B.I. Stadnyk

B.I. Stadnyk, S.P. Yatsyshyn

National University “Lviv Polytechnic”, 79013, 12, Bandera
Street, Lviv, Ukraine

S.P. Yatsyshyn

THERMOMETRIC NOISE AND PERFORMANCE OF THERMOELECTRIC THERMOMETERS

Opportunities of thermoelectric thermometry are considered for the purpose of nanotechnology. Linear dimensions of thermometers have to be commensurable with those of the measured objects. The specific group of phenomena seems to become valid in nanopatterns due to the growing role of surface energy and its gradient. It changes the intensity of thermometric noise and forms the basis for sensor performance and their influence factors that affect measurement precision.

Key words: thermoelectric thermometer, nanotechnology, thermometric performance.

Introduction

Intensive development of microelectronics and nanotechnology involves significant improvement of the energy efficiency of chips which is impossible, first, without further progress in the field of thermoelectric conversion of scattered electrical power; second, without in-situ measuring the temperature of these very chips with the help of embedded sensors. The simplest of them are the thermoelectric sensors. Clearly, the size of the latter must comply with the size of measured objects, for instance wrap-around gate CNTFETs (CNT length ~100 nm and diameter ~ 20 nm) [1].

These measuring instruments of thermoelectric genesis are quite new and their operation in the size limits of nanoelectronics creates a series of problems, the most important of which are: a) the necessity to study the extent to which the concept of "temperature" can be described by common physical, thermodynamic and electrodynamic approaches [2]; b) further development at the nanoscale of thermoelectricity fundamentals and particularly the approach of eddy thermoelectric currents [3]; c) creating a new class of thermoelectric substances with nano distributed spatial heterogeneity [4]; d) establishment of standards of physical units based on the fundamental constants of matter [5]; e) update of thermodynamics towards consideration of surface tension forces and others that has led to the advent of nanothermodynamics [6].

1. Objective of the work

The objective of this work is studying the basic principles of high-precision thermoelectric thermometers development for nanotechnology purposes on the basis of researching influence factors caused by fluctuation-dissipation phenomena in thermometric substance that manifest thermometric noise (in the form of eddy thermoelectric currents).

2. Researches in thermoelectric thermometry: theory and experiment

We have proved the applicability of statistical-thermodynamic approach to the problem of thermo-EMF stability. A new thermodynamic force in the form of mechanical stress gradient $\nabla\sigma$ was considered in [7]. Then involvement of statistical thermodynamics of nonequilibrium processes shows the advisability of a unifying approach in studying the influence functions caused by the complex processes of heat, charge, etc. transfer on the characteristics of thermometric substances of thermoelectric thermometers acting as numerous technological and operational factors, such as perturbation factors. For a prolonged use the thermometric substance is transferred to the thermodynamic state that is close to weakly unstable steady-state one. However, transfer processes in thermometric substance result in the fluctuations of electric genesis (i.e. thermometric noise) arising due to changes in thermodynamic state, thus, in a change of metrological characteristics and, therefore, in raising the instrumental component uncertainty of thermoelectric thermometer.

Specified noise provides the basis for forming a transformation function and its influence factors (Fig. 1). To avoid the correlation effects of different influence factors, which is important for assuring the accuracy in metrology, the metrologically stipulated system of selecting the non-related factors that are thermodynamic quantities is applied [8]. Fluctuation-dissipation theorem, related to reversible and irreversible thermodynamics, could be applied both to nanomaterials and thermosensitive substance. The Nyquist rate, combining the spectral density of energy of electric noises within certain frequency band and electric resistance, is treated as a particular case of this theorem.

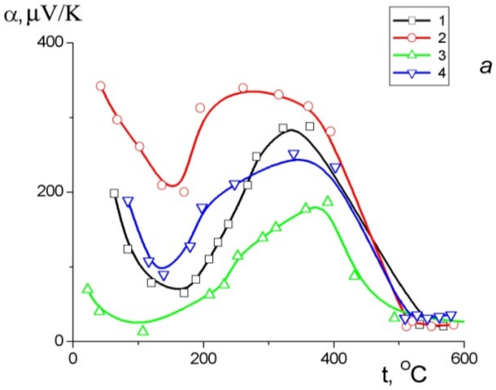

Fig.1. The Seebeck coefficient α of tellurium doped with 1.1% (1) and 1.5% (2) zinc and 1.1% (3) and 1.5% (4) of gallium and their changes at melting (higher 400°C).

Then involvement of statistical thermodynamics of nonequilibrium processes emphasizes the advisability of a unifying approach to studying the influence functions caused by the complex transfer processes as regards the effect on thermoelectric thermometers thermometric substance of numerous technological and operational factors such as perturbation factors. However, in thermometric substance transfer processes the fluctuations of electric genesis (i.e. **thermometric noise**) arising due to changes in thermodynamic state, result in changing the metrological characteristics and therefore in raising the uncertainty of thermoelectric thermometer readings.

Considering the classical electro thermal phenomena in conducting medium, which set the basis for thermoelectric phenomena, we obtain a system of three equations with three unknowns in the presence of electric and heat transfer, and their related mass transfer in thermodynamic system of thermometric substance under consideration. Namely thermopower (or its equivalent value) emerges in a rather long and thin conductor which is located in thermally inhomogeneous medium. Three components of three equations given below that describe the fluxes of heat I_h, charge I_e and mass I_m, are derived:

$$\begin{cases} I_e = -L_{11}\nabla\varphi - \dfrac{L_{12}}{T}\nabla T - L_{13}\nabla\left(\dfrac{\mu}{T}\right) \\ I_h = -L_{21}\nabla\varphi - \dfrac{L_{22}}{T}\nabla T - L_{23}\nabla\left(\dfrac{\mu}{T}\right), \\ I_m = -L_{31}\nabla\varphi - \dfrac{L_{32}}{T}\nabla T - L_{33}\nabla\left(\dfrac{\mu}{T}\right) \end{cases} \qquad (1)$$

where thermal diffusion is described by coefficients $L_{23} = L_{32}$. Coefficients $L_{13} = L_{31}$ concern the electro diffusion that is absent at measuring thermopower with the help of compensating method when $I_e = 0$. Electrical transfer applies when it is necessary to minimize the error of thermoelectric thermometers, for example in nuclear power plants where essentially the possibility of their metrological verification is impossible. In general, the solution of electrical flux transfer equation of thermometer is obtained as transformation function:

$$I_e = k_1\left[e^2 E_l - eT\nabla\left(\frac{\mu}{T}\right)\right] - \frac{e}{T}k_2\nabla T = 0 \tag{2}$$

Here $k_1;k_2;k_3$ are the kinetic coefficients. With the obtained intensity of electric field along thermoelectrodes the intensity of electric field E_l:

$$E_l = \frac{k_2 - k_1\mu}{ek_1T}\nabla T + \frac{1}{e}\nabla\mu = \alpha\nabla T + \frac{1}{e}\nabla\mu, \tag{3}$$

is integrated over the length of electrodes, hence of a thermocouple located in the temperature gradient area. We obtain thermopower or in a wide temperature range the transformation function of thermoelectric thermometer:

$$U(T,...) = U(T) + \Delta U\left[T(x);\mu(x)\right] = \int_x \alpha\left[T(x)\right]\nabla_x T dx + \frac{1}{e}\int_x \nabla_x\mu\left[T(x)\right]dx. \tag{4}$$

Here α is the Seebeck coefficient; 1st summand determines the transformation function; 2nd summand defines the influence function. In this case, thermoelectrodes are considered to be heterogeneous, and there may be a gradient of chemical potential ($\nabla\mu = 0$) along their length. Radially heterogeneous medium is successfully simulated [10] by parallel connected conductors of different materials. The studies explain the reasons for the appearance and mechanisms of occurrence of thermoelectric effects in thermoelectric materials with smoothly distributed properties. Thus, the equivalent thermopower U_E of a multifilament wire drawn up by different wires of particular thermopower U_i and electrical conductivity γ_i is computed as:

$$U_{\sum} = \frac{\sum_i U_i\gamma_i}{\sum_i \gamma_i}. \tag{5}$$

A similar formula is obtained [11] by using thermodynamic foundations. In that case various temperature dependences of conductivity can be considered.

Functionally graded thermocouples are realized on the basis of thermoelectric materials with smoothly distributed properties (or with the gradient of chemical potential along the electrodes) [12]. It is due to imposing the temperatures drop on the latter during the thermoelectric thermometers operation. As a result, the transformation function becomes more precise, just as the thermoelectric thermometer readings.

It can be shown that other thermodynamic fluxes excluding the above mentioned heat, charge and mass fluxes, are especially significant in micro- and nano-volumes. These are exactly the mechanical flux connected with volume gradient (∇V) and the flux caused by the available surface area gradient of nanosamples (∇M), which give rise to amendments in equations (1):

$$E_l == \alpha\nabla T + \frac{1}{e}\nabla\mu + c\nabla V + d\nabla M \tag{6}$$

changing by integration the integral thermopower to:

$$\begin{gathered}U(T,...)=U(T)+\Delta U\left[T(x);\mu(x);V(x);M(x)\right]=\\=\int\limits_x \alpha\left[T(x)\right]\nabla_x T dx+\frac{1}{e}\int\limits_x \nabla_x \mu\left[T(x)\right]dx+c\int\limits_x \nabla_x V\left[T(x)\right]dx+d\int\limits_x \nabla_x M\left[T(x)\right]dx.\end{gathered} \tag{7}$$

It should be taken into account that "mechanical" thermodynamic flux is the flux generated due to mechanical stress gradient along the *X*-axis of thermoelectrode. This one-dimensional task ignores the possibility of thermodynamic forces and fluxes action in other two coordinates, in contrast to [9].

3. Nanothermometry features

3.1. Nanothermocouples

Nanotechnology requires temperature measurement and control of very small volumes of material with the microsecond time response. Such measurement instruments seem to be thin-film thermocouples. Unfortunately, they do not offer a reasonable level of performance reproducibility.

In reality, these metrological characteristics do not exceed millisecond value with the smallest sizes of the available thermoelectric thermometers. The latter can be considered to be thin-film thermocouples with the Seebeck coefficient proportional to the thickness of films; with the thickness of 100 nm the sensors response time makes about 1 μs. Known are [10] also electrodeposited thermocouples in the form of silver-nickel nanowires as electrodes with sufficiently linear performance within the range of 20-100 °C. Unfortunately, these sensors are not produced yet with proper reproducibility, interchangeability etc.

The reasons could consist in technological peculiarities that cause the differences between thermocouples in certain lots and between thermocouples within the lots; they change their characteristics over time. We have studied the effect of thermo structural mechanical stress on thermoelectric output and, hence, on thermocouple readings. When studying the impact of thermal shocks there were observed deviations from equilibrium values (Fig.2). The latter increased with a rise in temperature jump ΔT. This process became more intensive when the jump was done in two phases (ΔT = 600 + 600 K). These changes can be related to the emergence and relaxation of mechanical stresses that correlate with thermopower drift and occur in the neighborhood of defects.

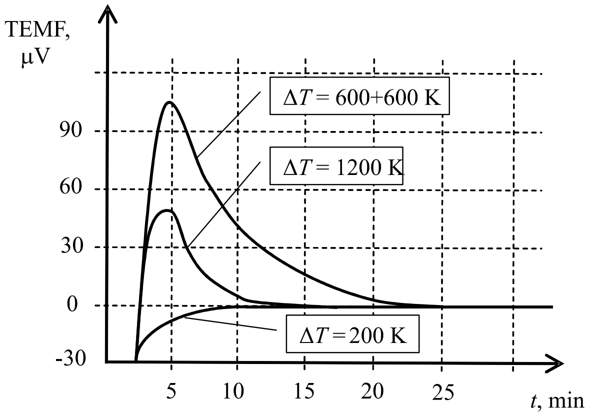

Fig. 2. Effect of thermal shocks demonstrated according to readings of two differentially connected thermocouples at different values of temperature drop ΔT.

Currently, the structures of FET CNT type are of particular interest for thermoelectric phenomena research due to their nanodimensions as well as to the presence of two junctions (inlet wire –source; outlet wire - drain) that are in immediate vicinity to each other, that is, the points where the heat could be released or absorbed.

3.2. Liquid-in-nanotube and solid-in-nanotube thermometers of volumetric expansion

Examination [11] showed that surface and bulk transfer processes together form the calibration characteristics of liquid-in-glass thermometer. Moreover, intensity ratio of these processes cardinally changes with thermometer dimensions reduction down to nanosizes. Eventually, it changes to the opposite flux responsible for formation of thermometer influence function.

Thus, in the considered case we deal with the thermodynamic forces that correspond to mechanical, surface and heat freedom degrees and define the system of transfer equations for thermosensitive substance:

$$\begin{cases} I_m = -L_{11}\nabla V - L_{12}\nabla M - L_{13}\nabla T \\ I_n = -L_{21}\nabla V - L_{22}\nabla M - L_{23}\nabla T \\ I_T = -L_{31}\nabla V - L_{32}\nabla M - L_{33}\nabla T \end{cases}. \tag{8}$$

Here, $I_e; I_h; I_m$ are the transfer fluxes caused by electrical charges, surface tension and heat transfer, respectively; L_{ij} are the transfer coefficients. Equations of calibration characteristics of mentioned thermometers for macroworld and micro(nano)world are derived below from this system.

In the macroworld it is deemed necessary to minimize an error caused by surface tension and the temperature gradient. The latter is negligibly small (I_T=0) because liquid-in-glass thermometers measure the temperature at small space temperature gradient. Then system (8) is reduced to:

$$\begin{cases} I_m = -L_{11}\nabla V - L_{12}\nabla M \\ I_n = -L_{21}\nabla V - L_{22}\nabla M \end{cases}. \tag{9}$$

The 1st equation concerns the flux of displacement of thermosensitive liquid column under the action of forces caused by the gradients of volume and surface area. The 2nd equation concerns the surface tension force gradient leading to decrease/increase of column height under the action of said thermodynamic forces. In so doing, the force caused by surface effects becomes important on drawing near to nanosize and becomes determinative in nanoworld. So, in case of liquid-in-nanotube thermometer we deal with displacement of column due to a change in surface tension forces caused by temperature change The effect of mechanical freedom degree becomes responsible for the deviations from the nominal calibration characteristics, which determines measurement error of nanothermometer.

In other words, consideration of a liquid-in-glass thermometer in macroworld with neglect of surface tension forces could bring us to interrelation of liquid volume ΔV and controlled temperature changes:

$$\Delta V = V_0 \alpha_V \Delta T. \tag{10}$$

Here, V_0 is the initial liquid volume; α_V is the coefficient of thermal expansion of liquid. With a spherical container of diameter D for liquid it gives the possibility to estimate changes in the column height Δh (diameter d) of a thermometer as a function of temperature ΔT by the proportionality (when α_V = 10^{-4} 1/K and $D = 10d$) describing the equation of thermometer calibration characteristic:

$$\Delta h = 0.067 d \Delta T = A\Delta T, \text{ mm}. \tag{11}$$

Indeed, thermometer sensitivity is reduced with a decrease in thermometer tube diameter. The temperature dependence of surface tension forces could be depicted for all liquids, so that the data are placed along one common curve. If V is the molar volume and T_c is the critical liquid temperature, then surface tension coefficient σ is defined as:

$$\sigma V^{2/3}=k\left(T_c-6-T\right). \tag{12}$$

Here, k is a constant for all liquids (Eötvös constant makes 2.1×10^{-7} Joule/K mole$^{-2/3}$). Then, equation of calibration characteristic of a liquid-in-nanotube thermometer takes on the form:

$$\Delta h=\frac{4k'}{\gamma d}\left(\frac{N_A}{V}\right)^{2/3}\left(T_c-6-T\right)=C\left(T_c-6-T\right), \tag{13}$$

where C is a constant.

3.3. Resistance thermometers made of nanostructured thermosensitive substance

Metal glasses (MG) with an amorphous structure are subject to investigations as novel materials with a high resistivity ρ and a small value of temperature coefficient α. The particular efforts are made in the endeavour to bind the electrical MG properties with the peculiarities of their manufacturing technology which could be beneficial in the manufacture of special electrotechnical materials, spintronics etc. The study of nanostructured materials confirms the existence of fields of considerable mechanical microstresses whose influence is equal to doping with admixtures. In the approximation of a MG model, i.e., assuming that there are precipitations of other phases in a matrix, e.g. pseudo-phases which could be represented by the microvolumes of different densities, to obtain experimental results, we have considered the equation of the third order for the resistivity of two-phase material: $\rho_a\left(\Delta\rho\right)^2=\left(1-q\right)\rho_1\left(\Delta\rho\right)^2+\left(\Delta\rho\right)^3-q\rho_1^2$. Here, $q=\Delta S/S$ is the effective intersection area of precipitations, $\rho_1=a+bT$ is the resistivity of a matrix, $\Delta\rho$ is the change of the specific electrical resistance due to precipitations. Explanation roots in the dependence of the specific volume on the speed of chilling, determined in connection with the above temperature. The increment in the MG volume reaches several percent and has a considerable impact on transmission processes with a rise in temperature.

3.4. Ultrasonic thermometers with a sensitive element made of nanostructured thermosensitive substance

Such thermometer could be applied to measuring ultrahigh temperatures with a minimal methodical error component. To provide the stability of thermometer transformation function, we should consider process peculiarities, particularly electron-phonon interaction with tensile defects, occurring in thermometric substance. The porous thermometric materials of real, lower than ideal, density are characterized by smaller changes of thermometer transformation function as compared to ideally dense materials due to deformation influence. Relaxation of the above-mentioned stresses with time acquires a form of resilient plastic structural shifting, diffusive micropores drifting (potassium mechanism) or initiates other phases as in the case of silicium and aluminium oxides that also could encourage the renewal of a transformation function [12].

3.5. Noise thermometers

Thermometric noise can be studied most efficiently with the aid of this kind of thermometers, since their calibration characteristics are calibrated in noise power unit; these thermometers are intended for measurement and have been specially calibrated for this purpose as measuring instruments. Thus, at rapid heating of noise thermometers we have recorded the noise transition process caused by thermodynamic disequilibrium in the sensitive element. It is due to internal changes of defects density in thermosensitive material. As result of imposition of uneven temperature gradient on the thermometer, the changes in calibration characteristics increase (Fig.3).

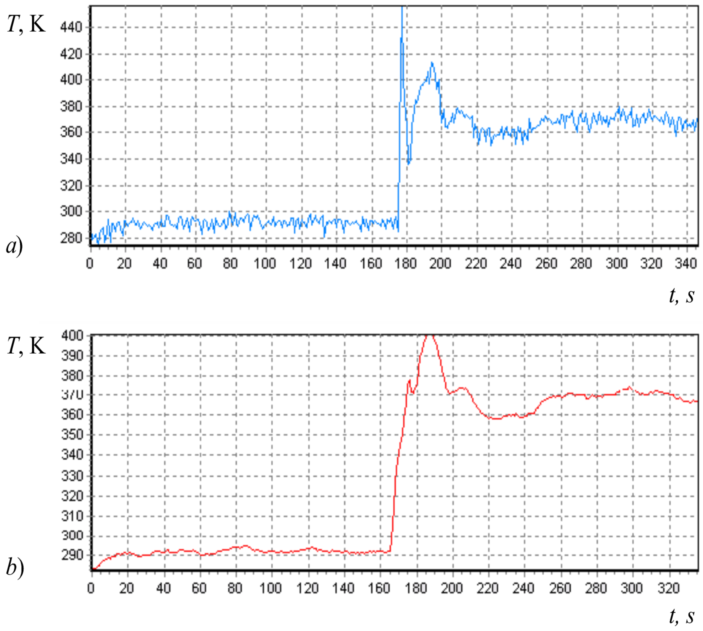

Fig. 3. Process of changing the readings of noise thermometer due to temperature jump from 288 K to 368 K (frequency band of noise signal: 10 - 110 kHz, time of averaging: a) 1s.; b) 10s.

Investigation of noise signal behavior is conducted in dynamic temperature mode by the method of rapid transfer of sensitive element from one medium to another of higher temperature (Fig.3). At the instant of 170th second from measurement beginning, the temperature varies abruptly (from 288 K to 368 K). The recorded temperature defined by noise power exceeds the temperature of gauged medium almost twice.

4. New formalism of nanothermodynamics and peculiarities of thermometer operation

4.1. Fundamental approaches, appropriate for extension of thermodynamics to nanolevel

Up to date, two fundamental approaches are known for extension of thermodynamics to nanoscale; they are based on the microscopic and macroscopic viewpoints, respectively. The first one would refer to the fundamental theorem of macroscopic thermodynamics and establish the new formalism of nanothermodynamics by introducing a new function(s) presenting the fluctuations or reflecting the surface effects in nanopatterns. Another one could directly modify the equations of the macroscopic thermodynamics and establish a new model of thermodynamics on nanoscale by introducing after the Laplace–Young equation additional pressure $\Delta P = \sigma\left(\frac{1}{R_x}+\frac{1}{R_y}\right)$, where $R_x; R_y$ are 2 local radii of surface curvature, or the Gibbs–Thomson relation concerning the fluctuation density of nanosystems in the corresponding thermodynamic expressions [7]. We used both approaches to address the behavior and metrological characteristics of thermosensitive elements made of nanoscaled and nanostructured substances.

4.2. Additional freedom degrees of the fundamental equation of thermodynamics

In order to explain MG electro kinetic and some other defining properties, the nanothermodynamics [7] involves introduction of two additional freedom degrees in the fundamental equation of thermodynamics (Fig.4).

They are: σdM (M is the surface area), caused by the surface tension σ, and □dV (V is the volume of 2nd phase precipitations), caused by the expenses of the specific energy □ for the formation of these precipitations in the matrix of original substance.

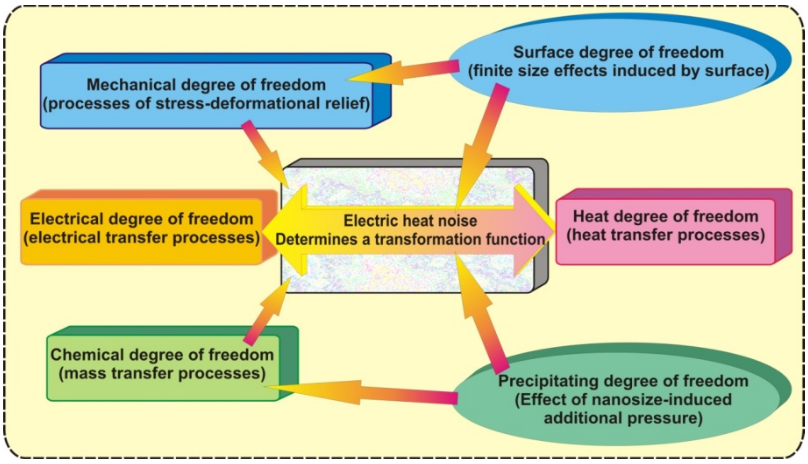

Fig.4. Formation of different noise types and transformation functions of (nano) thermometers in relation to appropriate freedom degrees of the fundamental equation of nanothermodynamics.

We try to consider the influence of the latter by the example of polycrystalline structure of barium-strontium ferrite studies conducted in [16]. Contact overcooling of thin layer occurs at the final stage of pressed powder sintering due to grains interaction through this very layer being in liquid state. Contact temperature difference (up to ten kelvins) for a number of material compositions decreases rapidly with increasing the size of crystallites. The same applies to considerable temperature (tens of kelvins per cm) gradient and, hence, concentration gradient. At the grain size more than 6 µm contact temperature difference becomes negligible.

Using this approach, a vast field of various influence factors producing effect on the thermometric substance, hence on thermometer transformation function, can be reduced to a small number of independent factors, whose effect on the specified function is uncorrelated. Thus, the accuracy of thermoelectric thermometers is considerably increased, which is of minor importance for thermoelectric energy sources.

In the linear thermodynamics, when the system is not too distant from equilibrium, thermodynamic forces X and fluxes J are bound by the Onsager reciprocity relation: $J_i = \sum_j \beta_{ij} X_j .....(i; j = 1...l)$, where $\beta_{ij} = \beta_{ji} ....(i, j = 1...l)$ received with expansion of the complex function $J = J(X_1; X_2; ...X_6)$ in a Taylor series:

$$J_I(X_1,..,X_6) = J_I(0) + \sum_J \left.\frac{\partial J_I}{\partial X_J}\right|_{(0)} (X_J - 0) + \sum_j \sum_n \left.\frac{\partial^2 J_I}{\partial X_j \partial X_n}\right|_{(0)} (X_J - 0)(X_n - 0) + ... \,. \quad (14)$$

The sources due to the influence of thermodynamic forces and fluxes for thermosensitive substance of thermoelectric thermometers are considered and analyzed below while reducing their linear sizes to micro- and nano-sizes. The processes of electric, thermal and partly mass transfer form the thermoelectric thermometer transformation function, and other transfer processes are responsible for forming the influence functions. So, for these thermometers the transformation function

$F\left(T,p,...\right)$, that is defined by three thermodynamic forces (electrical, chemical, heat) and caused by the effect of other thermodynamic forces on total influence function $F_I\left(T,p,...\right)$, are represented in connection with a normalized value of transformation function $F\left(T,0,0,...\right)$:

$$\begin{gathered}F\left(T,p,...\right)=F\left(T,0,0,...\right)+F_I\left(T,p,...\right),\\ \text{where}\quad F_I\left(T,p,...\right)=\sum_{I=3...6}F_I\left(X_I\right),\\ F\left(T,p,...\right)=F\left(T,0,0,...\right)\left[1+\frac{F_I\left(T,p,...\right)}{F\left(T,0,0,...\right)}\right]=F\left(T,0,0,...\right)\left[1+K_\Sigma\left(T,p,...\right)\right].\end{gathered}\tag{15}$$

Here $K_\Sigma\left(T,p,...\right)=K_X+K_M+...$ is the relative total influence function due to complex action of mass transfer K_X, deformation K_M etc.

4.3. Coherence effect as extra mechanism of eddy currents emergence in nanomaterials

In the classical theory of heat conductivity it is considered that the only reason for heat flux in solids is the temperature gradient different from the zero. However, the thermal deformation of the body, in the case of a significant rate of heat flux, results in the so-called coherence effect. It consists in the interaction of deformation and temperature fields. This is already a ground for a transition to the thermodynamics of nonequilibrium processes and even to thermodynamics of nonlinear processes. Numerical evaluation of the impact of the specified effect was performed on the glass and steel samples characterized by about the same thermal diffusivity *a*. Glasses and ceramics are characterized by large values of coherence parameters $\varepsilon'/a_T T' << 400$; whereas the similar parameter of steel is far less and makes 20. This means the following. For ceramics and nanostructured materials the assessment of temperature field effect necessitates a solution of related linear dynamic thermo elasticity problem. Especially it concerns ceramics, where small changes in temperature over time lead to significant deformation impacts.

5. Further development of fundamental principles of eddy currents formation in the absence of temperature gradient imposed on material

One of the real cases of any thermoelectric material application is the absence of marked temperature gradient imposed thereon. Then, the conception of eddy currents can work properly, because according to the fluctuation-dissipation principles of thermodynamic parameters fluctuation, including temperature, they still exist in this substance. Such fluctuations are inevitably manifested by eddy thermoelectric currents. The latter results in the appearance on sample surface of charge fluctuations that can be identified by the method of passive noise spectroscopy [13]. As an example, let us give the results of electrical fluctuations/noise studies as compared with the thermoelectric phenomenology research.

Transfer processes are significantly complicated with a considerable rate of temperature change. For instance, thermoelectric substance is annealed at one temperature and rapidly is moved to a medium with a higher temperature, where due to the formation of dislocation ensembles the mechanical stresses arise that are capable of accumulating the internal energy. Their length can be significantly larger than the lattice constant. In a dynamic temperature mode the availability of structural defects can lead to changes in characteristics of noise. Noise phenomenology is clearly explained by involving the mechanism of energy accumulation-dissipation on local tensile quasi defects of vacancy origin at their interaction with phonons. With or without current flow, phonons are generated in thermosensitive substance; they are accumulated in quasi defects and then are relaxed in reversible or irreversible manner, causing respectively *1/f* or thermal noise.

The Raman method gives opportunity of electron-phonon interaction study. The wave number of optical phonon of the Stokes component is strongly dependent on temperature. For example, for silicon monocrystal this dependence in the temperature range 300...400 K is linear: $\nu_0\left(cm^{-1}\right)=0{,}025\Delta T$, where ΔT is a change in monocrystal temperature [14]. It enables to obtain more precise temperature readout at known temperature dependence of the Raman shift ν_0. With a rise in temperature, the wavelength of scattered light approaches the wavelength of the laser. It is caused by the elimination of tensile micro stresses acting in studied substance due to increased mobility of defects, especially vacancies.

While capturing the phonons by a tensile defect, its local temperature is rising. Considerable thermo-extension takes place, which at some moment could cause the rapture of inter-atomic bonds and thus microcrack emergence. By using the intensity of the Stokes and anti-Stokes bands in the Raman spectrum, the phonon value *n* was defined and their capture by tensile defects was ascertained. Local temperature of the above mentioned defects (with linear size till 10 atoms) is determined as $T_d=\dfrac{h\nu}{k\left[\ln\left(n+1\right)-\ln n\right]}$.

It is obvious how important for thermosensitive substance is a rise in temperature of these dots, that is, on these defects. On the other hand, focusing attention on tensile defects as physically elementary nanosized structure subsystems enables to motivate the introduction of thermodynamic values i.e. the application of nanothermodynamics to the objects under study.

It is important to consider such common factor of influence on calibration characteristics as a deformation factor that tends to increase at a combined action of temperature and strains (structural, resilient, ductile or others) in thermosensitive substance during measurement. This factor is manifested in local distortion of temperature of these materials as a result of applying stresses of tensile micro concentrators that are considered as quasi local nanosized defects of thermo-fluctuation origin. These distortions greatly reduce the real durability of thermometric substance due to noise, which at the same time strengthen deviations of thermoelectric thermometer calibration characteristics, degrading its precision.

Conclusions

1. Reducing the sizes and diminishing the thermometric substance dispersion lead to emergence of the influence factors on the thermoelectric thermometer performance that can be considered by nanothermodynamics. In nanoworld, while decreasing dimensions of thermosensitive substance, surface tension forces and forces of second phase precipitations formation become more effective and can lead not only to drift, but also to changing the character of calibration characteristics.
2. Nanothermometry (including the thermoelectric nanothermometry) considers the action of: a) surface tension thermodynamic force; b) thermodynamic force caused by formation of second phase precipitations in the matrix of original substance.
3. By changing the power of foregoing sources, the thermosensitive substance state permanently drifts producing thermometric noise in thermoelectric thermometry or elementary eddy currents in thermoelectric energetics. Control of this charge deviations enables us to produce new quasi-nonequilibrium materials with high-stable calibrating characteristics for thermoelectric

thermometers; to create functionally graded thermocouples that are a bright example of smoothly distributed structures [15]; and to develop new types of unique thermoelectric thermometer on the industrial base of such devices as CNTFETs the linear dimensions of which are less than thermocouple hot-junction sizes (it is possible to measure in-situ FET's temperature regime with the aid of thermoelectricity).

References

1. R.Sahoo, R.Mishra, Simulations of Carbon Nanotube Field Effect Transistors, *Internat. Journ. of Electronic Engineering Research* **1**(2), 117-125 (2009).
2. L.Anatychuk, *Thermoelectric Power Converters*, *Volume 2* (Institute of Thermoelectricity, Kyiv-Chernivtsi, 2003).
3. O.J.Luste, R.V.Kuz', Computer Control of Eddy Thermoelectric Currents, *J. Thermoelectricity* 2, 11-19 (2004).
4. R.G.Cherkez, Theoretical Studies on the Efficiency of Air Conditioner Based on Permeable Thermoelectric Convertor, *Applied Thermal Engineering* 38, 7-13 (2012).
5. B.Stadnyk, S.Yatsyshyn, and H.Fedorchuk, Metrological Array of Cyber-Physical Systems. Part 2: Checked Instrument Based on Quantum Resistance Standard, *Sensors and Transducers* 186(3), 12-17 (2015).
6. H.Hofmann, Advanced Nanomaterials. Course support, *Powder Technology Laboratory, IMX, EPFL*, Version 1, September 2009.
7. S.Yatsyshyn. B.Stadnyk. Ya.Lutsyk, and L.Buniak, *Handbook of Thermometry and Nanothermometry* (IFSA Publishing, 2015).
8. P. Glansdorf, I.Prigogine, *Thermodynamic Theory of Structure, Stability and Fluctuations* (Wiley, New York, 1971).
9. A.Kao, K.Pericleous, The Effect of Secondary Arm Growth of Thermoelectric Magnetohydrodynamics, *Magnetohydrodynamics* 48(2), 361-370 (2012).
10. M.E.Bourg, W.E.van der Veer, A.G.Grüell, R.M.Penner, Electrodeposited Submicron Thermocouples with Microsecond Response Times, *Nano Lett.* **7**(10), 3208–321(2007), DOI: 10.1021/nl071990q, September 18, 2007.
11. S. Yatsyshyn, B. Stadnyk, and Ya.Lutsyk, Research in Nanothermometry. Part 3: Characteristics of the Thermometers with Liquid- and Solid-Phase Sensitive Elements, *Sensors and Transducers* **140** (5), 15-23 (2012).
12. S. Yatsyshyn, B. Stadnyk, and Ya.Lutsyk, Research in Nanothermometry. Part 7: Ultrasonic Thermometer with Nanostructured Thermometric Materials, *Sensors and Transducers* **143**(8), 1-9 (2012).
13. R.Hemant, B.Gijs, Simultaneous Low-Frequency Noise Characterization of Gate and Drain Currents in AlGaN/GaN High Electron Mobility Transistors, *Journ. of Appl. Phys*. **106**, 103712 (2009); http://dx.doi.org/10.1063/1.3259437 (5 pages).
14. A.N.Magunov, *Laser Thermometry of Solids* (Moscow, Physmathlit, 2001) (in Russian).
15. B. Stadnyk, S. Yatsyshyn, P.Skoropad. Analiza Efektywnosci Stosowania w Termometrii Funkcjonalnie-Gradientowych Czujnikow, *Pomiary, Automatyka, Kontrola* 12, 42–45 (2006) (in Polish).

Submitted 24.04.2015

T.A. Ragimova

T.A. Ragimova, O.V. Yevdulov

Federal State Budgetary Educational Institution of
Higher Professional Education "Dagestan State
Technical University", 70, Imam Shamil avenue,
Makhachkala, 367015, Russia

O.V. Yevdulov

INVESTIGATION OF A THERMOELECTRIC SYSTEM FOR LOCAL FREEZING OF LARYNX TISSUES

The paper is concerned with a thermoelectric system for local freezing of larynx tissues. The results of its mathematical simulation and full-scale test of a prototype are presented. Two-dimensional and one-dimensional theoretical and experimental plots of temperature variation at different system points are given.

Key words: larynx, thermoelectric system, thermopile, thermal exposure, temperature field, mathematical model, prototype, experiment.

Introduction

One of the priority areas in medicine is safety and the use of natural treatment methods capable of stimulating biological response of human organism. In this connection, drug-free modalities are of considerable current use. One of the most widespread and efficient natural physical factors in medicine is low-temperature exposure that serves the basis for methods of local hypothermia of individual human organs and tissues. Among them, one should emphasize local cooling and freezing of larynx tissues which is actively used not only for treatment of throat diseases, such as chronic tonsillitis, pharyngitis, but also as an all-purpose immunostimulating drug, recommended for mass adoption in medical institutions of various level.

Current facilities for local cooling of larynx tissues suppose the use of liquid coolant and have the form of metal rods pre-cooled in liquid nitrogen or oxygen, the so-called passive cryoprobes, as well as systems with open and closed circulation of liquid coolant [1-3]. To the above facilities one can refer devices described in [4-6]. The equipment includes a reservoir with liquid nitrogen, heat-insulated pipes for coolant feed and rejection equipped with corresponding valves, operating tip of various shape and gas evacuation system. To improve the efficiency of cryotip defrosting, as well as to expand the potential of cryodestruction method, in [7] use is made of optical fibers attached to laser radiation source and brought with their operating tips to cryotip cold conductor. In [8], replaceable tips are used as a working source of cold which are filled with coolant and arranged in a case fixed in the holder which allows improving the ergonomics of the device and assures the possibility of its operational application in the field. To improve the operating efficiency of the device for local freezing of larynx tissues due to acceleration of coolant circulation and improvement of heat transfer, [9] involves pressure rise unit and additional heat-exchange unit.

The above facilities do not always meet safety requirements due to possible depressurization of compression systems, biological aggressivity of coolants used, delayed operating processes and low accuracy of cooling effect dosing. The use of liquid coolants in such devices complicates to a large extent their design and maintenance, reduces the operating time due to a restricted coolant volume, prevents from reaching the necessary level of thermal exposure control, does not solve the problem of adhesive effect which calls for the presence of additional heating devices. Said disadvantages interfere with a wide adoption of efficient methods of cryotherapeutic effect on larynx tissues in medical practice.

Under these conditions it is advisable to use thermopiles as a function element in a device for cooling larynx tissues. Their use offers a number of definite advantages, namely eliminates liquid coolants owing to which the device becomes independent from centres of production and delivery of cryogenic fluids, provides for unlimited service life, environmental friendliness, noise-free operation; improves the accuracy of dosing and exposure control, supposes arrangement of reverse mode by switching supply current direction.

In so doing, design of thermopile-based cooling system should conform to a number of specific features including mandatory provision of device temperature parameters in conformity with medical procedures corresponding to the existing hygienic standards, high reliability of exposure, precise localization of cold focus, safety, etc.

In this connection, the purpose of the paper is to investigate a thermoelectric system for local cooling and freezing of larynx tissues, to study the processes occurring in it with regard to the influence of target object parameters and thermopile characteristics.

Mathematical simulation of a thermoelectric system for local freezing of larynx tissues

A quasi-steady-state mathematical model of a system for local freezing of larynx tissues has been developed. This mathematical model considers a device as a totality of components, namely heat-exchange devices (heat exchanger, thermal bridge, thermopile, heat insulation, and operating tip), assuring temperature reduction of a biological object within the required time to the necessary value.

Fig. 1 shows a design circuit of the system. Here, the first junctions of additional thermopile 1 through operating tip of heat capacity c_{p1} and thermal conduction σ_{p1} are connected to biological tissue of heat capacity c_m and thermal conductivity σ_m, respectively.

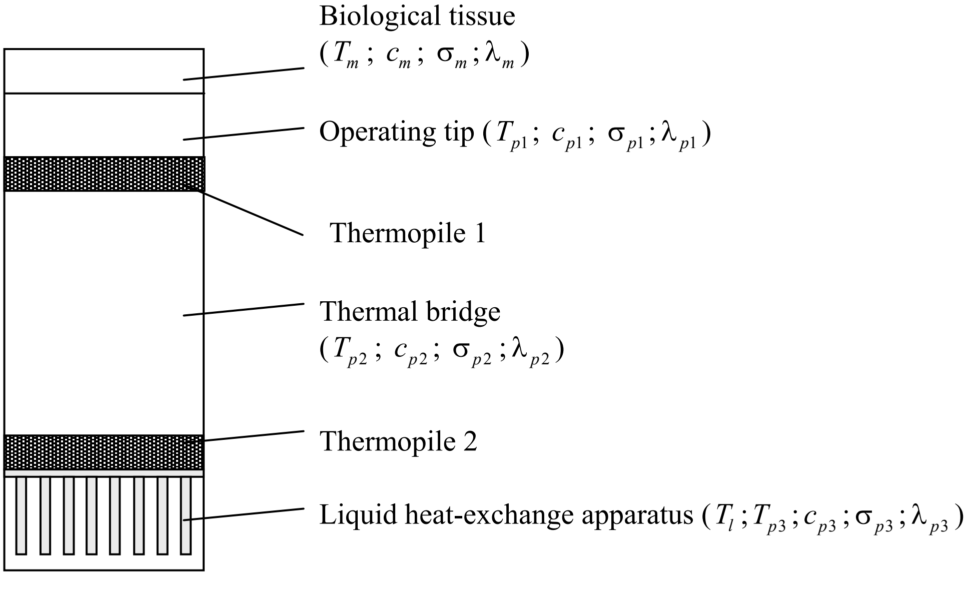

Fig. 1. Design circuit of a system for local freezing of larynx tissues.

The second junctions of thermopile 1 are brought into contact with the end face of thermal bridge of heat capacity c_{p2} and thermal conductivity σ_{p2} whose second end face is connected to the first junctions of the basic thermopile 2.

The second junctions of thermopile 2 by means of a liquid heat exchange apparatus of heat capacity c_{p3} and thermal conductivity σ_{p3} are maintained at temperature T_{p3}. The temperature of liquid flowing in the heat-exchange apparatus is maintained equal to T_l. Current of constant density, j_1 and j_2, respectively, flows through thermopile 1 and thermopile 2. Moreover, biological object under study is characterized by specific power of heat release Q_r.

Under these conditions, mathematical implementation of the model is determined by a system of differential equations:

$$\left.\begin{aligned}
&\frac{dT_m}{d\tau}=\frac{1}{m_m c_m}\left[\sigma_m\left(T_{p1}-T_m\right)+Q_r+\sigma_{amb}\left(T_{amb}-T_m\right)\right]\\
&\frac{dT_{p1}}{d\tau}=\frac{1}{m_{p1}c_{p1}}\left[n_1S_1\left[-e_1j_1T_{p1}+\frac{1}{2}j_1^2\rho_1h_1+\frac{\lambda_1}{h_1}\left(T_{p2}-T_{p1}\right)\right]-\sigma_{amb}\left(T_{amb}-T_{p1}\right)\right]\\
&\frac{dT_{p2}}{d\tau}=\frac{1}{m_{p2}c_{p2}}\left[\begin{aligned}&n_2S_2\left[-e_2j_2T_{p2}+\frac{1}{2}j_2^2\rho_2h_2+\frac{\lambda_2}{h_2}\left(T_{p3}-T_{p2}\right)\right]+\\&+n_1S_1\left[e_1j_1T_{p1}+\frac{1}{2}j_1^2\rho_1h_1+\frac{\lambda_1}{h_1}\left(T_{p2}-T_{p1}\right)\right]-\sigma_{amb}\left(T_{amb}-T_{p1}\right)\end{aligned}\right]\\
&\frac{dT_{p3}}{d\tau}=\frac{1}{m_3c_{p3}}\left[n_2S_2\left[e_2j_2T_{p2}+\frac{1}{2}j_2^2\rho_2h_2-\frac{\lambda_2}{h_2}\left(T_{p3}-T_{p2}\right)\right]-\sigma_{p3}\left(T_{p3}-T_l\right)\right]
\end{aligned}\right\}, \qquad (1)$$

where T_m is the temperature of biological tissue; T_{p1} is the temperature of operating tip having thermal contact with the biological object; T_{p2} is the temperature of thermal bridge; m_m is the average mass of tissue; $m_{p1,p2,p3}$ is the mass of operating tip, thermal bridge and heat exchanger; $e_{1,2}$ is the Seebeck coefficient of thermoelements in thermopile; $\rho_{1,2}$ is the electric resistivity of thermopile; $h_{1,2}$ is the height of thermoelements in thermopile; $\lambda_{1,2}$ is the thermal conductivity of thermopile material; T_{amb} is the ambient temperature, σ_{amb} is coefficient of heat exchange with the ambient.

The initial conditions for the case of evaluation of the time to reach the operating mode by the device are given at no-load operation (no contact of device to biological object), based on the assumption that at the initial time moment the thermoelectric system is in thermodynamic equilibrium with the ambient, and the temperature of all system points is equal to ambient temperature. In so doing, the system of equations (1) is written as:

$$\left.\begin{aligned}
&\frac{dT_{p1}}{d\tau}=\frac{1}{m_{p1}c_{p1}}\left[n_1S_1\left[-e_1j_1T_{p1}+\frac{1}{2}j_1^2\rho_1h_1+\frac{\lambda_1}{h_1}\left(T_{p2}-T_{p1}\right)\right]-\sigma_{amb}\left(T_{amb}-T_{p1}\right)\right]\\
&\frac{dT_{p2}}{d\tau}=\frac{1}{m_{p2}c_{p2}}\left[\begin{aligned}&n_2S_2\left[-e_2j_2T_{p2}+\frac{1}{2}j_2^2\rho_2h_2+\frac{\lambda_2}{h_2}\left(T_{p3}-T_{p2}\right)\right]+\\&+n_1S_1\left[e_1j_1T_{p1}+\frac{1}{2}j_1^2\rho_1h_1+\frac{\lambda_1}{h_1}\left(T_{p2}-T_{p1}\right)\right]-\sigma_{amb}\left(T_{amb}-T_{p1}\right)\end{aligned}\right]\\
&\frac{dT_{p3}}{d\tau}=\frac{1}{m_3c_{p3}}\left[n_2S_2\left[e_2j_2T_{p2}+\frac{1}{2}j_2^2\rho_2h_2-\frac{\lambda_2}{h_2}\left(T_{p3}-T_{p2}\right)\right]-\sigma_{p3}\left(T_{p3}-T_l\right)\right]
\end{aligned}\right\}, \qquad (2)$$

For the case of evaluation of the time of exposure of larynx tissues, the initial conditions are taken from the previously obtained data for the evaluation of the time of reaching the operating mode, and the temperature of target object is 309 K.

It was also assumed that the temperatures of operating tip and heat exchanger are equal to the respective junction temperatures. This assumption increases the time of reaching the operating mode, and the results subsequently obtained will be overrated.

The solution of system (1) and (2) was done numerically in the MATHCAD application program package. In so doing, thermal conductivities were found from the formulae:

$$\sigma_{p1}=\frac{\lambda_{p1}\cdot S_{p1}}{\delta_{p1}},\ \sigma_{p2}=\frac{\lambda_{p2}\cdot S_{p2}}{\delta_{p2}},\ \sigma_{p3}=\frac{\lambda_{p3}\cdot S_{p3}}{\delta_{p3}},\quad \sigma_{m}=\frac{\lambda_{m}\cdot S_{m}}{\delta_{m}}.$$

where λ_{p1}, λ_{p2}, λ_{p3}, λ_m is thermal conductivity of operating tip, thermal bridge, heat exchanger and biological tissue, respectively; $S_{p1,2,3,m}$ is the area of contact surfaces of TE device for freezing of larynx tissues and biological tissue, operating tip and thermopile 1, thermal bridge and thermopile 2, and heat exchanger, respectively; $\delta_{p1},_{p2},_{p3}$, δ_m is the thickness of operating tip, thermal bridge, heat exchanger, and biological tissue, respectively. The numerical values of the initial quantities in expressions (3) were assumed as follows [4]: λ_{p1} = 389 W/m·K; λ_{p2} = 389 W/m·K; λ_{p3} = 389 W/m·K; λ_m = 0.2 W/m·K; S_{p1} = 25·10^{-6} m^2; S_{p2} = 10^{-4} m^2; S_{p3} = 36·10^{-4} m^2; δ_{p1} = 0.01 m; δ_{p2} = 0.13 m; δ_{p3} = 0.02 m; δ_m = 0.01 m.

In order to evaluate the time of reaching the operation mode by the device, as well the time of exposure, the purpose of calculation was to obtain the temperature field of device-target object system as a function of time at ambient temperature T_{amb} = 298 K for the case of no-load system operation (Fig. 2 and Fig. 3) and in the case of influence on larynx tissue (Fig. 4). The time dependences of larynx tissue temperature, operating tip, thermal bridge and liquid heat exchange apparatus at different thermopile supply currents, as well as for different T_l values were obtained.

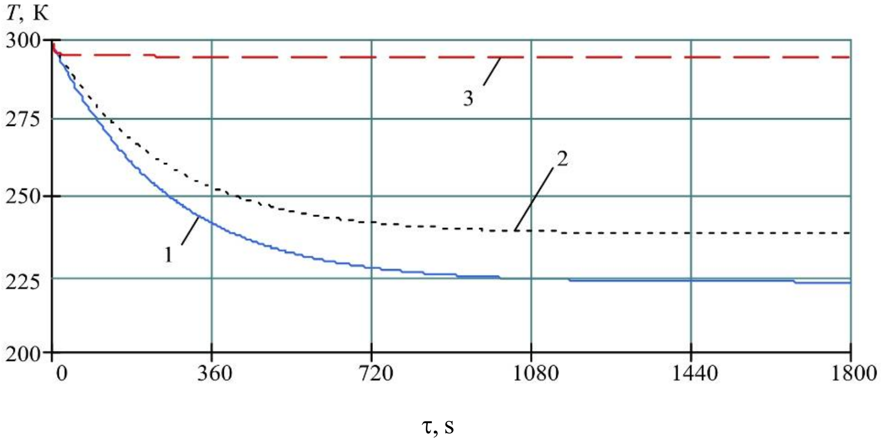

*Fig. 2. Temperature field of TE device as a function of time without thermal load.
1 – temperature of operating tip, 2 – temperature of thermal bridge,
3 – temperature of liquid heat exchange apparatus.*

As it follows from the represented data, the dependences are of a monotonous decreasing nature. According to the above plots, without thermal load the temperature of operating tip is stabilized in about 18-20 minutes (Fig. 2), which corresponds to time necessary to reach its operating mode. Increase in current strength of additional thermopile (Fig. 3) from 0.5 to 1A at supply current of basic thermopile 5 A reduces the temperature of operating tip T_{p1} from 235 K to 220 K.

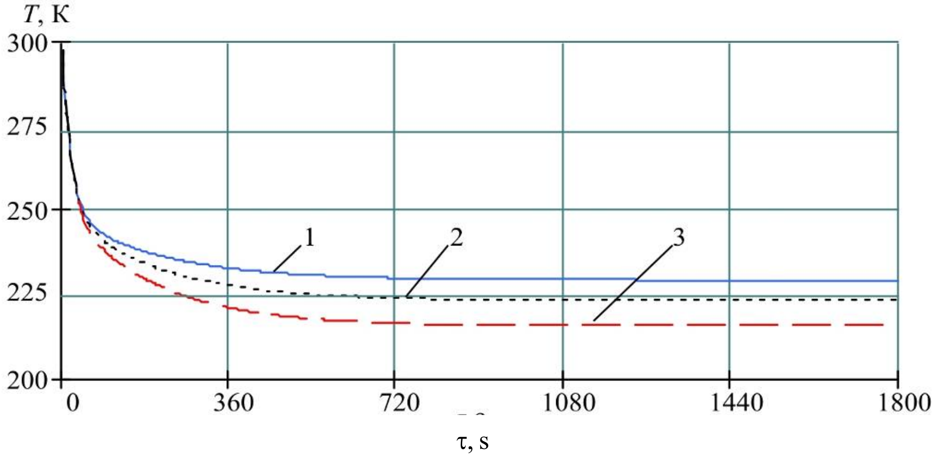

Fig. 3. Temperature variation of operating tip in time under no-load conditions at supply current for basic thermopile 5A and different supply currents for additional thermopile. 1 – 0.5 A, 2 – 0.75 A, 3 – 1 A.

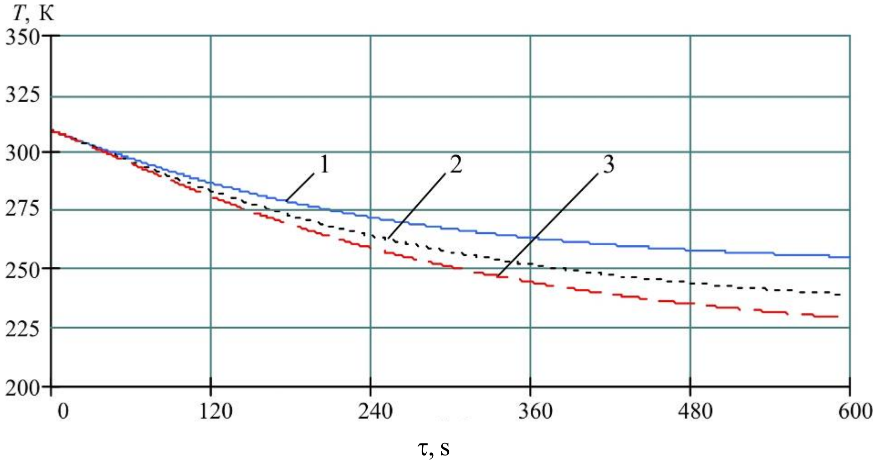

Fig. 4. Temperature variation of larynx tissue in time at different supply currents for basic thermopile. 1 – 2 A, 2 – 3.5 A, 3 – 5 A.

Further increase in current strength results in the Joule heat growth. Therefore, at fixed temperature T_l the ultimate decrease of operating tip temperature is restricted by the value of supply current optimal for this thermopile type. A deeper temperature decrease of operating tip can be obtained by reducing the temperature of liquid T_l, flowing across the heat exchange liquid apparatus. Thus, to reduce tissue temperature, for instance, to 250 K at liquid temperature T_l = 288 K requires 3 minutes less than in the case when T_l = 298 K.

The time to reach the required tissue temperature can be reduced, for instance, to 273 K, by increasing the strength of supply current for additional thermopile. Thus, for the case under study, according to the plots given in Fig. 4, the increase of current strength from 2 to 5 A allows reducing this time from 4 to 2.5 minutes.

Experimental studies of a thermoelectric system for local freezing of larynx tissues

With a view to confirm the results of mathematical simulation, full-scale test of a prototype of thermoelectric system for local freezing of larynx tissues was performed. The object of experimental studies was a prototype of TE device for local freezing of larynx tissues with two and, for comparison, with one TEM. The external view of the system prototype is given in Fig. 5.

Fig. 5. External view of a system for local freezing of larynx tissues.

In the course of the experiment, the prototype was placed into a thermally isolated climatic chamber. The thermopile was powered from electric energy sources Instek PSH – 3630 and GW Laboratory DC Power Supply GPR-1850HD. The load on the operating tip was simulated by a nichrome wire wound on cylinder end. In the course of the experiment, temperature was measured by means of copper-constantan thermocouples whose reference junctions were placed in Dewar flask, and the signal was taken by a multi-channel temperature meter IRTM 2402/M3. Voltage and current on the thermopile were recorded by means of ammeters and voltmeters built into electric energy sources.

During the experiment, voltage and current on the thermopile, ambient temperature and temperatures at different points of the prototype were determined.

In conformity with the value of maximum supply current for the basic thermopile used (5.8 A) and additional thermopile (1.7 A), the work of device was tested for the four values of supply current (3 A; 4 A; 4.5 A and 5.0 A) for the basic thermopile and three values of supply current for additional thermopile (0.5 A; 1 A; 1.5 A).

The main task when performing experimental investigations of the prototype was to determine the time dependence of temperature at check points with fixed values of thermopile supply currents (Fig. 6 and 7).

In conformity with the data in Fig.6, maximum level of temperature decrease when using one basic thermopile is 243 K (–30°C) for maximum current 5 A and is increased by 2 K , 4 K and 10 K for supply currents 4.5 A, 4 A and 3 A, respectively. Based on the resulting data, one can select optimal supply current for given thermopile.

Fig. 7 represents time dependences of tip temperature for different supply currents with the use in the device of the basic and additional thermopiles. The above dependences show that with the use of additional thermopile whose supply current is increased from 0.5 A to 1.5 A, when optimal supply current of the basic thermopile is 5 A, the temperature of the tip is reduced from 233 K to 228 K.

To evaluate temperature variation along the thermal bridge of length 13 cm, the dependences of time variation along the length of the bridge were obtained for different time moments under no-load conditions. According to the results of measurements, maximum temperature difference along the length of the bridge with supply currents for the basic and additional thermopiles 5 A and 1 A, respectively, is 287 K and falls on the initial moment of device switching. When the device reaches the steady-state mode, this difference does not exceed 3 K and points to a relative uniformity of temperature distribution along the length of the thermal bridge. Owing to this fact, in the construction of a mathematical model one can use the averaged temperature of the thermal bridge. In so doing, this simplification will not have a considerable impact on the accuracy of mathematical calculations.

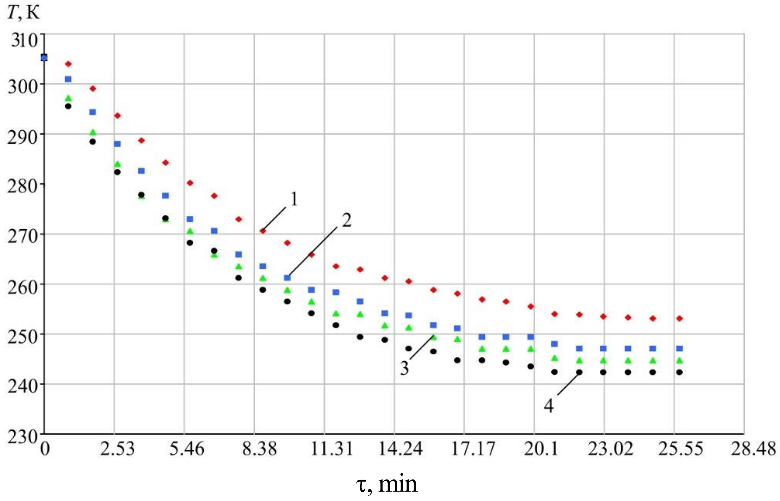

Fig. 6. Time dependence of tip temperature with different supply currents for the basic thermopile, under no-load conditions.

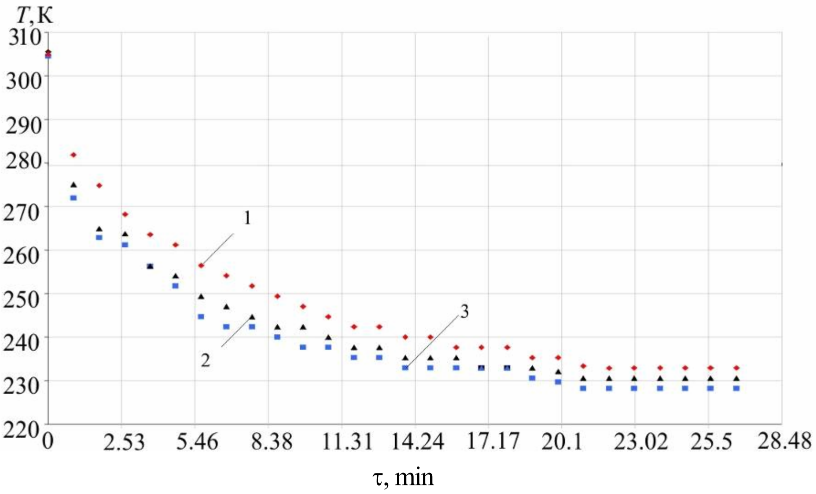

Fig. 7. Time dependence of tip temperature with different supply currents for additional thermopile, under no-load conditions with supply current for basic thermopile 5A.

To evaluate the efficiency of heat rejection system, temperature variation of the basic thermopile hot junction in time was recorded. For the case corresponding to supply currents for the basic and additional thermopiles 5 A and 1 A, respectively, the value of hot junction temperature does not exceed 302 K at cooling liquid temperature 293 K and flow rate 0.07 l/sec.

The resulting experimental data define the acceptable precision of device mathematical model. Maximum discrepancy between the calculated and experimental data does not exceed 11%. The greatest deviation of calculated data from the experiment in the case of determination of the tip temperature is mainly observed in the time interval related to reaching device regime.

Conclusions

On the basis of investigations performed the following conclusions can be made:

1. One of the efficient methods for treatment of ORT diseases, such as chronic tonsillitis, pharyngitis, etc., is local freezing of larynx tissues. This procedure can be implemented due to the use

of thermopiles as a source of cold.

2. A thermoelectric system for local freezing of larynx tissues has been designed that consists of two thermopiles interconnected by all-metal thermal bridge equipped with operating tip and liquid heat exchanger.

3. A quasi-steady-state mathematical model of a thermoelectric system has been developed which considers a device as a totality of components, namely heat-exchange devices (heat exchanger, thermal bridge, thermopile, heat insulation, and operating tip), assuring temperature reduction of a biological object within the required time to the necessary value.

4. It has been established that under no-load conditions the operating tip temperature is stabilized in about 18-20 minutes at supply currents from 1 to 3 A, which corresponds to time necessary to reach its operating mode. In so doing, increase in current strength from 1 to 3 A reduces the operating tip temperature from 275 to 237 K.

5. When carrying out the procedures, the necessary level of larynx tissue temperature reduction (273 K) can be achieved in 4 minutes and 2.5 minutes at supply currents 2 A and 5 A.

6. With a change in current strength from 2 A to 5 A, the ratio between temperature change and current strength change is reduced. With increase in supply current from 2 A to 3 A, the temperature of tissue is reduced from 267 K to 250 K, the increase in current strength from 3 A to 4 A reduces the temperature from 250 K to 240 K, and the increase in supply current from 4 A to 5 A reduces the temperature to 233 K.

7. At fixed temperature T_l maximum reduction of operating tip temperature is restricted to the value of thermopile optimal current. A deeper cooling at this supply current value can be obtained by reduction of T_l value.

8. A test bench and measurement procedure for full-scale test of the prototype has been developed. The results of experimental investigations of the prototype have demonstrated a satisfactory repeatability of calculated and experimental data. Maximum discrepancy between the calculated and experimental data did not exceed 11% over the entire measurement range.

9. The results of theoretical and experimental investigations of the thermoelectric system fort freezing of larynx tissues have shown its definite advantages for practical application.

References

1. A.Yu. Baranov, Cryogenic Physiotherapy, *Physiotherapy, Balneology and Rehabilitation* **3**, (2005).
2. A.Yu. Baranov, Artificial Cold at the Service of Health, *Herald of the International Academy of Refrigeration* **1**, (2006).
3. V.V. Portnov, Local Air Cryotherapy: Mechanism and Practical Application, *Resort Sheets* **2**, (2009).
4. *Patent RF № 2483691*, Cryosurgical Apparatus, V.N.Pavlov, S.V.Kungurtsev, D.V.Kulakov, 2013.
5. *Patent RF № 2520253*, Method for Treatment of Nanopharynx Tumors, P.V. Svetitsky, 2014.
6. *Patent RF № 2018273*, Method for Deep Local Cooling of Tissue, V.I. Kochenov, 1994.
7. *Patent RF № 2496442*, Cryotip with a Sapphire Cold Conductor-Irradiator, L.P. Mezhov-Deglin, V.N. Kurlov, I.A. Shikunova, M.K. Makova, A.V. Lokhov, 2013.
8. *Patent RF № 2372044*, Cryosurgical Instrument, Kh.Kh. Erganokov, 2009.
9. *Patent RF № 2293538*, Cryosurgical Apparatus, Yu.V. Korolev, S.M. Iushin, 2007.
10. *Medical Encyclopedia*, Ed. By V.I. Pokrovsky (Moscow: Medicine, 2003).

Submitted 14.04.2015.

NEWS
OF INTERNATIONAL THERMOELECTRIC ACADEMY

IVAN VASYLIOVYCH HUTSUL

On July 8, 2015, in his 69th year, Ivan Vasyliovych Hutsul, professor of Theoretical Physics Department, dean of Physics Faculty for many years, passed away.

Ivan Vasyliovych Hutsul is a graduate of Physics and Mathematics Faculty of 1971, Doctor of Science in Physics and Mathematics, professor of Theoretical Physics Department, corresponding member of the International Thermoelectric Academy.

Ivan Vasyliovych was born on June 24, 1947 in the village of Hlushkiv, Ivano-Frankivsk region. He graduated from Horodenka secondary school. He went into higher education at Physics and Mathematics Faculty of Chernivtsi University, on graduating from which he entered the post-graduate course of at Theoretical Physics Department of this higher educational institution. On graduating from the post-graduate course, training in which had to be interrupted for service in the army, he decided to cast his lot with Chernivtsi University where he first worked as a junior research fellow of scientific and research sector. On maintaining his PhD thesis in 1978, Ivan Vasyliovych became a senior research fellow. In 1986 he started his teaching activity first as assistant, and since 1990 as an associate professor at Theoretical Physics Department.

Simultaneously with teaching activities, Ivan Vasylyovych was actively engaged in scientific research and in 2001 he successfully maintained doctoral thesis “Electrical and Thermal Transport Phenomena in Anisotropic Semiconductors”.

The main area of scientific research pursued by I.V. Hutsul was a detailed analysis of the capabilities of anisotropic opticothermoelements offered for use at detection and continuous control of various-power radiant fluxes.

From June 2003 till 2013 he was elected dean of Physics Faculty.

The scientific heritage of I.V. Hutsul covers over 120 research and methodological works, 6 patents for inventions, and one PhD thesis maintained under his supervision.

On these exceptionally hard days for the friends and family of the diseased the International Thermoelectric Academy and Journal of Thermoelectricity Publishers extend their condolences and share the feeling of deep sorrow and untold loss.

ARTICLE PREPARATION RULES

The article shall conform to the journal profile. The article content shall be legible, concise and have no repetitions.

The article shall be submitted to the editorial board in electronic version.

The text shall be typed in text editor not lower than MS Word 6.0/7.0.

Page setup: “mirror margins”- top margin – 2.5 cm, bottom margin – 2.0 cm, inside – 2.0 cm, outside– 3.0 cm, from the edge to page header – 1.27 cm, page footer – 1.27 cm.

Graphic materials, pictures shall be submitted in color or, as an exception, black and white, in .opj or .cdr formats, .jpg or .tif formats being also permissible. According to author’s choice, the tables and partially the text can be also in color.

The article shall be submitted in English on A4 paper sheets; the number of pages shall not exceed 12. By agreement with the editorial board, the number of pages can be increased.

To accelerate publication of the article, please adhere to the following rules:

- the authors’ initials and names are arranged in the centre of the first page at the distance of 1 cm from the page header, font Times New Roman, size 12 pt, line spacing 1.2;
- the name of organization, address (street, city, postal code, country) – indent 1 cm below the authors’ initials and names, font Times New Roman, size 11 pt, line spacing 1.2, center alignment;
- the title of the article is arranged 1 cm below the name of organization, in capital letters, semi-bold, font New Roman, size 12 pt, line spacing 1.2, center alignment. The title of the article shall be concrete and possibly concise;
- the abstract is arranged 1 cm below the title of the article, font Times New Roman, size 10 pt, in italics, line spacing 1.2 ,center alignment;
- key words are arranged below the abstract, font Times New Roman, size 10 pt, line spacing 1.2, justified alignment. The title “Key words” – font Times New Roman, size 10 pt, semi-bold;
- the main text of the article is arranged 1 cm below the abstract, indent 1 cm, font Times New Roman. size 11 pt, line spacing 1.2, justified alignment;
- formulae are typed in formula editor, fonts Symbol, Times New Roman. Font size is “normal” – 12 pt, “large index” – 7 pt, “small index” – 5 pt, “large symbol” – 18 pt, “small symbol” – 12 pt). The formula is arranged in the text, centre aligned and shall not occupy more than 5/6 of the line width, formulae are numbered in round brackets right;
- dimensions of all quantities used in the article are represented in the International System of Units (SI) with the explication of the symbols employed;
- figures are arranged in the text. The figures and pictures shall be clear and contrast; the plot axes – parallel to sheet edges, thus eliminating possible displacement of angles in scaling;
- tables are arranged in the text. The width of the table shall be 1 cm less than the line width. Above the table its ordinary number is indicated, right alignment. Continuous table numbering throughout the text. The title of the table is arranged below its number, center alignment;
- references should appear at the end of the manuscript. References within the text should be enclosed in square brackets. References should be numbered in order of first appearance in the text. Examples of various reference types are given below.

– L.I. Anatychuk, *Thermoelements and Thermoelectric Devices: Handbook* (Kyiv: Naukova Dumka, 1979), p.766. (Book)
– T.M. Tritt, Thermoelectric Phenomena, Materials, and Applications, *Annual Review of Materials Research* **41**, 433 (2011). (Journal paper)
– U. Ghoshal, *Proceedings of the XXI International Conference on Thermoelectrics* (N.Y., USA, 2002), p. 540. (Proceedings Conference)

The article should be supplemented by:

- letter from the organization where the work was performed or from the authors of the work applying for the publication of the article;

- information on the author (authors): last name and initials; full name and postal address of the institution where the author works; academic degree; position; telephone number; E-mail;

- author's (authors') photo in color or, as an exception, in black and white. With the number of authors more than two their photos are not given;

- author's application to the following effect:

> We, the undersigned authors, … transfer to the founders and editors of "Journal of Thermoelectricity" the right to publish the article…in Ukrainian, Russian and English. This is to confirm that the present publication does not violate the copyright of other persons or organizations.
>
> Date Signatures

Below is given an example of article preparation.

ISSN 1607 - 8829. Journal of Thermoelectricity. 2015. № 2. 1-90